SIZE-DEPENDENT SCATTERING PROPERTIES OF PLANETARY REGOLITH ANALOGS

by

Jennifer Lynn Piatek

B.S. Physics, Rensselaer Polytechnic Institute, 1992

M.S. Geology, Arizona State University, 1997

Submitted to the Graduate Faculty of

Geology and Planetary Sciences, School of Arts and Sciences in partial fulfillment

of the requirements for the degree of

Doctor of Philosophy

University of Pittsburgh

2003

UNIVERSITY OF PITTSBURGH

FACULTY OF ARTS AND SCIENCES

This dissertation was presented

by

Jennifer Lynn Piatek

It was defended on

April 18, 2003

and approved by

William Cassidy

William Harbert

Robert M. Nelson

Michael S. Ramsey

Bruce W. Hapke
Dissertation Director

SIZE-DEPENDENT SCATTERING PARAMETERS OF PLANETARY REGOLITH ANALOGS

Jennifer Lynn Piatek, PhD

University of Pittsburgh, 2003

The physics of the interaction of light with a particulate surface are important to understanding and analyzing remote sensing data from planetary surfaces. An examination of the angular scattering properties of powder samples with known compositions and particle sizes was undertaken to try and further understand the interaction of light with a closely packed particulate medium. The samples range in size from smaller than to larger than the wavelength (λ) of incident light (0.05 – 30.09 μm in diameter, λ=0.635 μm). Based on a rich history of both theoretical treatments and laboratory measurements, results would be expected to show any dependence of scattering parameters on composition and/or particle size. Scanning electron microscope analyses of the powders were done to characterize particle size, composition, and shape as the major contributors to observed trends in scattering parameters. Models currently in wide use to describe light scattering by planetary regoliths make two important assumptions: (1) the propagation of light through the medium can be described by the equation of radiative transfer, which treats the medium as if it were made up of a continuous distribution of independent scatterers and absorbers; and (2) these fundamental scatterers are the individual particles that make up the medium. Models based on the radiative transfer equation were found to provide good empirical descriptions of the light scattering properties of particulate media composed of complex particles, such as planetary regoliths. However, the results reported here show that changes in scattering parameters predicted by the assumption that the particles are the

scatterers are not observed in these samples, and that such models do not accurately predict the transport mean free path, scattering coefficient, or extinction coefficient of such media. In particular, the transport mean free path shows remarkably little dependence on particle size over the size ranges studied, whereas the particle scattering assumption predicts a large variation. Theoretical models based on the second assumption should only be used with great caution when analyzing data taken on particulate surfaces.

Acknowledgements

First and foremost, I must thank the personnel at the Goniometer Laboratory at JPL for use of their samples, equipment, and time. Bob Nelson provided a summer job, additional data, an intellectual sounding board, and a fascinating explanation of the probabilistic intricacies of throwing two dice down a felt table (and betting on the outcome). Bill Smythe, whom I must thank for acting as an impromptu unofficial committee member, was always there to throw a wrench in our monkey plans. Amy Snyder Hale provided much lab support, and was always there for those last minute email requests.

Thanks to everyone at R.J. Lee Group in Murraysville, PA, for their time, assistance, and patience while helping me do the automated particle sizing. Stephen Kennedy, Marsha Dreiblebis, John Johns, Barb Kutchko, and a number of other people (whose names I have sadly forgotten) gave me advice, lab space, and access to the equipment I needed. Even though we eventually rejected that data, this was an indispensable portion of this project.

My committee (Bill Cassidy, Bill Harbert, Bob Nelson, and Mike Ramsey) had to wade through all 150+ pages, 30+ equations, and 100+ plots of this document. Their advice was an important addition to the final product. Thanks also to Brian Stewart for sitting on my comps committee as a last minute substitution, so I didn't have to reschedule.

Another earlier committee member, David Crown, gave me not only good criticism at those exams, but also was responsible for my first experience with journal article writing, and gave me a good swift kick in the butt when my comps didn't come along as fast as they should have. I never really realized the value of working with a perfectionist until I sat up late at night

aligning images in figures to millimeter precision: the final results of any work I do will be that much better, and I am grateful for that learning experience.

I never got a chance to thank anyone at Arizona State for help during my M.S. degree: belated thanks to my advisor, Phil Christensen (for keeping me around long enough to finish!) and to everyone in the TES lab for putting up with me for so long.

Thanks again to Amy Snyder Hale for letting me stay with her at Mount Wilson, and also to Dave Hale (and Shelly, Daisy, and Stanley) for letting me invade their space and take up all of Amy's spare time.

My fellow grad students at Pitt actually kept me sane, whether they wanted to or not. Candace "Hash Brown" Kairies is not only a good friend, but also a great roommate who always understood why I had to shout "shoot the #?$%@ puck!" at the T.V. now and again. Sarah Bee Z. McElfresh probably listened to more of my griping than was anyone's due, and always had something helpful and encouraging to say. Jeff Byrnes always had something interesting to discuss, and a never-ending supply of great music. Scott Mest, Sherry "G.G." Stafford, and Lee Beatty (who always found the right time for a Dio song) kinda round out the "insanity crew": I don't know what I would have done without these folks. A round for the gang at happy hour, wherever we happened to end up. Thanks also to the U of R crew at Nags Head for much fun and relaxation (fire the laser!).

The Planetary Volcanology Field Workshop (August, 2001) gave me a chance to see the island of Hawai'i in all its volcanic splendor – every geologist should do this at least once. Thanks to Scott Rowland and NASA for the workshop, and "Mahalo, Pele" for sharing the gifts of your wonderful island: I thought often of those places while slaving away at the computer.

For those that will never actually see this document: thanks to the programmers of gnuplot (without which the dissertation would never have been finished), and also to those who worked on RedHat Linux and Mac OS X. S. Boid, Drazowl, Manny, and Cap'n Hector kept everything amusing. Thanks, but no thanks, to N.J.C. and P.K.: I hope you someday regret those choices you made. (Still blue and green, after all these years!) Much gratitude to the Jameson and Jack Daniels distilleries, also without whom this dissertation would never have been finished. No work was ever completed without a soundtrack, thanks to those artists who managed to write the perfect song for each moment in the process (Disturbed, Godsmack, Megadeth, Ozzy, Queensryche, and many others).

For those who really could never begin to understand: I must thank Nott (who taught me to believe), P.A. (who taught me how to fly), Homer, 'D', and Knick for their unconditional friendship when I really needed it. Marvin, I wish for you an unobstructed view of Venus.

Lastly, but certainly not leastly, I have to thank my advisor, Bruce Hapke. I really did come to Pitt because I wanted to work with him, and while I may have had second thoughts now and again, I can truly say I would not be where I am today without his help and advice (and his book, which I never did actually finish reading).

May 15, 2003
Arkham, MA
(Go Pods!)

Dedication

To my parents, who always taught me I could do anything I put my mind to.
And to James, for being there to remind me they were right.

And lastly to those who inspire through their courage, dedication, and sacrifice.
We believe, and we remember.
Apollo 1 Challenger Columbia

TABLE OF CONTENTS

LIST OF TABLES

LIST OF FIGURES

Introduction

The light scattered by a planetary object has been used to make inferences about the nature of the object's surface since the telescope was first pointed at heavenly bodies. Galileo noted that the dark areas of the Moon he called “seas” were probably not water, as they did not exhibit the strong specular reflection associated with the relatively smooth surfaces of a lake or ocean. More recently, the light coming from a distant object (whether it be emitted, reflected or transmitted) has been used to study the composition of that object using the principle of spectroscopy; atoms, molecules, and minerals absorb specific frequencies of light that are characteristic of their composition. Considering the difficulty and expense of making *in situ* measurements of planetary surfaces (even some on our own planet), the ability to study a surface remotely is key to understanding the processes that shape the solar system. The principle of spectroscopy operates simply when the object being studied is homogeneous in composition and the geometry is well known. Complications arise, however, when the composition is heterogeneous, or if the geometry is not simple.

The physics of the interaction of light with flat surfaces are well known; the earliest studies of light have quantified where the light will be reflected or refracted, depending on composition (specifically the index of refraction, through Snell’s Law), and what percentage of that light will be reflected or transmitted (Fresnel’s Law). In these interactions the light can often be treated as if it consists of rays and its wave nature ignored (geometric optics). Recently, light scattering models have been extended to include particulate surfaces, which are better representatives of actual planetary surfaces. It has been noted that scattering from the surfaces of media composed of particles that are large with respect to the wavelength is similar in certain

aspects to that for the flat surfaces noted above; when a particle is large (compared with the wavelength), its interaction with light can be adequately described by geometric optics. When the particle size approaches the wavelength, however, the interactions are no longer simple, because waves scattered from one part of the particle to another, or between particles, will interfere coherently with each other. It is the purpose of this thesis to examine the changes that occur in the light scattering properties of particulate media as the particle size changes from larger than to smaller than the wavelength.

This complication is apparent in reflectance and emission spectroscopy of samples with varying particle sizes. Often, strong IR absorption bands decrease in depth with increasing particle size, while weaker bands often increase in depth and shift position as well (Conel, 1969; Salisbury *et al.*, 1987; Moersch and Christensen, 1995; Mustard and Hays, 1997; Cooper and Mustard, 1999). Numerical models that attempt to explain these changes as combinations of current models have not been successful, although one of the causes may be incorrect values of the complex refractive indices used in modeling, particularly those of quartz published by Spitzer and Kleinman (1961) (Moersch and Christensen, 1995; Mustard and Hays, 1997). The inferred cause of spectral band depth reduction in thermal emission spectroscopy is that the observed light represents both the light directly emitted by a particle, and light that has been multiply scattered by nearby particles (i.e. reflected). A result of Kirchoff's Law is that the reflectance and emissivity of an optically thick substance at the same temperature sum to 1; in a spectrum, the combination of emitted light and multiply-scattered light tends to approach unit emissivity as the contribution of multiple scattering increases. Because of coherent effects, the nature of the multiple scattering can change as particles approach the size of the wavelength.

The effect of changing particle sizes has also been noted in studies of the opposition effect, which is an observed increase in the reflectance of a surface when the angle between the light source and the observer is very small. While the relationships between the porosity of a surface and the angular width of the opposition surge are thought to be well understood for media consisting of colloidal suspensions of perfect spheres (i.e. Kuga and Ishimaru, 1984; Wolf *et al.*, 1988), this is not the case for media of irregular particles in contact with each other. The latter is a more realistic analog of planetary regoliths. Predicted relationships between the width of the opposition peak, the wavelength, and the sizes of the particles have not been observed in previous laboratory studies (i.e. Nelson *et al.,* 2000; Hale *et al.*, 2002; Nelson *et al.*, 2002a). A better understanding of the correlation between particle size and the parameters of the opposition surge is key to understanding how planetary regoliths scatter light, and how physical parameters of those surfaces can be determined from that scattered light. The determination of these physical parameters is the goal of remote sensing observations of planetary surfaces. What follows is an experimental study examining the changes in reflectances of particulate samples as the viewing angles are changed. The intent was to determine the relationship between particle size and scattering parameters such as the magnitude and width of the opposition surge, the effective single scattering albedo, and the effective single scattering function.

Background

Scattering Models

There are two commonly used starting points for models of the interaction of light and matter; the equations of radiative transfer (Chandrasekhar, 1960), and the Mie solution to Maxwell's equations (Mie, 1908 - as presented in van de Hulst, 1957; Hansen and Travis, 1974; and Bohren and Huffman, 1983, among many others). The radiative transfer equation assumes that the medium is made up of units that scatter independently; that is, that the waves scattered by each unit do not interfere coherently with each other. A scattering unit might be a facet on a particle surface, an inhomogeneity within a particle, the particle itself, or an agglomerate of particles. If this condition is met, it provides exact, but not analytic, solutions for the transmission, reflection and emission by the medium. The solution requires either significant computing time, or approximations that allow the equations of the model to be analytically solved. Approximate models have been proposed by Lumme and Bowell (1981) and Hapke (1981, 1993). A useful method is the two-stream approximation, which averages the radiance over the upwelling and downwelling directions and allows for an analytical solution. The two-stream approximation has been widely applied to radiative transfer problems in the planetary sciences (i.e. Conel, 1969 and those summarized by Hapke, 1993). One of the more commonly used models has been referred to as the "isotropic multiple scattering approximation" (IMSA), and has gone through several incarnations (Hapke, 1981; Hapke and Wells, 1981; Hapke, 1986). A modification of this particular model (Hapke, 2002), which more accurately describes multiple scattering, will be used for further analysis of laboratory phase curves.

Using the radiative transfer equation for a particulate medium requires the specification of the scattering properties of a typical scattering unit. It is almost universally assumed that

these independently scattering units are the particles that make up the medium. The Mie solution to Maxwell's equations provides a description of the interaction of light with an isolated, spherical particle of any size. Recently, the T-matrix formulation, which can exactly calculate scattering by a particle of a somewhat more complicated shape than a sphere, has been published by Mishchenko (1991, 1993b) and Mishchenko and Travis (1998). An alternative approach is the equivalent slab model of Hapke (1993) in which a particle is approximated by a one-dimensional slab. This model has the advantage that it is analytic and that internal scatterers within the particle can easily be included. These solutions have also been widely used in planetary science, but often the limitations of the solutions are ignored. In particular, Mie theory does not consider particles that are closely spaced or non-spherical. However, this theory has been used with some success in conjunction with other models that do consider the more complicated factors (i.e. Moersch and Christensen, 1995; Mustard and Hays, 1997).

Remote sensing instruments gather information about the light that is scattered off of or emitted by a planetary surface. The intent of collecting these data is to learn about the physical properties of the surface: properties such as composition, particle size, and porosity. The data, however, is not simply analysed. These physical properties can have a variety of effects on the results, and complex scattering models such as the ones discussed above are often used in analyses of these data to try and determine physical properties. Better understanding of how the light interacts with the surface is key to improving these models, and thus improving the interpretations of remotely sensed data. Laboratory studies are useful for improving this understanding, because the physical properties of the target surface can be determined through other methods and correlated with light scattering or emission results.

Geometries

In order for the text that follows to be understandable, the geometries and variables that will be used are described here. The viewing geometry referred to through this study is pictured in Figure 1. Three angles are defined in this figure; the angle of incidence (i), the angle of viewing or emission (e), and the phase angle (g). The angle of incidence is defined here as the angle between the direction from the surface to the light source and a line perpendicular to the surface. The angle of emission is the angle a line from the surface to the observer (usually a light detector of some kind) makes with that same perpendicular line. In the experiments reported here, these two angles lie in the same plane, called the "principal plane". The phase angle is defined as the angle between the directions from the surface to the light source and the observer. A plot of intensity (or reflectance) versus phase angle is referred to as a "phase curve". The scattering angle (Θ), defined as the angle between the direction of propagation of the incident ray and the scattered light, is the complement of the phase angle ($\Theta = \pi - g$).

The Fundamental Particle Scattering Assumption

The radiative transfer equation describes the radiation field inside a medium as a gas of photons diffusing through the material; the theory of radiative transfer is also used to describe energy transfer within gases such as those in a planetary atmosphere or the interior of a star. An auxiliary assumption that is not part of the radiative transfer equation, but that is commonly used with it, is that the scattering units are the particles, which scatter independently; there are assumed to be no coherent interactions between light scattered from two different particles, and the phase of that scattered light is assumed to be random. This assumption is probably valid for a medium of isolated particles, such as clouds or atmospheric aerosols, but is suspect for media

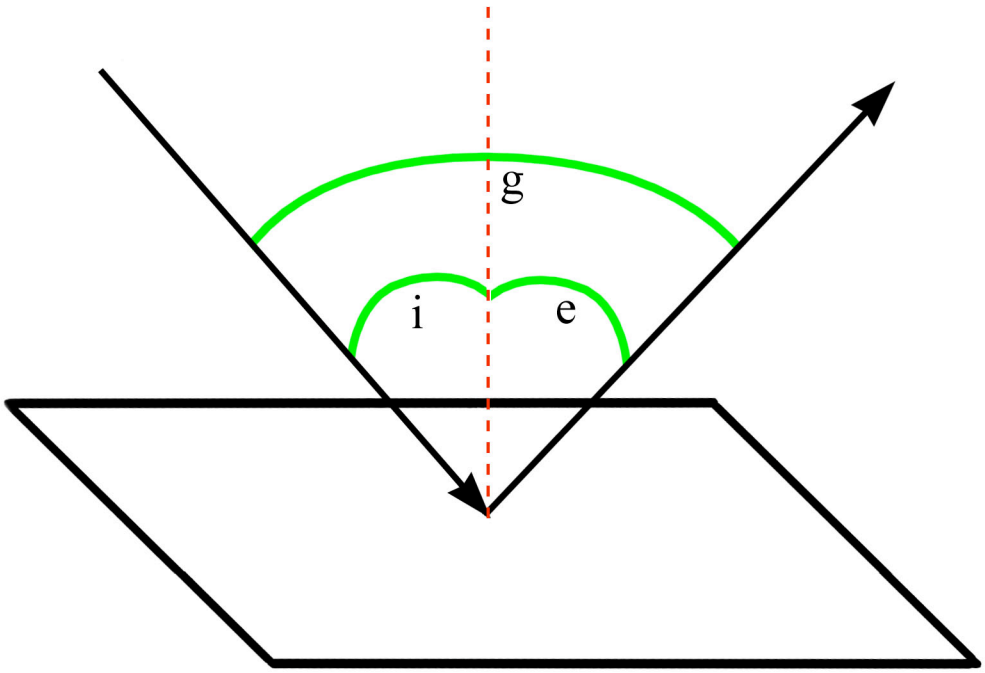

Figure 1: Diagram of viewing geometry.

where particles are closely packed. The canonical definition of "isolated" is that the nearest neighboring particle is at least 3 particle radii away; this definition, however, is based on a comment in the introduction of van de Hulst (1957), which has never been theoretically or experimentally justified. This criterion is certainly not true for powders or media such as planetary regoliths, which are often the target surfaces for spectroscopic investigations whose aim is to determine the physical parameters of the target surface remotely.

The radiative transfer equation (RTE) is concerned with two physical properties of the scattering units of the medium; the single scattering albedo (w), and the single scattering function (p(g)), which describes the relative amount of light scattered into a direction given by the phase angle g. The average cosine of the scattering angle (<cos□>), also called the cosine asymmetry factor, is derived from p(g) and characterizes that function. The value of <cos□> is determined by the integral (Hapke, 1993, p. 68):

$$\langle \cos\theta \rangle = \frac{1}{2} \int_0^{\pi} \cos g\, p(g) \sin g\, dg. \qquad (1)$$

[*Note: a list of all variables used in this study and their symbols appears in Table 1*]. If this parameter is negative, then the unit is backscattering, meaning it scatters a majority of the incoming light back to the hemisphere containing the incident beam. If the result is positive, the material is forward scattering; the majority of scattered light is in the hemisphere opposite the incoming beam). A value of zero indicates a unit that scatters symmetrically (equal amounts into each hemisphere): an isotropic substance is a special case of a symmetrical scatterer. These two independent parameters are related to five other non-independent parameters — the scattering coefficient (S), the absorption coefficient (K), the extinction coefficient (E), the volume angular scattering coefficient (G(g)), and the transport mean free path (L). The extinction coefficient represents the fractional intensity of light that is "removed" per unit path length from a beam as it

Table 1: Variables used in the text, listed alphabetically.

$\langle\cos\theta\rangle$	average cosine of the scattering angle
A	area
A_B	beam area
B_{C0}	amplitude of CBOE
B_{S0}	amplitude of SHOE
C_{ext}	average exinction cross section per particle
C_{sca}	average scattering cross section per particle
e	angle of emission
E	extinction coefficient
g	phase angle
h_c	CBOE width parameter
h_s	SHOE width parameter
HWHM	half width at half max
i	angle of incidence
I	radiance
J	irradiance
L	transport mean free path
$m(\lambda)$	complex refractive index
N	number per unit volume
p(g)	single scattering function
Q_E	extinction efficiency
Q_S	scattering efficiency
r	reflectance
R	relative reflectance
S	scattering coefficient
v	volume
w	single scattering albedo
x	radius
α	filling factor
λ	wavelength
μ	cos(e)
μ_o	cos(i)
θ	scattering angle
ρ_B	bulk density
ρ_S	solid density
σ	geometric cross section

propagates through the material, and therefore is not measured by a detector. This can be accomplished through scattering out of the beam path, absorption of the light by the material, or bending of the light path out of the field of view of the detector (diffraction). Because the material considered here consists of many small particles in contact with each other, the amount of light that is initially diffracted (via separations between the particles) is quite small, and it almost immediately encounters yet another particle. This light is essentially indistinguishable from the incident beam (Hapke, 1999). For this reason, diffraction is ignored for the model fits. Thus, in the case of a particulate sample like a planetary regolith, the extinction coefficient is the result of scattering and absorption. The fraction of light scattered per unit length is represented by the scattering coefficient, and the fraction absorbed per unit lengthby the absorption coefficient (K), so that the relationship is E = S + K. The fraction of light scattered per unit volume, G(g), is simply defined as G(g) = Sp(g).

The relationship between S and the transport mean free path is given by (Hapke, 2002, eq. 35):

$$L = \frac{1}{S\left(1 - \langle \cos \theta \rangle\right)}. \tag{2}$$

The transport mean free path may be thought of as the mean distance a photon travels though a medium before its direction of travel is changed through a large angle (about a radian) (Hapke, 2002). The ratio of the scattering coefficient to the extinction coefficient is equal to the single scattering albedo (Hapke, 1993, p. 66):

$$w = \frac{S}{E}. \tag{3}$$

These two formulas are easy to calculate, and provide the remaining scattering parameters necessary for comparison with fundamental particle scattering theory. If it is assumed that the

particles are the fundamental scattering units, then the extinction and scattering coefficients can be related to the particle extinction and scattering efficiencies (Q_E and Q_S) through the relationship (Hapke, 1993, p. 158):

$$E = \sum_i n_i \sigma_i Q_{Ei}$$
$$S = \sum_i n_i \sigma_i Q_{Si} \quad (4)$$

where n represents the number of particles per unit volume, and σ is the geometric cross section of a particle. Each term denoted by subscript i represents a different type of particle present in the medium (such as different in size, shape, or composition). If the fundamental particle scattering assumption is valid, then L becomes (Hapke, 2002, eq. 35):

$$L = \left[\sum_i n_i \sigma_i Q_{Si} \left(1 - \langle \cos \theta \rangle\right) \right]^{-1}. \quad (5)$$

Isolated-particle scattering models — such as Mie, T-matrix, or equivalent slab — can be used to calculate the values of both Q_E and Q_S for different particle types, after suitable corrections for the removal of diffraction.

This study had several objectives related to the assumption of fundamental particle scattering and the models based on this assumption. (1) Radiative transfer based models can empirically describe scattering by media of particles whose sizes are greater than the wavelength; how well do such models describe the scattering of media with particle sizes equal to or smaller than the wavelength? (2) To what extent is the fundamental scattering assumption valid; can models and relationships based on the assumption of isolated particles be reliably applied to data from planetary regoliths and regolith analogs? (3) If the fundamental scattering assumption is not valid, then what is the physical meaning of the radiative transfer parameters

given above. (4) Can particle properties be derived from photometric laboratory measurements or remote sensing data?

Previous work examining the effect of particle size, packing density, and wavelength on light interaction has shown that there is indeed a relationship between these factors. Ishimaru and Kuga (1982) performed a series of transmission experiments with different sizes and packing densities of latex spheres in suspension. The light source was a red laser beam, which passed through the sample, then through a polarizer, and then was focused on a detector. The path length of the laser through the sample could be controlled by varying the cell holding the sample. The resulting intensity was then used to calculate the attenuation constant for the material (essentially the same as the extinction coefficient defined above). Their results show that the attenuation constant increases with increasing density for particle sizes larger than the wavelength; however, their attenuation constant results show a decrease with increasing density for particle sizes smaller than the wavelength, probably due to coherent interactions between the particles. Their results do suggest that there is some relationship between the wavelength of scattered light and the properties of the scattering units of the medium.

The existence of a relationship between the scattering properties and the ratio of particle size and wavelength in the scattering of light has been well documented in spectroscopic studies in the infrared region of the spectrum. At these wavelengths, natural surfaces and samples often have particle sizes that are similar to the wavelength. Studies of the reflectance and emission spectra of well sorted samples of quartz and olivine showed a dependence not only on size relative to wavelength, but with the imaginary part (k) of the refractive index as well (Mustard and Hays, 1997). The wavelength-dependent complex index of refraction of a material consistents of two parts. The real portion (n), or the index of refraction, defines the angular

change in the path of a light wave when it is refracted. The imaginary portion (k), or the absorptivity, describes how likely the light at that particular wavelength is to be absorbed by the material. Mustard and Hays (1997) suggested that when $k << 1$, the reflectance drops sharply when the particle size is similar to the wavelength. When k is larger (> 0.1), there is a decrease in reflectance in observed restrahlen bands with decreasing particle size, although there is no observable change in this decrease near the size of the wavelength. The shape of these bands changes as well. They also noticed that the Christiansen feature broadens and saturates with changing particle size if k is non-negligible; very small values of k showed no real variation in this feature. A similar study examining the changes in the spectra of smectite clay and palagonitic soil produced similar results (Cooper and Mustard, 1999).

An attempt to model the changes in quartz emission spectra with existing scattering models was made by Moersch and Christensen (1995). Thermal emission data for a series of sorted quartz samples were compared with theoretical results from a series of models; those of Mie (1908); Conel (1969); and Hapke (1981, 1984, and 1986). The models were also used in combination to see if this produced a better fit to the results. The models of Hapke and Conel are radiative transfer based, and Mie scattering theory has been discussed in a prior section. The conclusion of this particular study was that while none of the models could independently fit the data, a best fit was produced by using a combination that used Mie theory to determine single scattering albedo, which was then used in Hapke theory to determine emissivity. This hybrid model fit well with small and moderate values of k, but failed to predict behavior where k was large. A possible source of error in the model was incorrect values of the complex refractive index in the published literature (those of Spitzer and Kleinman, 1961). In addition, it was noted

that the regions where k was small (where emissivity bands were not present) were extremely sensitive to particle size.

The Opposition Effect

The opposition effect is an observed increase in the reflectance of particulate surfaces as the phase angle approaches 0°. Other terms used to refer to this effect include the opposition surge, retroreflectance, the hot spot (when seen in vegetation), and heileigenschein (lit. "holy shine"), but the term "opposition effect", coined by Gehrels (1956), is the currently preferred phrase in planetary remote sensing. This phenomenon was first noted in observations of the rings of Saturn made by Seeliger (1887,1893). who suggested that the mechanism responsible for this increase was "mutual shadowing effect". In this scenario (see Figure 2), the particles nearest the source cast shadows on particles that are further away, thus reducing the reflected light seen by the observer. When the phase angle is small, however, these shadows are not visible because they are blocked by the particles casting them. The result is an apparent increase in the reflectance of the object. An opposition surge produced by this mechanism is referred to as a "shadow-hiding opposition effect" (or SHOE), as discussed by Hapke (1963), Irvine (1966), and Hapke (1986). A multitude of later observations confirmed the existence of an opposition effect for Saturn's rings (including Bobrov, 1970; Irvine and Lane, 1972; Lumme and Irvine, 1976), as well as investigating an

additional possible cause of the effect – extremely backscattering ring particles (i.e. Franklin and Cook, 1965; Cook *et al.*, 1973; Kawata and Irvine, 1974; Price, 1974).

Saturn's rings are not the only Solar System object to exhibit an opposition surge, however. Gehrels (1956), as part of a survey of asteroid light-curves, noted that 20 Massalia also exhibits an opposition surge. Continued observations showed that the opposition effect is

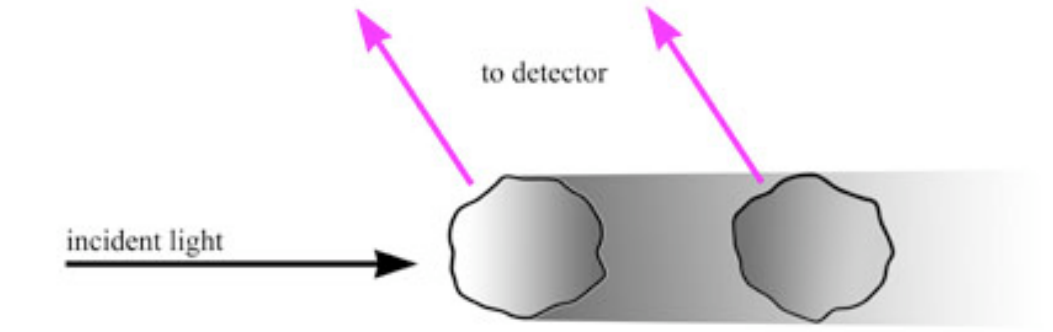

a) Large phase angle case: detector observes both the illuminated particle and shadowed particle behind.

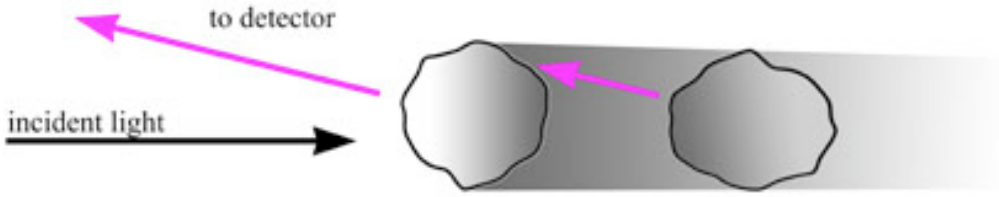

b) Small phase angle case: detector observes only the illuminated particle.

Figure 2: Diagram of shadow-hiding mechanism.

commonly observed on these objects (Taylor *et al.*, 1971; Shevchenko *et al.*, 2002, among many others). Phobos and Deimos (the moons of Mars) are thought to be captured asteroids, and also exhibit opposition surges (Klaasen *et al.*, 1979).

Observations of larger objects have also displayed opposition surges, which have been used to make inferences about the object's surface. These include Mercury (Mallama *et al.*, 2002), Io (Simonelli and Veverka, 1986), Europa (Helfenstein *et al.*, 1998), Iapetus (Franklin and Cook, 1974), Titania (Lane *et al,*, 1986; Nelson *et al.*, 1987; Thomas *et al.*, 1987; and Helfenstein *et al.*, 1988), and Triton (Lane *et al.*, 1989; Buratti *et al.*, 1991). This, however, is far from an exhaustive list of the studies of the phase curves of planetary objects!

Additionally, the phase curves of the Moon and Mars have warranted close attention, particularly the lunar surface. The lunar opposition surge was first noted by Gehrels *et al.* (1964). Early explanations for this effect included shadowing by fine-scale surface structures such as vesicles (Minnaert, 1961) or highly porous, lacy "fairy-castle" structures in the lunar regolith (Hapke and van Horn, 1963). Numerical models suggested that the surface dust layer needed to be extremely porous to explain the observed opposition effect (Hapke, 1963), causing some to suggest that electrostatic levitation caused a fine layer of particles to be suspended above the surface of planetary objects (Gehrels *et al.*, 1964). Mars also exhibits an opposition surge (O'Leary, 1967, Thorpe, 1979). From the surface color, it appeared that the planet was covered by a layer of oxidized iron, prompting comparison between lab samples and the Martian phase curve (O'Leary and Rea, 1968; Egan, 1969).

Initial laboratory studies, however, were unable to duplicate the opposition effect, until Oetking (1966) showed that a variety of natural samples did in fact have narrow opposition surges. A number of laboratory studies confirmed the existence of an opposition surge in a

variety of manmade and natural particulate samples (Egan and Hilgeman 1976; Egan and Hilgeman 1977; Gradie *et al.*, 1980; Buratti *et al.*, 1988), as well as vegetation (Hapke *et al.*, 1996), and both lunar and meteoritic samples (O'Leary and Briggs, 1970; O'Leary and Briggs, 1973; Egan *et al.*, 1973).

The observation of this effect was often used to identify the presence of a regolith at the surface of an object and to try to quantitatively determine the porosity of the surface. Because of the diffraction of light around small particles, shadow-hiding becomes less efficient as the particle size approaches the wavelength. In addition, samples with high albedos would be expected to have smaller shadow-hiding opposition surges because multiply-scattered light illuminates the shadows. However, bright particulate surfaces often exhibit a strong opposition surge. An additional mechanism was needed to explain opposition surges from high albedo surfaces and from media with very small particles. This additional mechanism turned out to be coherent backscatter.

First identified by Kuga and Ishimaru (1984) and Tsang and Ishimaru (1984), and first described in the literature as weak localization (Wolf and Maret, 1985; van Albada and Lagendijk, 1985), coherent backscatter refers to the coherent addition of two multiply scattered light waves that travel the same path through the material, but in opposite directions, as shown in Figure 3. Each part of the incident wave front enters the sample at a different point, and exits where the other ray entered. At zero phase angle, or if the separation of these two entrance/exit points is small, the waves are in phase with each other. Coherent addition occurs when the waves are in phase (otherwise they interfere randomly), and this coherent addition is responsible for increasing the reflectance near opposition. This mechanism is referred to as the "coherent backscatter opposition effect" (or CBOE), and has been suggested as one of causes of the strong

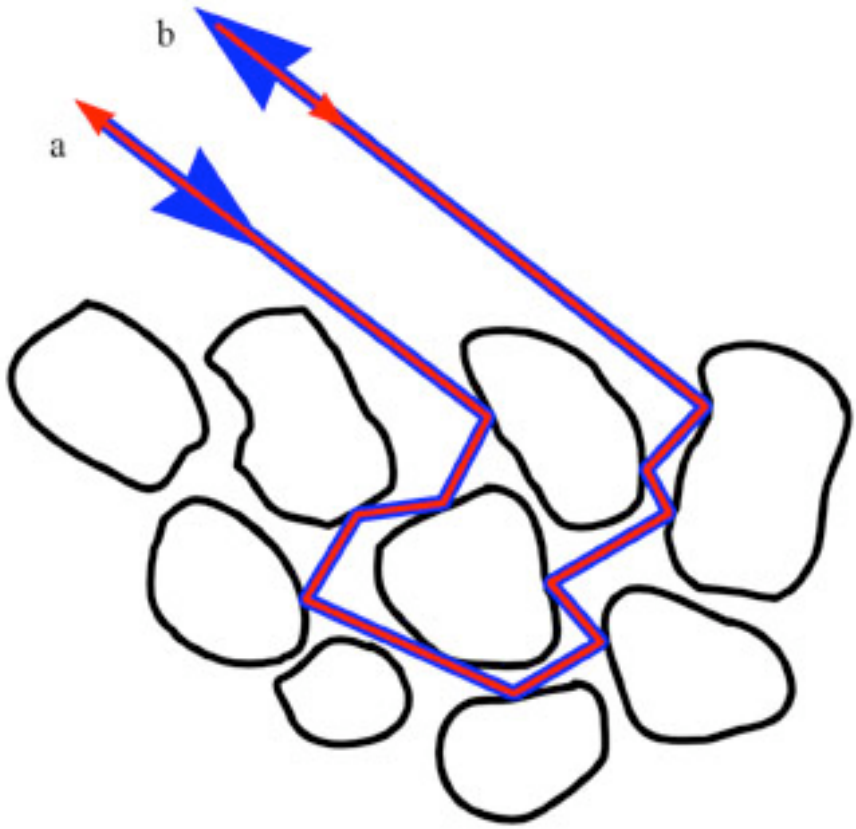

Wave front 1 (outer blue ray) enters from direction a., is scattered
multiple times within the media, and exits in direction b..
Wavefront 2 (inner red ray) follows the exact same path,
only in the opposite direction (enter from b., exit towards a.).
If the two fronts are in phase, they will interfere constructively.

Figure 3: Diagram of coherent backscatter mechanism.

opposition surges of icy satellites (Shkuratov, 1988; Muinonen, 1990; Hapke, 1990; Hapke and Blewett, 1991, Mishchenko, 1992a).

Theoretical studies of coherent backscatter suggested that there should be different effects with different polarizations, particularly when the light is circularly polarized (Stephen and Cwilich, 1986; Etemad *et al*., 1987; Peters, 1992); changes in observed reflectances in linearly polarized light have been observed as well (Kuga *et al*., 1985). As noted in the explanation of Hapke *et al*. (1993), during a specular reflection or Rayleigh scattering, the helicity (or direction – clockwise or counter-clockwise, or handedness (left or right, depending on direction of rotation)) of a circularly polarized wave changes to the opposite sense. So if light is singly scattered or reflected, the observed light will have the opposite helicity. Multiple scattering or reflecting events, however, will continue to reverse the direction of polarization. These events will also tend to scatter light out of the view of the detector, and to reduce the intensity of the continuing wave (since no natural surface reflects 100% of the light incident upon it). The result is that the polarization of multiply scattered coherent light will become more random as the number of scatterings increases, meaning that the most strongly circularly polarized portion of multiply scattered light will have undergone two scattering events (Hapke *et al*., 1993). Since the helicity is reversed at each event, this light will have the same helicity as the incident light. Since the CBOE requires multiply scattered light, the major contribution to the opposition increase will be due to light that has been scattered twice, and hence has the same direction of circular polarization as the light incident on the sample. The circular polarization ratio is defined as the ratio of light scattered with the same helicity as the incident light to that with the opposite helicity. The preceeding discussion implies that the circular polarization ratio will increase with decreasing phase angle if the CBOE is present. This increase in the circular

polarization ratio is widely regarded as the characteristic signature of the CBOE (Hapke *et al.* 1993).

Since both mechanisms are believed to operate in particulate samples (and planetary regoliths), this circular polarization effect is thought to be capable of separating the two opposition effect mechanisms. This is necessary for quantitative analysis of observations. Such analyses, however, have not yet conclusively separated the effects of the SHOE and CBOE for the much-studied lunar surface (Hapke *et al.*, 1993; Hapke *et al.*, 1998). Quantitative theoretical analyses of the CBOE based on the fundamental particle scattering assumption predict a relationship between the particle size and the width of the opposition surge (Hapke, 1993; Mishchenko and Dlugach, 1993; Mishchenko, 1992b). Such a relationship has been observed for media of well-separated particles (Kuga and Ishimaru, 1984; van Albada and Lagendijk, 1985 and 1987; Wolf *et al.,* 1988), but has not been observed for media of complex particles in contact (Nelson *et al.* 2000). The validity of such models is further examined as part of this study. A strong dependence of the width of the CBOE on the wavelength of scattered light has also been predicted (Kuga and Ishimaru, 1984; van Albada *et al.*, 1987; Ishimaru and Tsang, 1988), but has not been observed in practice for closely packed media (Nelson *et al.*, 2002b).

Sample Characterization

Technique

The intent of this study is to examine how the bidirectional reflectances of particulate samples of the same composition vary with changing particle size for sizes both larger and smaller than the wavelength. Samples were chosen based on particle size availability, a well-characterized composition, and as narrow particle size distribution as possible. These samples were then analyzed using instruments capable of measuring reflected light in both linearly and circularly polarized light at a variety of phase angles.

The wavelength of light used in this study was a major constraint to particle size due to instrument availability. The availability of instruments that could measure scattered intensity and polarizations at both very small and large phase angles determined the wavelength. In this case, the instruments used had a 0.635 μm wavelength laser source. It is possible to change lasers to obtain measurements at different wavelengths, and the theory does not constrain the wavelength; however, it was impractical to switch lasers at the time of data collection, so the wavelength of 0.635 μm became a fixed constrant on particle size. This meant that the particle sizes used would have to bracket this wavelength. Materials that are readily available in this size range are normally manufactured for use as pigments, food additives, or abrasives. Since these materials are manmade, the particle size, shape, and composition are often well known. Even so, additional analysis was undertaken to ensure that these parameters were well understood.

Three different powders were used for this study: aluminum oxide, iron oxide, and precipitated calcium carbonate. The aluminum oxide abrasive powder was obtained in thirteen different particle sizes. The iron oxide was manufactured as a pigment, and was described as

□-hematite (Fe_2O_3) by the manufacturer. Six different sized samples were analyzed. The precipitated calcium carbonates are intended as food additives, and four different sizes were obtained. A table of manufacturer, composition, and particle size for all three compositions appears in Table 2.

In addition to these parameters, the particle shape is also important for understanding the reflectance of the powdered samples. The particle shape of the precipitated calcium carbonate was identified using the manufacturer's specifications. Particle shapes of the aluminum and iron oxides were identified using scanning electron microscopy (SEM); in particular, the Phillips SEM located in the Materials Science department at the University of Pittsburgh. Samples were prepared using a relatively simple method. First, double-sided carbon tape was applied to the surface of an appropriate SEM stub. The upper surface of the tape was exposed, and a small amount of the powder placed on the adhesive surface. A Teflon spatula was used for this purpose, and also to press the powder onto the tape. Particles that did not stick were blown off using compressed air. The prepared stub was then coated with an approximately 8 nm-thick veneer of palladium, which provides a charging surface for the electron beam. Samples were analyzed in the SEM by picking random spots on the surface that were suitable for viewing (i.e. had a large population of particles that were arranged in a level manner). Large clumps of particles sticking above the mean surface of the sample tend to increase the charging and significantly affect the quality of the image. Areas that were picked were examined at a high enough magnification to identify the shapes of the particles in the image. Approximately 3 areas per sample were viewed in this manner, due to time constraints. Representative SEM images appear in Appendix 1.

Table 2: List of composition, supplier, supplier's product number, and given average/nominal particle diameter for each sample used in this study. Also included are the optical constants (n(□) and k(□)) used in theoretical calculations for each composition, as well as the diameters given for the aluminum oxide samples by Nelson *et al*. (2000), which vary from those used here.

			This study	Nelson *et al*. 2000
Aluminum Oxide	Microabrasives Corp.	Microgrit GB 3000	0.05 μm	0.1 μm
n(0.635 μm) = 1.766 k(0.635 μm) = 7.86 x 10^{-6}		Microgrit GB 2500	0.1 μm	0.5 μm
		Microgrit GB 2000	0.3 μm	1.0 μm
		Microgrit GB 1500	0.7 μm	1.2 μm
		Microgrit GB 1200	1.0 μm	1.5 μm
		Microgrit WCA 1	2.1 μm	2.1 μm
		Microgrit WCA 3	3.2 μm	3.2 μm
		Microgrit WCA 5	4.0 μm	4.0 μm
		Microgrit WCA 9	5.75 μm	5.75 μm
		Microgrit WCA 12	7.1 μm	7.1 μm
		Microgrit WCA 20	12.14 μm	12.14 μm
		Microgrit WCA 30	22.75 μm	22.75 μm
		Microgrit WCA 40	30.09 μm	30.09μm
Calcium Carbonate	Whittaker, Clark, & Daniels Inc.	5961 Calcium Carb Multifex Ultrafine	0.06 μm	
n(0.635 μm) = 1.658 k(0.635 μm) = 0.00026		5900 Calcium Carb Albaglos Tech Grade	0.8 μm	
		5970 Calcium Carb Albacar Tech Grade	1.1 μm	
		2923 Calcium Carb Heavy	3.0 μm	
Iron Oxide	Harcros Pigments (now Elementis Pigments, Inc.)	Copperas Red Iron Oxide R1299	0.15 μm	
n(0.635 μm) = 3.0374 k(0.635 μm) = 0.02455		Copperas Red Iron Oxide R2199	0.25 μm	
		Copperas Red Iron Oxide R3098	0.3 μm	
		Copperas Red Iron Oxide R6098	0.6 μm	
		Copperas Red Iron Oxide R8098	0.9μm	
		Copperas Red Iron Oxide R9998	2.5 μm	

In addition to viewing particle size, it is possible to identify the basic composition of particles in an SEM by examining x-rays emitted by the surface when charged by the electron beam. These x-rays have wavelengths that are characteristic of particular atoms in the structure of the molecules in the particle, so it is possible to identify what elements make up the portion of the sample under the beam. While not as rigorous a determination as other methods, this is sufficient for verifying if a particle is indeed what the manufacturer identified it to be or not.

Iron oxide, however, has many polymorphs which cannot be identified by this method. The compositions of the six iron oxide samples were verified by x-ray diffraction (XRD), also at the Materials Sciences department at the University of Pittsburgh. The samples for XRD analysis were prepared by pouring a small amount of the powder into the sample holder, which was taped to a glass slide. The powder was packed into a gap in the sample holder (against which the slide was pressed). After packing, a clip was placed behind the sample to keep it in the holder, and the holder put into the XRD chamber. For each sample, data was acquired from 15 to 75 degrees ("2□"). After data acquisition, XRD peaks were compared to those in a standard library to determine what compositions were present in the material.

While each manufacturer gives an average particle size for the powder in question, it was desirable to verify the manufacturer's values and also determine the size distribution. In order to better identify the particle size, and to obtain the particle size distribution required for later numerical modeling, additional analysis was performed. Each of the samples used in the study was analyzed using an automated SEM particle counting system. In order to do this, samples had to be prepared such that the particles were well separated. This set of analyses took place at R.J.Lee Group in Murraysville, PA under the direction of Dr. Stephen Kennedy. First, a small amount of a sample was added to a beaker of methanol, which was subjected to sonication for

1-3 minutes. For the aluminum oxide and calcium carbonate, this appeared to be sufficient to disaggregate the particles. The iron oxides, however, did not separate as easily. For these samples, a surfactant was added to the methanol prior to sonication. Just after sonication, the liquid in the beaker was subjected to a shear stress by a Hamilton Standard milkshake mixing machine (see Figure 4).

After the particles had been sufficiently dispersed by the above methods, the liquid in the beaker was poured into a vacuum filtration unit that was fitted with a 0.22 μm polycarbonate mesh filter. The methanol was drawn through the filter by the vacuum, and then the filter was allowed to dry. The dried filter was placed under an optical microscope to determine if the particles were well-dispersed enough for the automated analysis; if there were too many particles that were too close together, a small piece of the filter was removed and used as the starting point for another filter preparation. If the particle distribution was adequate, then a small piece of the center of the filter was removed and mounted on an SEM stub. These stubs were coated first with suspended graphite, and the piece of the filter paper placed on this while the stub was still wet. After drying, the filter sufficiently adheres to the stub, which is then coated with a few nanometer thick layer of carbon to provide the charging surface necessary for SEM imaging.

The automated counting process can be programmed to identify both particle dimensions and compositions. Particles can be counted into "bins" based on user-identified parameters; particles were binned based on their compositions as noted by x-ray analysis during counting. This way, contaminant particles that were introduced during sample preparation could easily be separated; in particular, SEM analysis of the samples prior to automated counting noted pieces of Pyrex (from the beaker) and human skin flakes present in the sample. Additional setup parameters include the x-ray parameters for elements expected in the sample, the length of the

Figure 4: Image of shear stress generator used during CCSEM sample preparation (e.g. Hamilton Beach Mixmaster milkshake machine).

run (either by number of particles counted or length of time), the frequency at which SEM images would be saved, and the particle parameters to be measured. The parameter files used were the same for both iron and aluminum oxides; additional changes were made for the precipitated calcium carbonate samples, which were added to the analysis later.

The last portion of the run setup involved setting the run parameters on the sample stage in the SEM. The stage was set to a working distance (distance between the beam source and the sample) of 18 mm; this distance is large enough to allow for approximate x-ray compositions, but also small enough to get decent images for counting purposes. A quadrilateral area on each stub was identified for counting using the movable stage; the corners of the area were set to locations that were well away from the edge of the filter paper, and each location was identified by an x, y, and z stage location. The z-location controls the focus of the image, which is important for identifying particle edges. Particles are identified because they are brighter than the background (the "detect" brightness value), and the edges are identified by the location of a certain minimum brightness (the "measure" value, usually lower than the "detect" value). The values of the detect and measure parameters are set prior to the run, and are consistent for each particle composition (different values were used for the iron oxides, aluminum oxides, and precipitated calcium carbonates).

The counting process, once set up, is completely automated. The routine identifies the quadrilateral area noted during run setup. This area is broken up into a grid; boxes on this grid are randomly selected for analysis. Once a box is chosen, it is broken up into a second grid of four by four. Each quadrant is searched for "bright spots" that exceed the brightness value set in the 'detect' parameter. If a bright spot is identified, it is analyzed both for particle size (by determining the area enclosed by the 'measure' brightness value) and via x-ray composition. If

there is sufficient energy to identify the particle composition, then the dimensions (largest diameter, smallest diameter, area, and average diameter) are saved into the composition bin appropriate for that particle. Images are saved occasionally throughout the process. Counting continues until either the required number of particles have been counted, or the run time has elapsed; in all of the samples analyzed here, the run time of 2 hours elapsed before the limit of 5000 particles were counted. Results from this automated size analysis will be referred to as "CCSEM data" in forthcoming sections.

In order to verify the automated particle counts, a series of "hand" counts were made on the SEM images taken at the University of Pittsburgh. As the sample prep for these SEM images did not involve significant dispersion of particles, the imaged particles had to be separated for further image analysis. This was accomplished in Adobe Photoshop® by drawing outlines of particles in different layers, filling in the outlines, and then separating the drawn particles before combining the layers into a final image. Multiple images were used for each sample; in some cases higher resolution images covered the same area as portions of lower resolution images. In these cases, the particles counted in the high resolution image were excluded from the low resolution image. This counting image contained only grey shapes that represented the particles in the original image, and a scale bar. This greyscale image was then imported into NIH Image, a freeware image analysis program (available online at http://rsb.info.nih.gov/nih-image/). The program must first be given a scale, which was accomplished by determining the length of the scale bar in pixels and the labeled length in microns from the original image. The image is then thresholded so the particles appear in black and the background appears in white; given the nature of the images used for counting, this is a straightforward process. The counting images contain either grey particles or white background, and there is no gradation within the grey; the

thresholded image is identical to the original, except in color. The analysis algorithm identifies single blocks of black in the thresholded image, and performs measurements on that particle. For this analysis, the program was asked to return the perimeter of the particle outline, the x/y coordinates of the center of a best-fit ellipse, and the lengths of the major and minor axes of that ellipse. The axes of these ellipses were taken to be the largest and smallest diameters of the particle, and the average of these two was taken as the average diameter of the particle in question. The results were exported to a spreadsheet, and were combined with results from other images of the same sample to produce a final size histogram.

Results

Particle morphology, while an important factor in the scattering of light, is assumed to be spherical in the fundamental scattering model calculations made in this study. The importance of examining the shape was more to determine how close to spherical each particular composition tends to be and to identify if the particles tend to be separate or adhered together in clumps. Again, while each manufacturer gives approximate shapes for their particles, SEM analysis was completed to confirm these shapes. Representative images are shown in Appendix 1. For the aluminum oxides, images show that the smaller particle sizes consist of hexagonal platelets, often grouped in large "stacks". Adhering to these stacks are a multitude of smaller quasi-spherical particles. The larger particles are irregular in form, appearing mostly sub-rounded to sub-angular, with a few angular pieces. The shapes tend to be roughly equant, although the few angular pieces tend to be elongated. The transition between the two morphologies corresponds directly to the change in product number: the 1.0 μm and smaller samples are hexagonal plates, while the 2.1 μm and larger samples are irregular and usually not clumped together. This finding is directly opposite to the particle morphology comments made by Nelson *et al.* (2000), which

were based on the manufacturer's description rather than on direct imaging results. This morphology change also coincides with interesting changes in the scattering parameters, as discussed later.

The morphologies of the iron oxide samples are simpler: it would be difficult to identify which sample corresponds to which image without a scale bar or label. The iron oxides are commonly well rounded, and the particles again tend to be close to equant. There are more elongate particles than in the aluminum oxides, but these do not represent a majority of the sample. It has been noted, however, that the iron oxides are extremely clumpy on all scales: the sample commonly forms millimeter-sized clumps in the sample cup and container, and clumps of particles are easily visible in the SEM images. The resulting effect of these clumps on the scattering parameters remains to be determined.

Because of time constraints, the calcium carbonates were not imaged with the high resolution SEM at the University of Pittsburgh, so the lower resolution images from CCSEM counting were the only ones available for particle morphology determination. These images show that even with the particle separation procedures used for sample preparation, the particles in these samples often clump together. Where well-focused images of the clumps were obtained, many of the clumps appear to be aggregates of particles shaped like a plus-sign (+): these particles, though relatively "equant", are in no way rounded or spherical. There are some rounded particles visible in the images as well (and clumps of apparently rounded particles), but it is clear from even the lower resolution CCSEM images that the calcium carbonates are the "least-spherical" of the three compositions. This may be the cause for some of the oddly shaped single scattering functions derived for these samples. It may be that the calcium carbonates were not sufficiently dispersed prior to CCSEM analysis, and that some aggregates were measured.

Clearly, however, regardless of the particle composition, an assumption of spherical particle shape would not be valid.

The particle size analysis did not provide as many answers as it did more questions. From the particle shape analysis, it was clear that some of the manufacturer's labels were inaccurate (for example, it was difficult to find a 2.5 μm particle on the SEM images of the labeled 2.5 μm iron oxide). While the automated counting method (CCSEM) used was able to count a large number of particles and classify their basic elemental compositions, the results of this method are suspect. The average particle sizes determined for the smaller (< 1 μm) particle sizes via CCSEM were larger than the label size, and were similar in value despite the differences in the labeled sizes. This is most likely the result of the particles being smaller than the practical resolution of the method: while it might be possible to image these small particles with the microscope used, this requires a high resolution which is not practical for automated counting. When the size is smaller than a micron, the CCSEM tends to overestimate the size, as the resolution of the scanning electron microscope used in the CCSEM counting, which is limited to perhaps 0.2 μm at the best (it is possible to resolve the 0.22 μm holes in the filter paper). Given this limitation, it is not surprising that analysis of these very small particles is difficult. In addition, CCSEM analysis for the largest five aluminum oxides, with labeled sizes between 5 and 30 μm, produced results with averages around 0.7 μm, which are much smaller than the given sizes. From the SEM images, it was clear that these particles are in fact larger than the reported CCSEM sizes, so the automated counts were discarded. Although no conclusive reason for this discrepancy was identified, it appears likely that the instrument was not properly configured for these large sizes and therefore produced a spurious result.

Regardless of the cause for the error, the CCSEM results for the largest aluminum oxide particle sizes were rejected because of the inconsistency with the high resolution SEM images.

While a majority of the CCSEM results appear to be suspect, results from hand counting from SEM images do not appear to be significantly more accurate. While the values for the smaller particle sizes are more consistent with the label sizes, they tend to be smaller; this suggests some bias toward smaller particle sizes or an error in measurement technique that tends to produce smaller resulting sizes. Given the lack of separation of the particles on the SEM images, it is easily possible that larger particles were occulted by multiple smaller ones, meaning the small particles are preferentially outlined and counted. This is especially common in the smaller particle size samples, where the particles tend to clump together more than in the larger sizes. In addition, the depth of the field of view may not be sufficient to outline the largest particles. Instead, small protrusions on the particle are visible while recessed areas are not, leading to errors in discriminating between the two. Given these factors, it is likely that the SEM size estimates, whether automated or hand counted, are no more accurate than the average sizes and distributions given by the manufacturer. Comparison of the SEM and CCSEM size distributions with the manufacturers' labeled sizes is shown in Figure 5.

Acquiring average sizes and distributions from the manufacturer did not prove helpful, either. Each manufacturer provided a particle size for each sample upon original purchase, along with both a product number and a lot number. Information about particle size obtained from the manufacturer at a later time (a few months or years later) suggested results that were different from the original labeled sizes for some of the samples (at least one per composition and manufacturer, in fact). This presented a problem: whether to believe the results given at the time of purchase, or the results given at a later time. The later results might reflect a more

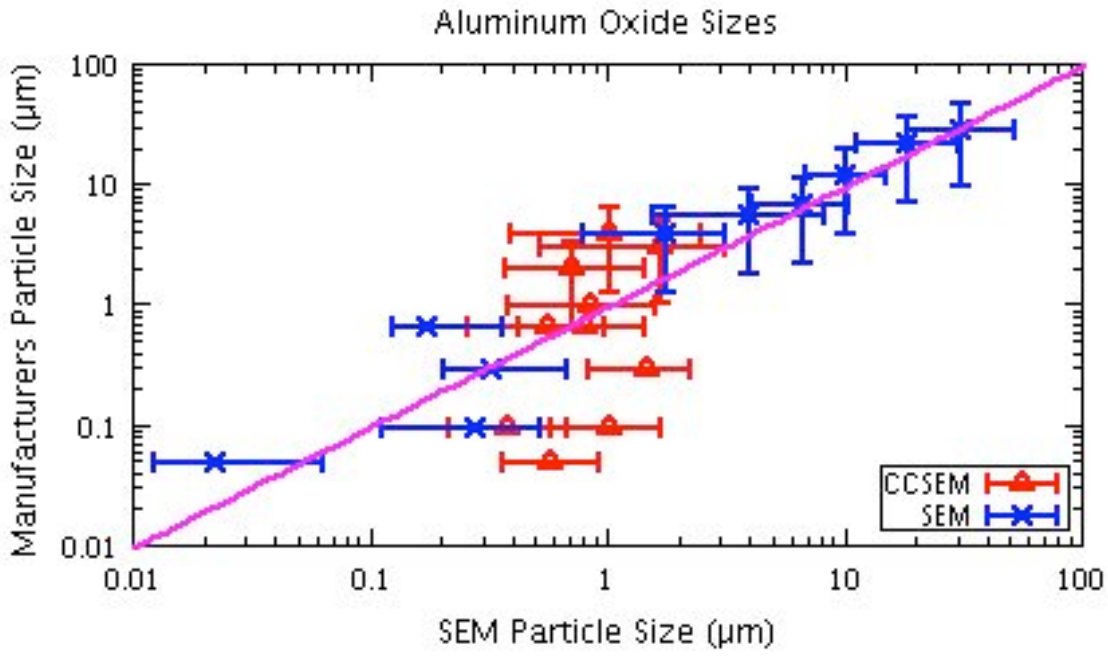

Figure 5a: Comparison of SEM/CCSEM size results (x-axis) and manufacturer's distributions (y-axis) for aluminum oxide. Both axes are plotted on a log-log scale. Points are placed at the value of the peak of the size distribution (or at the labeled size if no distribution is given), and error bars indicate the half power points of the distribution. The solid purple line has a slope of 1, indicating where the points should fall if the labeled sizes and SEM results agreed.

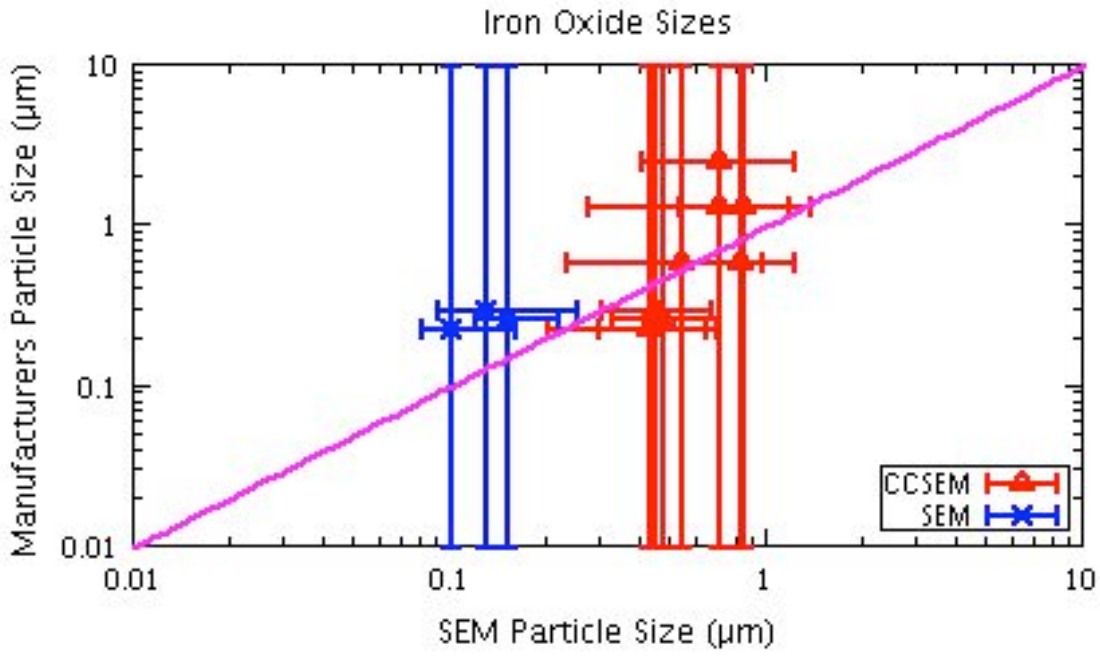

Figure 5b: Comparison of SEM/CCSEM size results (x-axis) and manufacturer's distributions (y-axis) for iron oxide. Both axes are plotted on a log-log scale. Points are placed at the value of the peak of the size distribution (or at the labeled size if no distribution is given), and error bars indicate the half power points of the distribution. The solid purple line has a slope of 1, indicating where the points should fall if the labeled sizes and SEM results agreed.

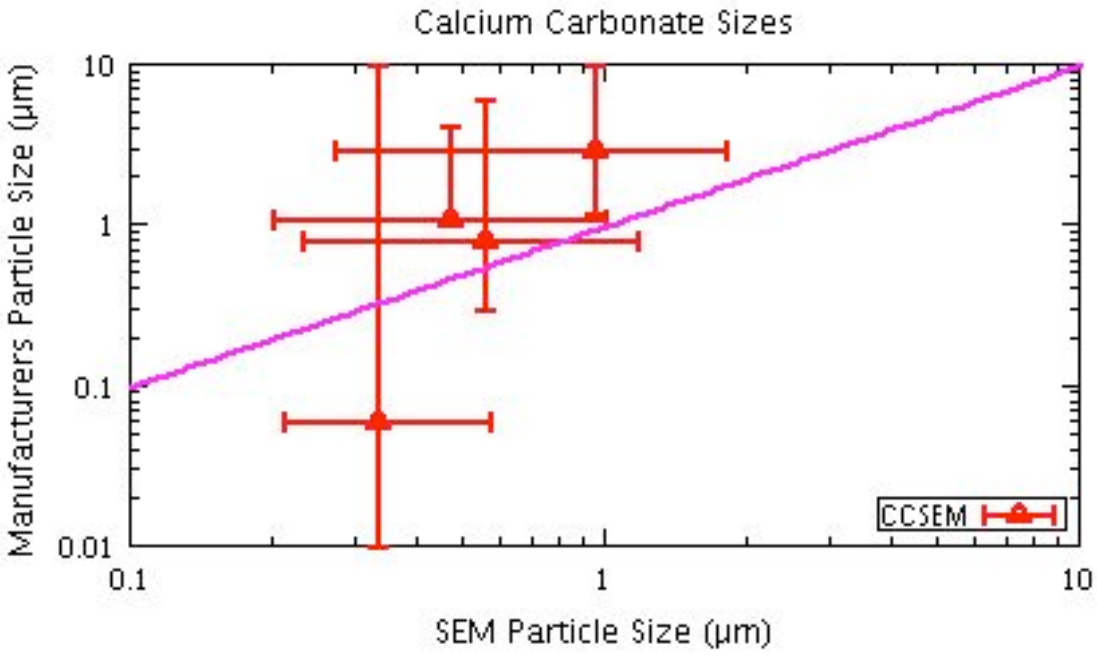

Figure 5c: Comparison of CCSEM size results (x-axis) and manufacturer's distributions (y-axis) for calcium carbonate. Both axes are plotted on a log-log scale. Points are placed at the value of the peak of the size distribution (or at the labeled size if no distribution is given), and error bars indicate the half power points of the distribution. The solid purple line has a slope of 1, indicating where the points should fall if the labeled sizes and SEM results agreed.

accurate method of particle sizing, or they may reflect a change in manufacturing method that could lead to a change in the actual distribution of the sample (or both). Because the later results were taken on different lot numbers, it is impossible to determine what caused the change in the labeled size. For this reason, the labeled sizes used here are the original labeled sizes given for each sample at the time of acquisition: later modifications by the manufacturer are ignored. (This is a variation from the results of Nelson *et al*. (2000), who published long arm goniometer phase curves for the aluminum oxides: those results use later size estimates for the smallest particle sizes that are different from the numbers given here. These results are in fact from the same samples, however, regardless of what particular size is ascribed to which sample: the smallest five aluminum oxide samples used here are equivalent to the smallest five sizes used in that particular study. The larger sizes are listed by the same size in both sets of results. The sizes used in Nelson *et al*. (2000) are listed in Table 2 next to the corresponding sizes used in this study).

It was felt that the manufacturer's labeled sizes were within the uncertainties of the size distributions determined by both automated and hand counting methods. Since size distributions were not available for all samples, however, it was not possible to simply rely on the manufacturer's published data. In order to estimate the size distributions of the samples, the distributions determined by both counting methods described above were examined, and an average distribution for each group of similar samples was estimated. The smallest 5 and largest 8 aluminum oxides were grouped separately, taking into account both the particle morphology differences, and the different product numbers assigned by the manufacturer. The iron oxides and calcium carbonates were grouped together by composition. The resulting distributions,

examples of which are shown in Figure 6, have the manufacturer's labeled particle size as the peak of the distribution, and these were used in the Mie theory results presented later.

The composition of the aluminum oxides and precipitated calcium carbonates were well documented in the manufacturer's literature. The iron oxides, however, were not as well documented. The composition analysis for these samples shows that all 6 samples have roughly the same composition, as the XRD results for all 6 samples are nearly indistinguishable. These XRD peaks are very consistent with results for hematite or synthetic iron oxide found in the XRD library. However, these results are also consistent with the peaks for iron hydroxide oxide, and also for nickel titanium oxide. Considering, though, that a majority of the SEM x-ray results for the iron oxide samples suggest that they do contain iron, and only a small fraction of particles contain titanium, the iron oxide result seems the most consistent. The presence of iron hydroxide oxide is hard to rule out, but the chemical formula for this compound ($Fe_{1.833}(OH)_{0.5}O_{2.5}$) is similar enough to hematite (Fe_2O_3); this difference appears negligible, and the samples can be considered as hematite.

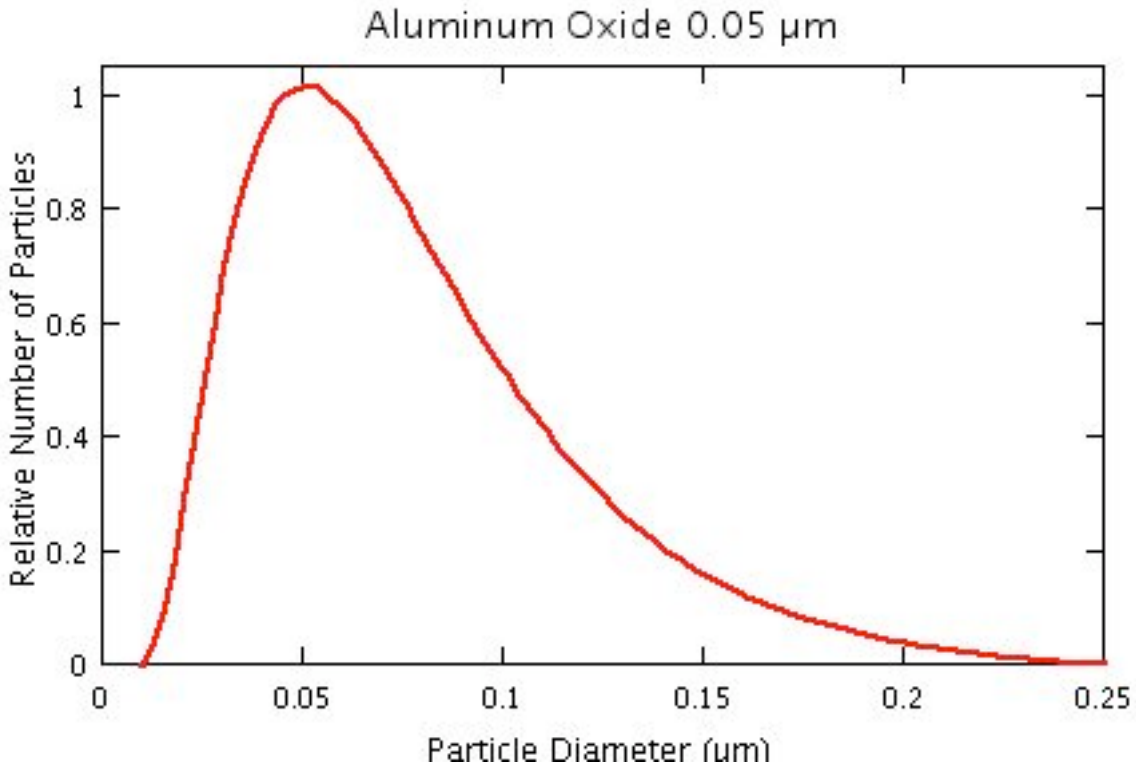

Figure 6a: Estimated size distributions for representative samples. Size distributions for other samples are similar in shape to these shown, with the manufacturer's labeled diameter at the peak of the curve. Shown above is the result for the 0.05 μm aluminum oxide, which is representative of the distribution used for the 5 smallest aluminum oxide samples ($\leq$ 1.0 μm).

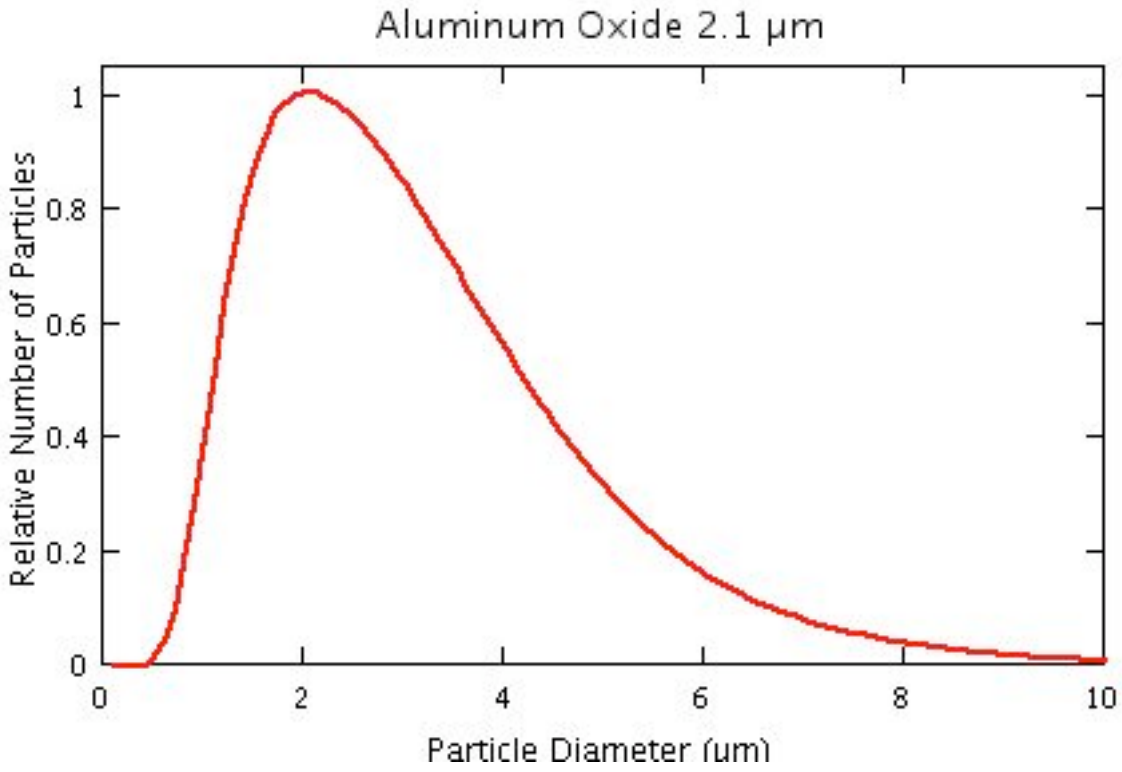

Figure 6b: Estimated size distribution for aluminum oxide, 2.1 μm. Representative of the distributions used for the largest aluminum oxides (≥ 2.1 μm).

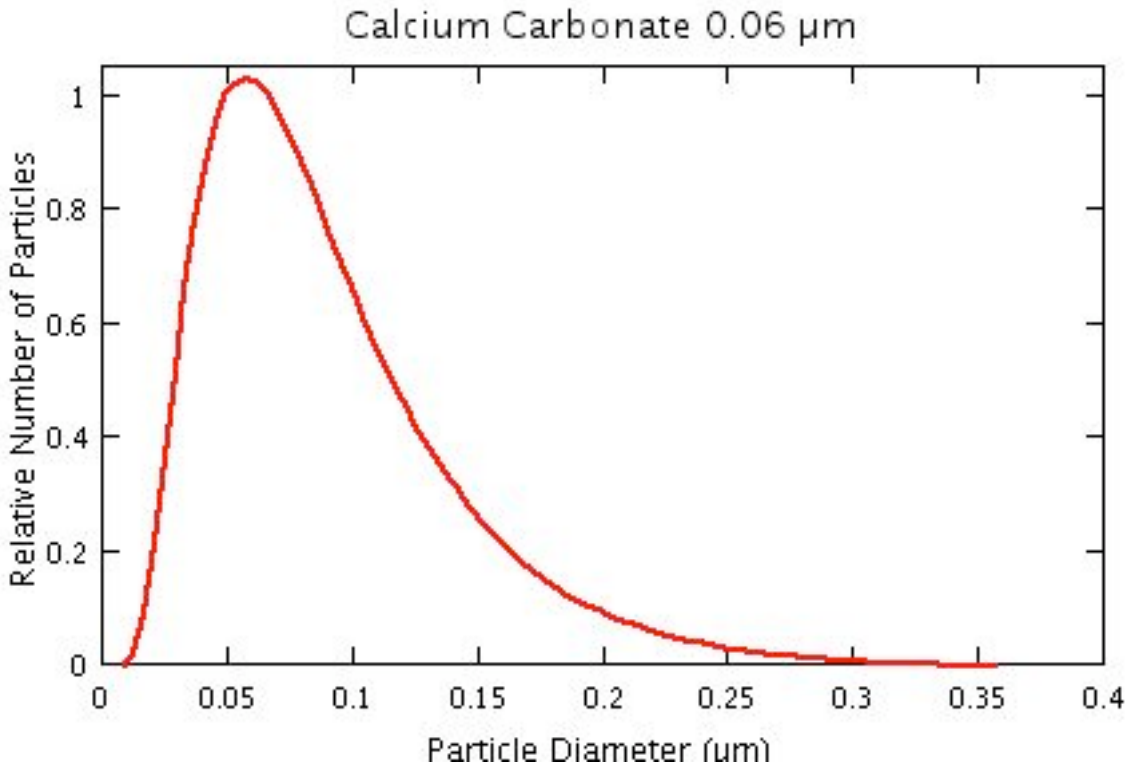

Figure 6c: Estimated size distribution for calcium carbonate, 0.06 μm. Representative of the distributions used for all the calcium carbonate samples.

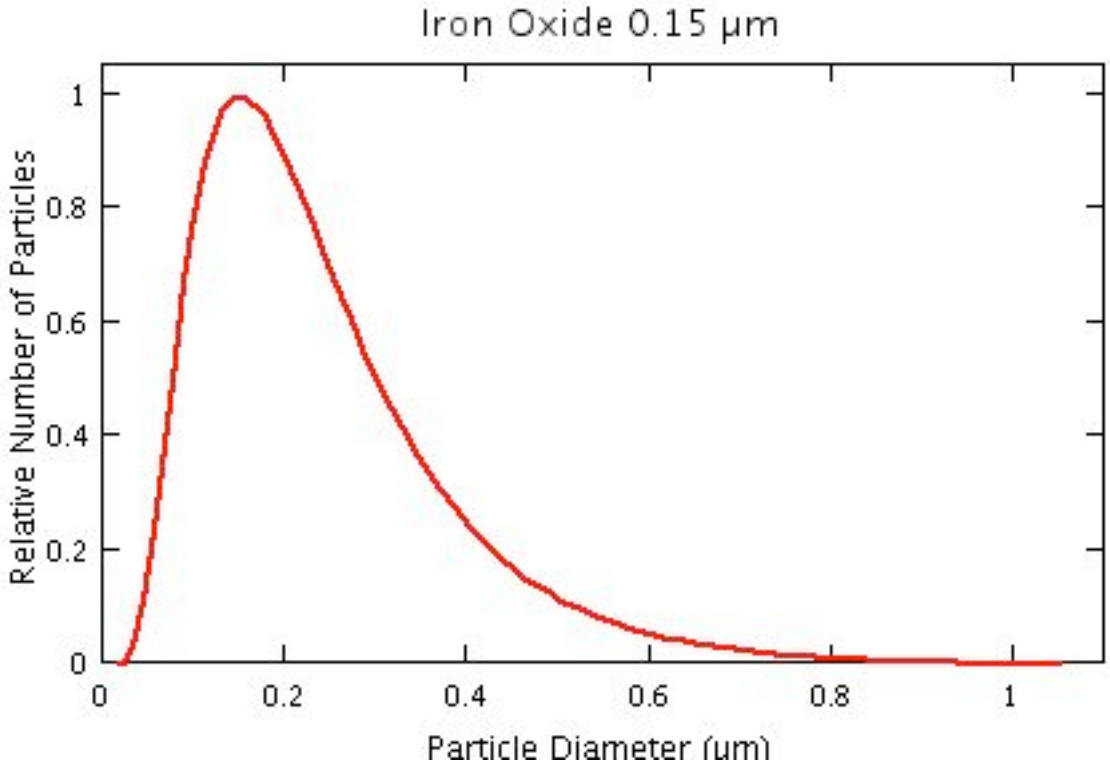

Figure 6d: Estimated size distribution for iron oxide, 0.15 μm. Representative of the distributions used for all the iron oxide samples.

Instrumentation

Introduction

The intent of this study is to identify the changes in light scattering parameters as the particle size of a sample changes. In order to characterize these scattering parameters, it is necessary to measure the reflectance in both linearly and circularly polarized light at a range of phase angles from very small to very large. An instrument that is capable of measuring light in various polarizations is a 'photopolarimeter', and an instrument that can measure a quantity at different angles is a 'goniometer'; thus the instruments used here are best termed 'goniometric photopolarimeters'. For simplicity, they are referred to simply as goniometers. Two different such instruments were employed; one capable of measuring reflectance at very small phase angles, and one that measures over a large range of phase angles.

The ability of a goniometer to measure at different angles depends on the distances from the sample to the light source and detector, which are both supported by arms. If an arm is long, then the end of the arm away from the fulcrum will travel further to get the same angular change; the difference between two very small angles on an instrument with short arms may appear indistinguishable, but will be obvious on an instrument with long arms. Thus, the instrument with the longer arm is better at measuring at smaller angles. Practically, however, it is difficult to then manage this arm at larger angles, as the distance the arm must travel is much greater. For these reasons, two instruments with different arm lengths were employed here: the "long arm" goniometer has an arm length of 2.3 m, and the "short arm" goniometer has an arm length of 1 m. Each instrument is described in subsequent paragraphs. All goniometer data presented herein were taken at the Goniometer Laboratory at the Jet Propulsion Laboratory under the direction of Drs. Robert Nelson and William Smythe, and with the assistance of Dr. Amy Snyder Hale.

The Long Arm Goniometer

The long arm goniometer, described in Nelson *et al*., 2000, has an arm length of 2.3 m, as stated earlier. A diagram and photograph appear in Figure 7. The incidence angle of the instrument (i) is fixed at 0°, and the detector angle (e) can be varied from 0° to 5° in increments as small as 0.05°. Because of obscuration of the source by the detector at very small phase angles (below 0.05°), the effective phase angle range is 0.05 – 5°. The source is a Melles Griot 5 mW helium-neon stabilized laser with an output wavelength of 635 nm (putting it in the red portion of the visible spectrum). The laser light first passes through a chopper with a frequency of approximately 105 Hz; the chopper also provides a reference signal to the output Stanford Research Systems SR830 lock-in amplifier. The chopped light then passes through an optical filter that alters the linear polarization. The original setup (which was used to acquire the aluminum oxide long arm data of Nelson *et al*. 2000) had a linear polarizer in this position that could be rotated so the incident beam polarization direction was either parallel or perpendicular to the scattering plane. A later modified setup replaced the linear polarizer with a half-wave plate, and used a stabilized laser, whose direction of polarization and intensity output are more constant than that of a standard laser. The laser polarization direction is set to one desired position, and the half-wave plate (which rotates the plane of polarization by 90°) is placed in the beam when the orthogonal polarization is desired. This also has the effect of allowing more light to reach the sample than when a linear polarizer is used, as the half-wave plate allows a higher percentage of light to pass through it. All of the data taken for this study were acquired after the modification that added the half-wave plate and stabilized laser.

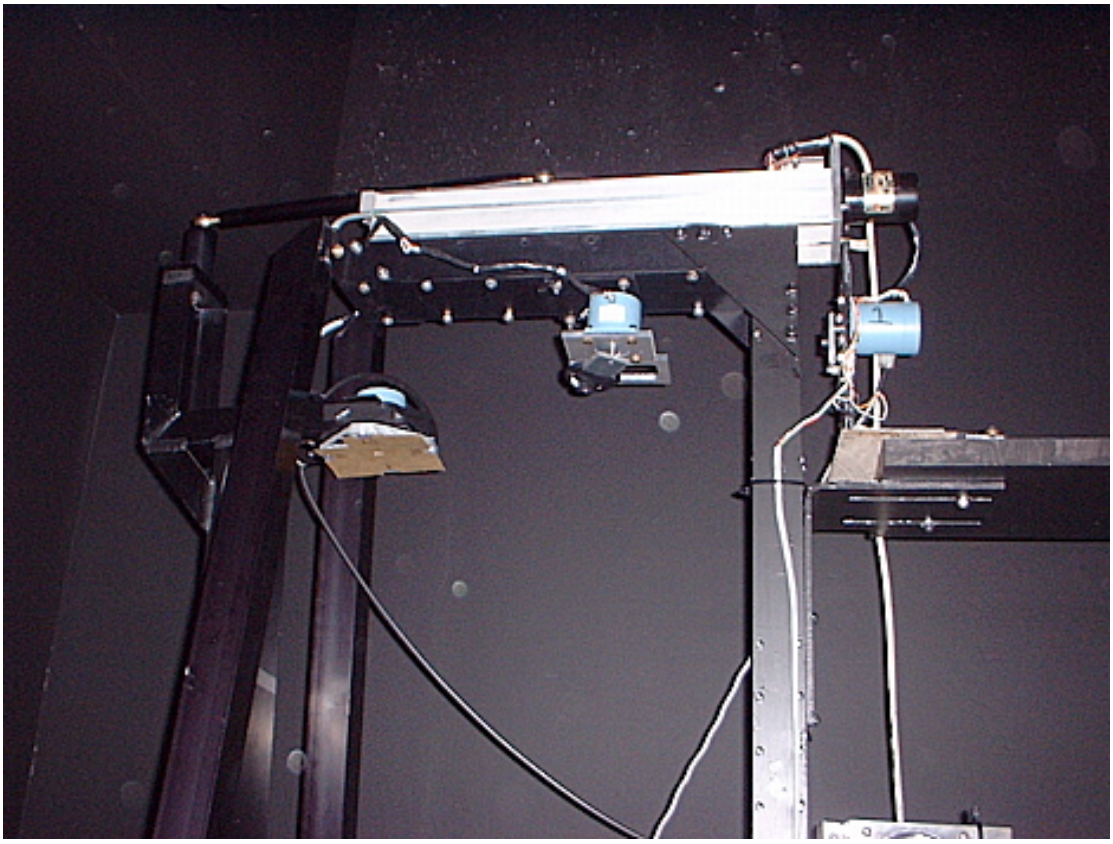

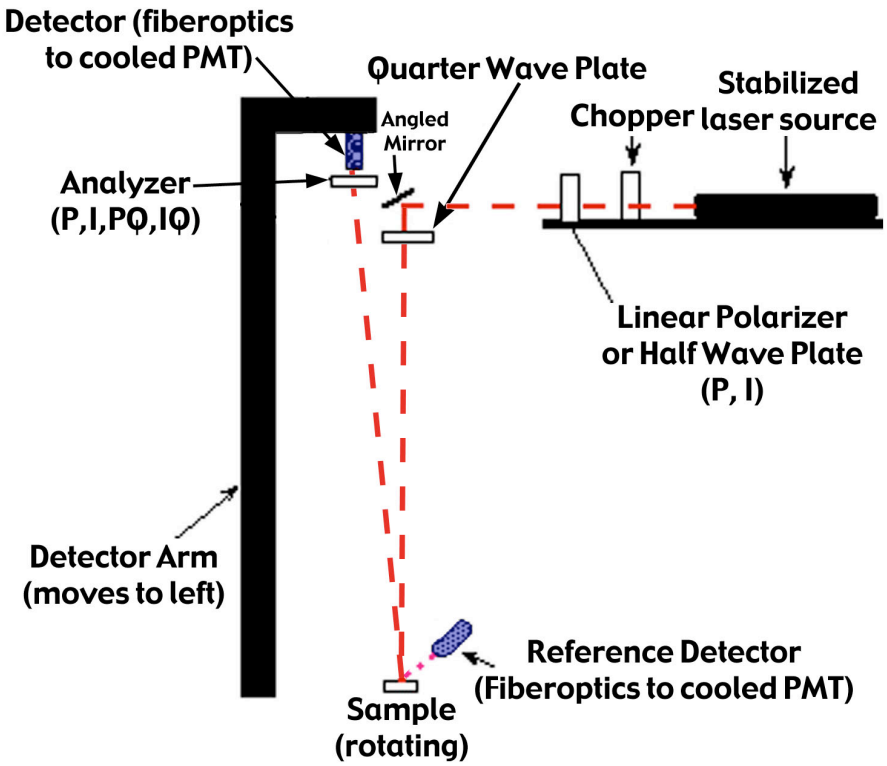

Figure 7: Photograph and diagram of JPL long arm goniometer.

After passing through the polarizer/half-wave plate, the light beam direction is changed by 90° at a first surface mirror so that it is incident upon the sample. A quarter-wave plate is inserted in the beam path after the mirror when circular polarization is required. The sample is placed in a cup sitting in a holder that is rotated at 12 RPM about the axis normal to the sample surface, at the center of the sample. This spinning helps to average out the effect of laser "speckle", which is present with a non-rotating sample. The sample cup used for a majority of the samples used in this study is 3.5 cm in diameter and 0.9 cm deep: one sample (aluminum oxide, 0.05 μm) was run in a smaller 2.4 cm diameter sample cup. The sample is poured into the cup, and the cup tapped to level the surface and break up any clumps. Ideally, the surface of the sample is level with the edge of the cup. Care is taken not to overly compact the sample, as the aim is to retain the loose structure characteristic of a planetary regolith.

After reaching the sample, the collimated light from the laser is scattered. An analyzer plate sits in front of the detector optics; this plate contains four sets of polarizers (two linear and two quarter wave plates plus linear polaroids) so that the detector can either be exposed to light in the same or opposite sense of polarization as the light incident on the sample, either linear or circular. The detector is a RCA 1P21 photomultiplier tube (PMT) fed by a fiber optic cable fitted with a lens and a notch filter, which is tuned to pass only a narrow bandwidth centered at 0.635 μm. One end of the cable is mounted at the top of the moveable arm, allowing the angle it makes with the surface to be varied. The cable outputs into a Products for Research, Inc Model PC202TSRF temperature stabilized housing (fixed at –10° C) that contains the PMT. The signal from the detector PMT is passed to a Stanford Research Systems SR830 lock-in amplifier which is synchronized to the chopper. Only the component of the signal that has the same frequency as the chopper is passed by the amplifier, and the result is stored on a personal computer (PC). The

combination of notch filter and chopper/lock-in amplifier reduces the effect of background light to below detectability. A reference detector is also employed to reduce the effect of noise in the signal introduced by laser output variations; comparisons of laser output with ambient temperature suggest that a change in ambient temperature of only a few degrees can produce observable changes in the laser output. The reference detector is identical to the primary detector (a second RCA 1P21 PMT cooled with a similar Products for Research, Inc Model PC202TSRF photoelectric cooler, attached fiberoptic cable and notch filter), and is connected to a second Stanford Research Systems SR830 lock-in amplifier synchronized to the chopper. The detector cable views the sample from a fixed position at a height of approximately 1 m, and collects any light scattered from the sample in this direction.

The analysis software for this instrument was written in QBasic®. It controls the movement of the polarizers, wave plates, and detector arm via stepper motors. Delays are written into the program so that all motions are complete and vibrations have ceased prior to any data collection. The run is completely automated, and takes readings in 8 senses of polarization before incrementing to the next phase angle position. Each reading is the average of three datapoints taken at each position, where each datapoint represents the average of 400 computer readings of the amplifier output. The readings from the primary and reference detectors, the ratio of the primary over the reference, the phase angle, and a number representing the detector position are outputted to a text file for later analysis. The detector arm begins at 0° phase, and is moved in increments of 0.05° until a phase angle of 2° is reached, and then it moves in larger increments of 0.1° until the maximum phase of 5° is reached. The software can perform multiple runs per session; the instrument is set back to a phase angle of 0°, and data collection begins again.

The Short Arm Goniometer

The short arm goniometer is set up in much the same way as the long arm, with a few differences (an earlier setup was described and used by Nelson *et al.*, 1998). A photograph and diagram appear in Figure 8. In this case, the Melles Griot helium-neon red laser used does not have a reliable polarization plane, so a linear polarizer is used instead of a half-wave plate. The laser is mounted on a tabletop that can be tilted so the incidence angle (i) can be varied from 0° up to 70°. The detector arm can be moved in increments as small as 0.5°, and can vary the viewing angle (e) from 0° to 90° on both sides of the vertical. The practical phase angle range of the instrument is 5°-140°, using an incidence angle of i=60° and a viewing angle range of e=55° on the same side as the light source to 80° on the opposite side. The 5° lower limit is determined by obscuration of the detector by the source mirror. The output beam from the laser goes first through a chopper (which again provides a synchronization signal to a lock-in amplifier), and then encounters an angled first surface mirror so its path is changed by 90°. Just after bouncing off the mirror, the beam passes through a polarizer wheel, which consists of a linear polarizer with two quarter wave plates attached underneath (so the light passes through the linear polarizer before the quarter wave plate in two of the wheel positions). The polarizer is aligned so that the direction of polarization is either parallel or perpendicular to the scattering plane, depending on its orientation. With this setup, the polarization of the beam can be varied in four ways (two linear, two circular). This entire setup (laser through polarizer wheel) is affixed to the tabletop, and can be tilted to vary the incidence angle.

After passing through the polarizer, the beam hits the rotating sample. The sample cup used has the same dimensions as the one used in the long arm. The detector is fixed to the top of the detector arm. The scattered light first passes through an analyzer wheel similar to the one on

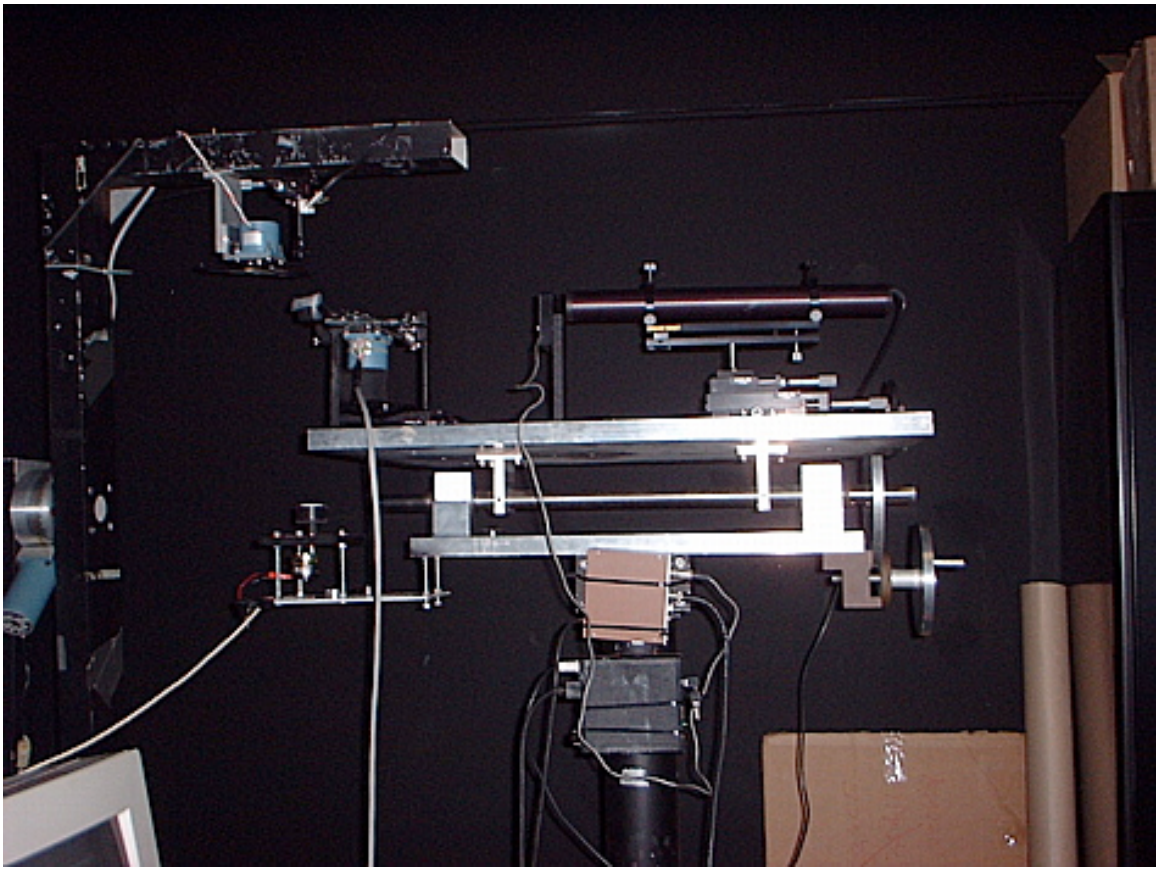

Figure 8: Photograph and diagram of short arm goniometer.

the long arm (four senses of polarization, identical to the ones on the input polarizer wheel as well), and then through a similar notch filter (which, again, only passes light in a narrow passband around 0.635 μm). The detector in this case is a photodiode, which outputs directly to a Princeton Applied Research Model 5101 lock-in amplifier. The lock-in amplifier is synchronized by the chopper, and outputs only signal with that frequency. This signal is passed to an additional amplifier so that it may be read by a PC and written out to a text file.

The analysis software for this instrument is similar to that for the long arm, and was also written in QBasic®. The movement of the polarizer wheels and detector arm are controlled by the software, and delays are built in so that motions cease and vibrations have time to damp out before any readings are taken. In this software, the number of computer readings per datapoint is an input parameter, and can be varied to adjust the length of time a run requires; a minimum of 200 readings was found to be necessary to avoid any systematic variation in the reading due to sample spin (observed in runs taken with smaller numbers of readings per point). The angle of the detector arm is incremented in 0.5° steps from 0 – 10° phase, and then in 1° increments. Some data runs have an additional change of increment so that the arm moves in 5° steps beyond 90° phase, which was necessary to reduce run time. The software is also capable of doing multiple runs per session as desired.

Data Analysis and Calibration

Prior to the beginning of each session on both goniometers, a calibration measurement is made. This consists of measuring at 5° of phase (i=0°, e=5°) in all 8 senses of polarization a Labsphere Spectralon reflectance standard with an albedo of 0.992 at λ=635 μm, based on measurements made by the manufacturer in accordance with the American Society of Testing and Measurement standards. The sum of these values is used for calibration purposes during

data analysis. On the long arm, the sample is also measured in this same configuration. Note that the reference detector is ignored for these calibration runs.

Goniometer data from both instruments are analyzed using routines written in MATLAB®. Two different routines must be employed because of the differences between the two machines. For the long arm data, which may have multiple datapoints at each angle/detector setting, these datapoints are averaged first. A correction factor for the reference detector at each phase angle is calculated by averaging the value of the reference for each input polarization. The value of the ratio of the primary to reference detectors is multiplied by the correction factor for the corresponding input polarization. The values of each polarization are then saved in separate vectors, which can be plotted singly if necessary. The sum of all polarization values for each detector position is calculated and saved as the phase curve for that run. Multiple phase curves for each sample are averaged together. Extremely noisy runs are discarded (an example is given in Figure 9).

The analysis for the short arm is simpler, as there is only one datapoint per polarizer position and angle, and no reference detector. A reference detector would not significantly improve the quality of the results, as the variations observed over large changes in phase angle are much larger than the magnitude of the background noise. Readings for each polarization are saved as separate vectors, and the sum of all 8 polarizations at each detector position is also plotted versus phase angle to show a phase curve. Again, multiple curves for a sample are averaged, with the noisy runs discarded.

For both instruments, the value of absolute reflectance is calculated by using the albedo run. The detector readings for the 99% reflectance standard are summed, and this is divided into the phase curves described above. The result is a measure of absolute reflectance that is ideally

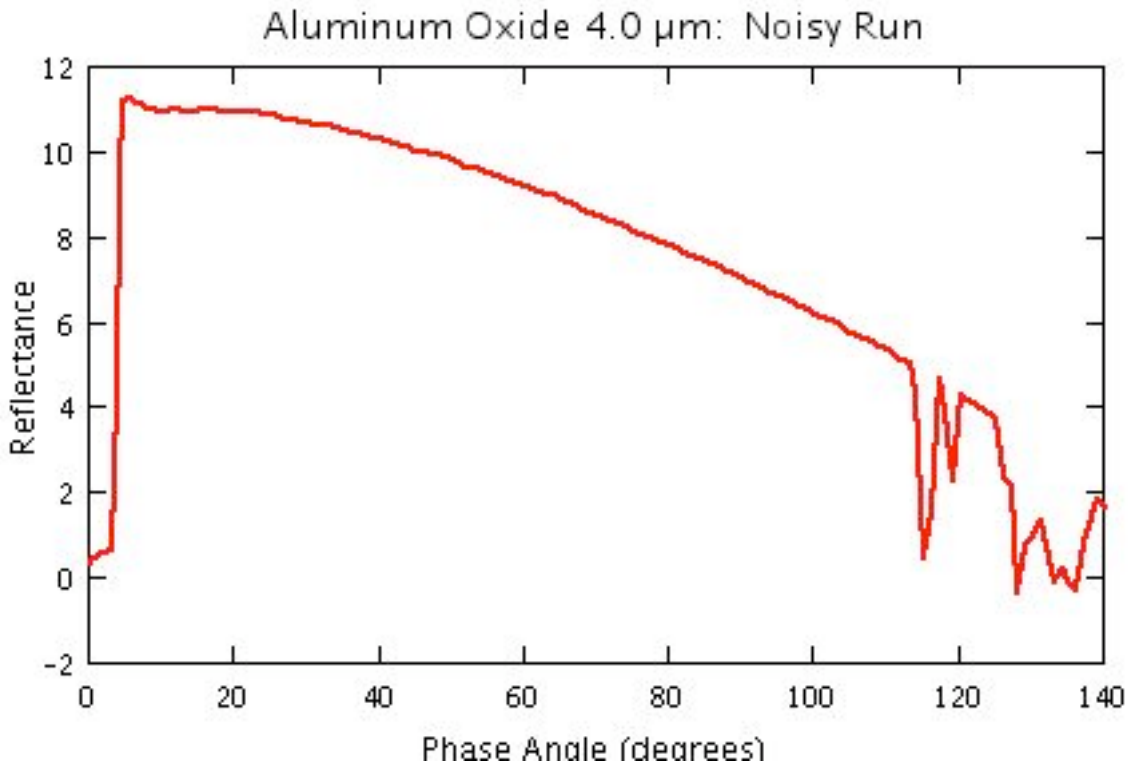

Figure 9: Example of a short arm run that was discarded due to excessive noise.

independent of the intensity of the source or sensitivity of the detector. The resulting phase curve should depend only on the geometry of the measurement and the scattering properties of the sample.

Scattering Parameter Determination

Model Curve Fitting

In order to determine the scattering parameters from the phase curve data, it is necessary to assume a model of light scattering from the surface. In this case, the improved RTE-based model of Hapke (2002) is used. All the equations below are taken from this model, and all variables are listed in Table 1 as well as described below.

The bidirectional reflectance of a surface in the model is defined as (Hapke, 2002, eq. 38):

$$r(i,e,g) = \frac{w}{4\pi}\frac{\mu_o}{\mu + \mu_o}\left[p(g)B_{SH}(g) + M(\mu_o,\mu)\right]B_{CB}(g) \quad (6)$$

where w is the single scattering albedo, μ is cos(e), μ_o is cos(i), p(g) is the single scattering function, $B_{SH}(g)$ is the contribution from the shadow-hiding opposition effect, $M(\mu_o,\mu)$ is a term that represents multiple scattering, and $B_{CB}(g)$ is the contribution from the coherent backscatter opposition surge. The single scattering function represents the power of the light deflected by a typical scatterer in the medium into a particular direction denoted by g relative to the power scattered into other directions. Because a material cannot scatter a negative amount of light, this function must be positive over the range 0° - 180°. The multiple scattering term M is defined as the following (Hapke, 2002, eq 17).

$$M(\mu_o,\mu) = P(\mu_o)\left[H(\mu) - 1\right] + P(\mu)\left[H(\mu_o) - 1\right] + \mathcal{P}\left[H(\mu) - 1\right]\left[H(\mu_o) - 1\right] \quad (7)$$

The H(x) function is an approximation for the Ambartsumian-Chandrasekhar H-function (Ambartsumian, 1958; Chandrasekhar, 1960), which is defined as the solution to the integral equation:

$$H(x) = \left(1 - \frac{w}{2} x \int_0^1 \frac{H(x')}{x + x'} dx'\right)^{-1} \tag{8}$$

Since this equation has no analytic solution, an approximation is required. The function (Hapke, 2002, eq. 13):

$$H(x) = \left(1 - wx\left(r_o + \frac{1 - 2r_o x}{2} \ln\left(\frac{1 + x}{x}\right)\right)\right)^{-1} \tag{9}$$

provides a good approximation (differing by no more than 1%) to the numerical solution to this equation (Hapke, 2002), and is used in this model. The term r_0 is defined as (Hapke, 2002, eq. 12):

$$r_0 = \frac{1 - \gamma}{1 + \gamma}; \quad \gamma = \sqrt{1 - w} \tag{10}$$

The remaining terms in the multiple scattering term M are derived from the single scattering function, and represent different geometries of multiply-scattered light. $P(\mu_0)$ and $P(\mu)$ represent the radiance of light scattered into either the upper or lower hemisphere by light incident on a scatterer from a direction defined by i or e (as appropriate). This formulation results from manipulation of the invariance equation, which evolves from the principle that the reflectance of the medium is not changed by adding an optically thin layer of material on top of it. The resulting form of these terms is (Hapke, 2002, eq.15):

$$P(\mu_0) = \frac{1}{2\pi} \int_{e=\pi/2}^{\pi} \int_{\phi=0}^{2\pi} p(g) \sin e \, de \, d\phi \tag{11}$$

where $p(g)$ is the single scattering function, and e' and ϕ are arbitrary angles within the hemisphere the light is scattered into. Essentially, $P(\mu_0)$ represents incident light that is scattered

into the medium (light incident with angle i scattered into the lower hemisphere, i.e. the sample), while P(□) represents the light that is scattered from the medium to the detector (light incident on the sample with angle e scattered into the upper hemisphere, or the opposite – as photons can travel a ray path in either direction). The remaining term ($\mathcal{P}$) defines the light scattered back into the lower hemisphere by a scatterer illuminated by the entire lower hemisphere, and is defined as (Hapke, 2002, eq. 16):

$$\mathcal{P} = \frac{1}{(2\square)^2} \int_{i=0}^{\square/2} \int_{\square=0}^{2\square} \int_{e=0}^{\square/2} \int_{\square=0}^{2\square} p(g) \sin e \, de \, d\square_e \sin i \, di \, d\square_i \tag{12}$$

where e', $\square_e$', i', and $\square_i$' are arbitrary angles within the hemisphere similar to those given in Equation (11).

Equations (11) and (12) are not simple to solve directly. However, if the single scattering function is expressed as a sum of Legendre polynomials, then an analytic solution can be achieved after some manipulation. The results below are the forms of these equations used in the phase curve models to follow (Hapke, 2002, eqs. 23, 24 and 25).

$$\begin{aligned} p(g) &= 1 + \sum_{n=1} b_n P_n(\cos g) \\ P(\square_0) &= 1 + \sum_{n=1} A_n b_n P_n(\square_0) \\ P(\square) &= 1 + \sum_{n=1} A_n b_n P_n(\square) \\ \mathcal{P} &= 1 \square \sum_{n=1} A_n^2 b_n \end{aligned} \tag{13}$$

The coefficient A_n represents constants that are defined by Hapke (2002, Table 1), and b_n is the coefficient of the Legendre polynomial in the representation of the single scattering function.

Complete expansions of the terms in Equation (13) for each different single scattering function used appear in Appendix 2.

The phase curve data collected show the reflectance of the sample measured at a number of phase angles within the principal plane relative to the reflectance of a Spectralon standard at a fixed geometry (i=0° and e=5°). The geometry for the sample is a fixed i, while e is varied in the principal plane (the plane containing the incident and scattered rays, as well as the normal to the sample surface). For the short arm data, the convention for relating e and i that will be used here is:

$$g = i + e \tag{14}$$

which assumes that e < 0 when the detector arm is on the same side of the instrument as the source, and e > 0 when on the opposite side. This convention is purely descriptive; since all angles in the model equations occur in cosine functions, the sign is irrelevant ($\cos(-\theta) = \cos\theta$). No such convention is required for the long arm, as i=0 and the detector arm is moved only in one direction to modify e.

The bidirectional reflectance of the standard was measured and was found to behave as a medium of isotropic scatterers, meaning that p(g) = 1. This is contrary to the assertion of the manufacturer, Labsphere, who claim that the material is highly Lambertian ("A Guide to Reflectance Coatings and Materials", available at http://www.labsphere.com). However, this statement appears to refer only to the directional-hemispherical reflectance, and not to the bidirectional reflectance. A plot of the phase curve of the standard, along with model phase curves for both an isotropic and a Lambertian surface, appears in Figure 10. Substituting p(g) = 1 into Equation (6) results in the following:

$$r_{standard}(i,e) = \frac{w}{4\pi}\frac{\mu_0}{\mu_0 + \mu}\left[H(w,\mu_o)H(w,\mu)\right] \tag{15}$$

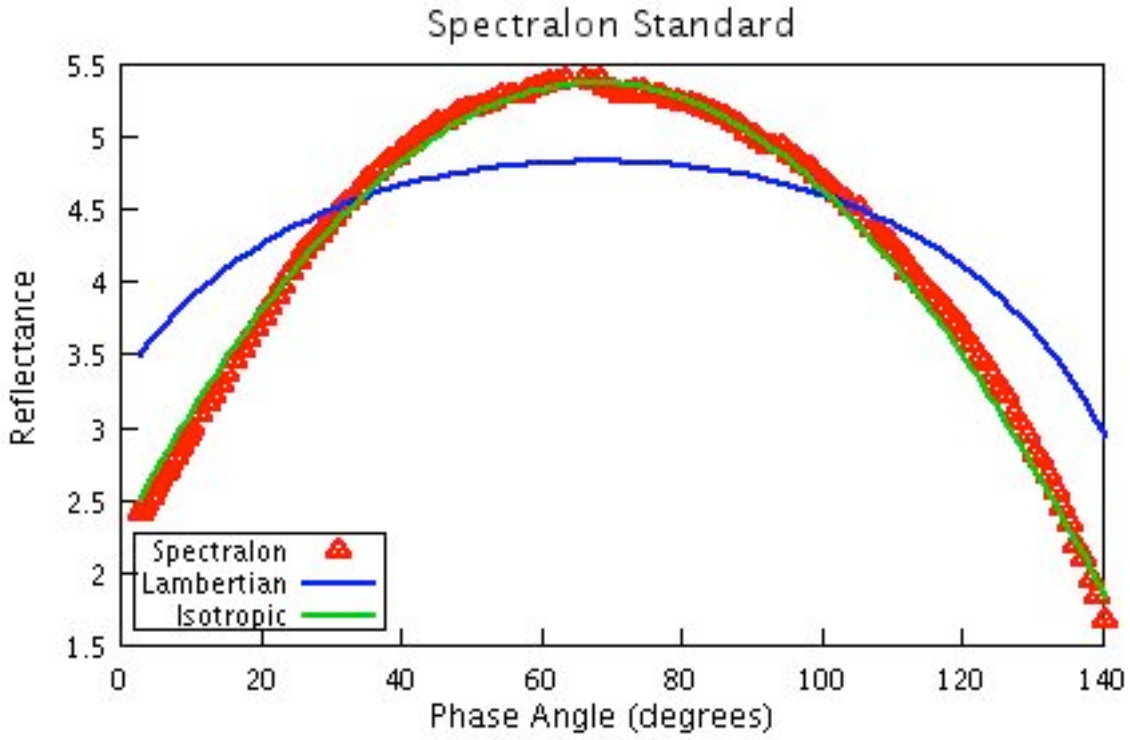

Figure 10: Phase curve for Spectralon reflectance standard, taken on the short arm goniometer with an incidence angle of 60°. Reference curves for a Lambertian and an isotropic scatterer are also shown.

where the values of μ_0 and μ depend on the viewing geometry. In this case, i=0 and e=5, so μ_0=1 and μ=cos(5°). The value of the single scattering albedo 'w' of the standard is discussed below.

The quantity J·r(i,e,g) is the radiance of light scattered from a surface illuminated by irradiance J over an area larger than that viewed by the detector. The light scattered per unit area of the surface is J·r(i,e,g)μ. In these experiments, the surface is illuminated by a collimated beam of light with cross-sectional area A_B, so that the surface area illuminated is A_B/μ_0. Although the detector views an area larger than A_B/μ_0, it is only sensitive to the scattered laser light. Hence, the intensity of scattered light incident on the detector is, using the formulation for r(i,e,g) given in Equation (15):

$$\begin{aligned} I(i,e,g) &= JA_B r(i,e,g)\mu/\mu_0 \\ &= JA_B \frac{w}{4\pi}\frac{\mu_0}{\mu_0+\mu}\left[p(g)B_{SH}(g)+M(\mu_0,\mu)\right]B_{CB}(g)(\mu/\mu_0) \\ &= JA_B \frac{w}{4\pi}\frac{\mu}{\mu_0+\mu}\left[p(g)B_{SH}(g)+M(\mu_0,\mu)\right]B_{CB}(g) \end{aligned} \tag{16}$$

The reflectance relative to the standard is:

$$\begin{aligned} R = \frac{I_{\text{sample}}(i,e,g,w)}{I_{\text{standard}}(i_s,e_s,w_s)} &= \frac{JA_B \frac{w}{4\pi}\frac{\mu}{\mu_0+\mu}\left[p(g)B_{SH}(g)+M(\mu_0,\mu)\right]B_{CB}(g)}{JA_B \frac{w_s}{4\pi}\frac{\mu_s}{\mu_{0s}+\mu_s}\left[H(w_s,\mu_0)H(w_s,\mu_s)\right]} \\ &= \frac{w\frac{\mu}{\mu_0+\mu}\left[p(g)B_{SH}(g)+M(\mu_0,\mu)\right]B_{CB}(g)}{w_s\frac{\mu_s}{\mu_{0s}+\mu_s}\left[H(w_s,\mu_{0s})H(w_s,\mu_s)\right]} \end{aligned} \tag{17}$$

where the subscript 's' refers to values for the standard. Equation (17) is independent of the area of the laser beam and the incoming irradiance, and is easily modified to take into account different viewing geometries.

The single scattering albedo of the standard can be assumed to be 1, or it can be calculated from the hemispherical albedo given for the standard. The hemispherical albedo, denoted by r_h (or more precisely, the directional-hemispherical albedo), is calculated by determining the reflectance of a surface illuminated with a collimated beam and measured over a full hemisphere. The manual for the Labsphere Spectralon standard (available online at http://www.labsphere.com) provides a plot of directional-hemispherical reflectance versus wavelength for an incidence angle of 8° for this material. From these values, the single scattering albedo of the standard can be determined using the equation (Hapke, 2002, eq. 41a):

$$r_h = 1 - \sqrt{1-w}\,H(\mu_o) \tag{18}$$

where H, μ_o, and w have the same definitions as earlier (Equations (9) and (10)). The value of w that satisfies the equation must be determined iteratively, as the dependence on w is not simple. The manual for the standard gives a value of $r_h = 0.992$ at a wavelength of 0.635 μm, which translates to a single-scattering albedo of 0.99999214 using Equation (18). This value is very close to 1, but because the H is extremely sensitive to w when w is close to 1, this difference translates to a small, but significant, difference in the values of H used to calculate the correction factor for the standard, as opposed to assuming an albedo of 1. This calculated albedo has been used in all curve fitting presented herein.

Finally, the contributions from the opposition effect are added. The shadow-hiding opposition surge is dominated by singly scattered light, so it is applied only to the single scattering term. This is represented by the function (Hapke, 2002, eq. 29):

$$B_{SH}(g) = 1 + \frac{B_{S0}}{1 + (1/h_s)\tan(g/2)} \tag{19}$$

where B_{S0} is the amplitude of this opposition surge (never greater than 1), and h_s is the angular width in radians of the shadow-hiding opposition effect. The coherent backscatter surge is

treated in a similar fashion, but is applied to the entire scattering term, and takes the form (Hapke, 2002, eq. 32):

$$B_{CB}(g) = 1 + B_{C0}\left[\frac{1 + \frac{1 - e^{-((1/h_c)\tan(g/2))}}{(1/h_c)\tan(g/2)}}{2\left[1 + (1/h_c)\tan(g/2)\right]^2}\right] \tag{20}$$

where the terms B_{C0} and h_c are similarly the amplitude and angular width (again in radians) of the coherent backscatter opposition surge.

The improved model of Hapke (2002) was used to determine the scattering parameters from the phase curve data. The parameters of interest, in this case, were the single scattering albedo (w), the single scattering function (p(g)), the amplitude and width of the shadow-hiding opposition surge (B_{S0} and h_s), and the amplitude and width of the coherent backscatter opposition surge (B_{C0} and h_c). Considering that p(g) is not a simple function, this leaves a significant number of parameters to be fit, which presents both a difficulty in finding a unique fit and a significant increase in the amount of computing time required to complete the fitting algorithm. In order to alleviate these problems, the fits were broken down into two stages. First, the single scattering albedo and single scattering function were determined by fitting the largest phase angles (> 20°) of the short arm goniometer data, where the effect of the opposition surge should be negligible. These solutions were then used to fit the shorter angles of the short arm data, by holding these parameters constant and fitting both the opposition effect functions. Finally, once the best solution was achieved via this method, all variables were allowed to vary, and the curve fit was finalized. These final fits are shown in Figures 11-17, with the appropriate scattering parameters listed in the lower right hand corner of each plot.

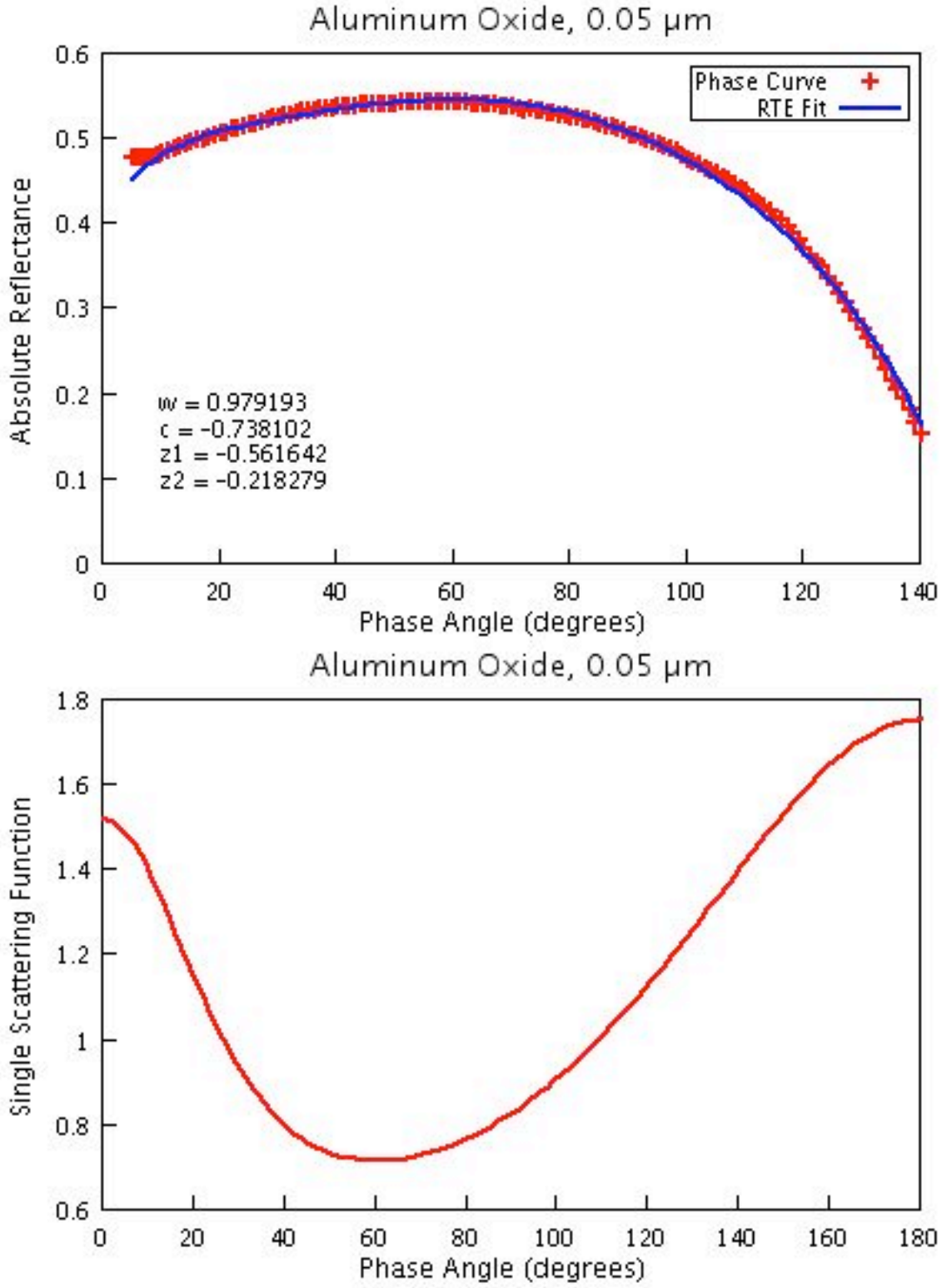

Figure 11a: Aluminum oxide short arm phase curves and model fits, and single scattering functions, expressed as asymmetric double Henyey-Greenstein functions. Figures are labeled by manufacturer's nominal particle diameter, with model parameters given in the lower left hand corner. This figure shows the phase curve for the 0.05 μm sample.

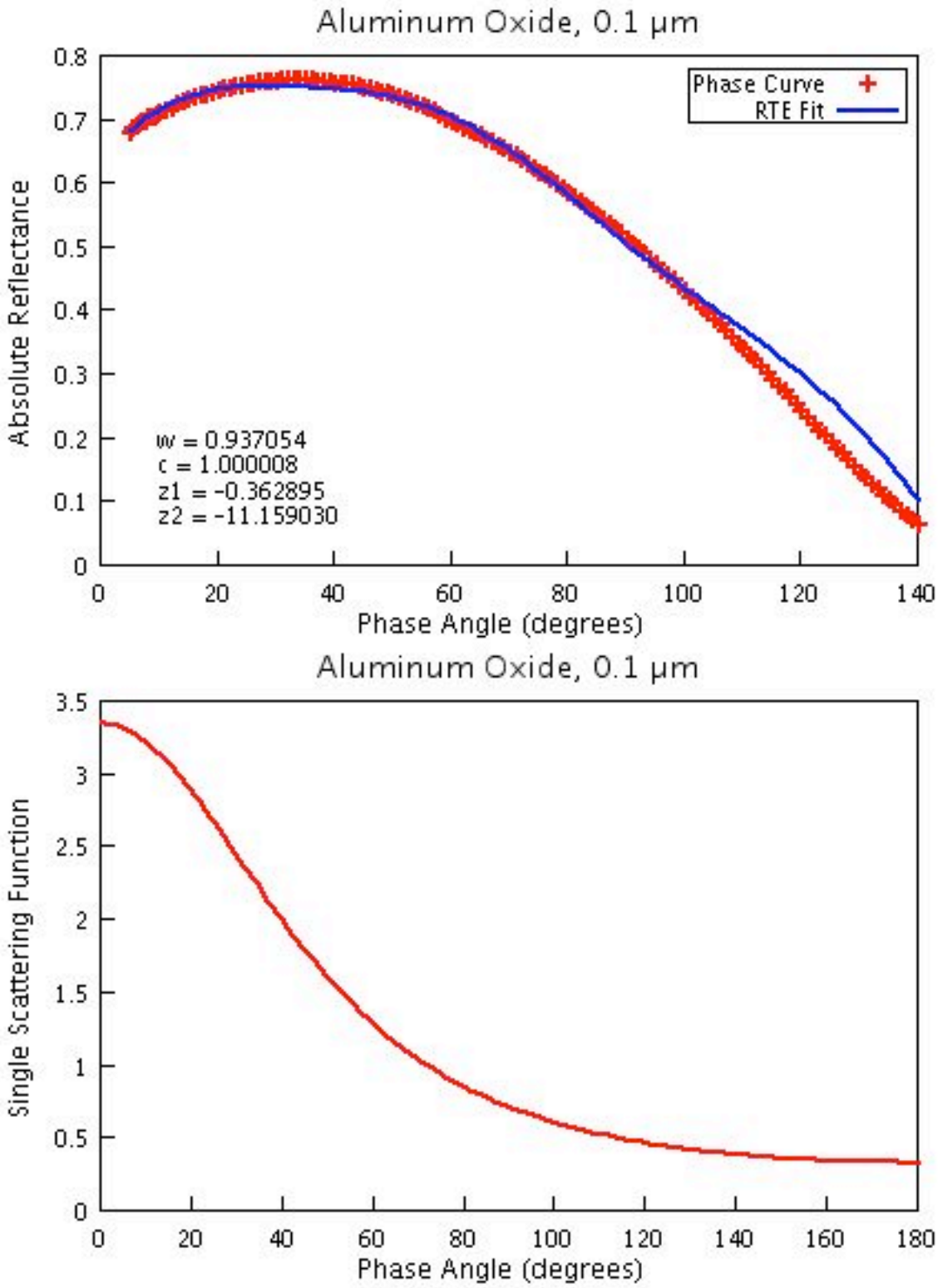

Figure 11b: Short arm phase curve and single scattering function for 0.1 μm aluminum oxide.

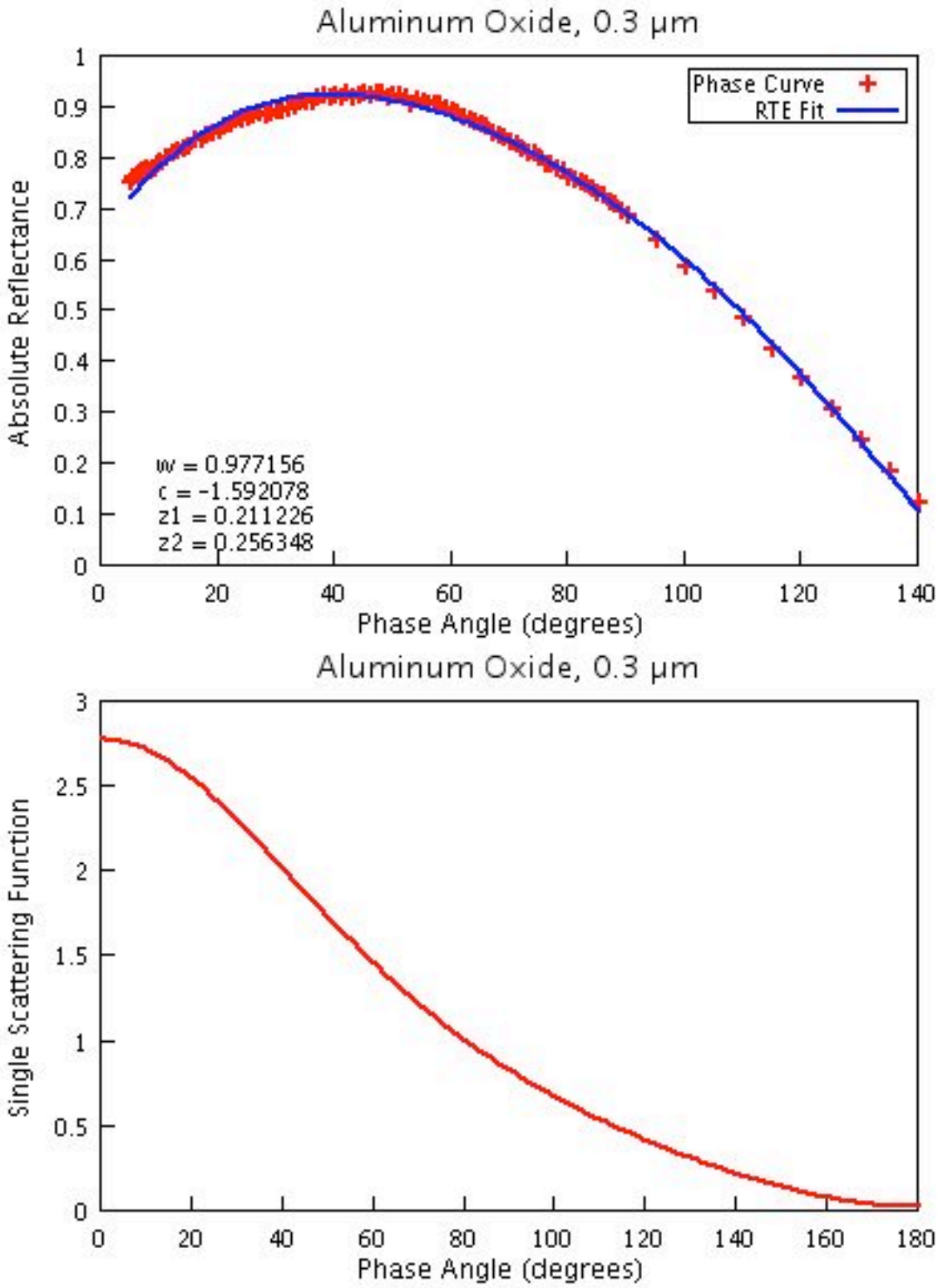

Figure 11c: Short arm phase curve and single scattering function for 0.3 μm aluminum oxide.

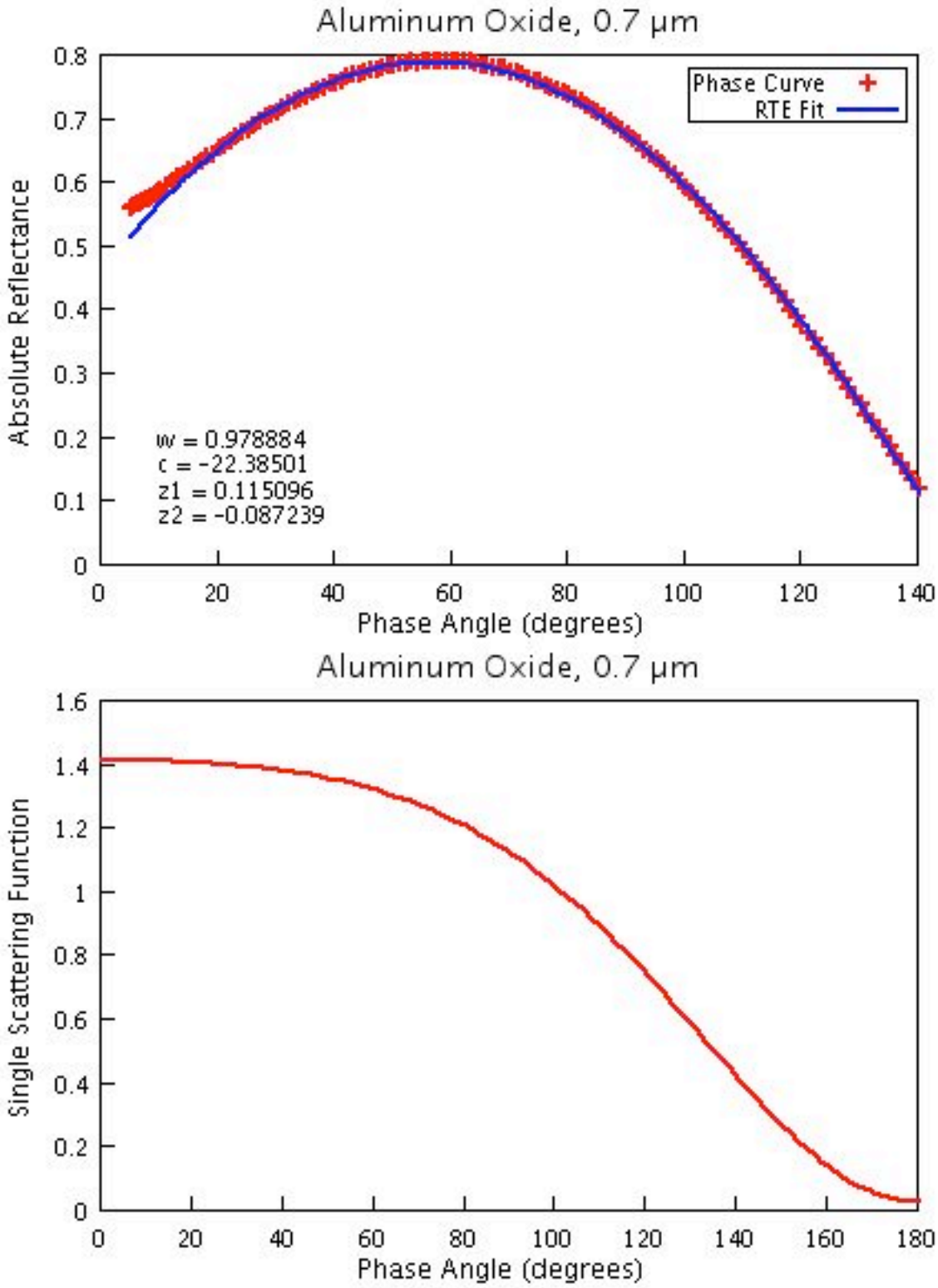

Figure 11d: Short arm phase curve and single scattering function for 0.7 μm aluminum oxide.

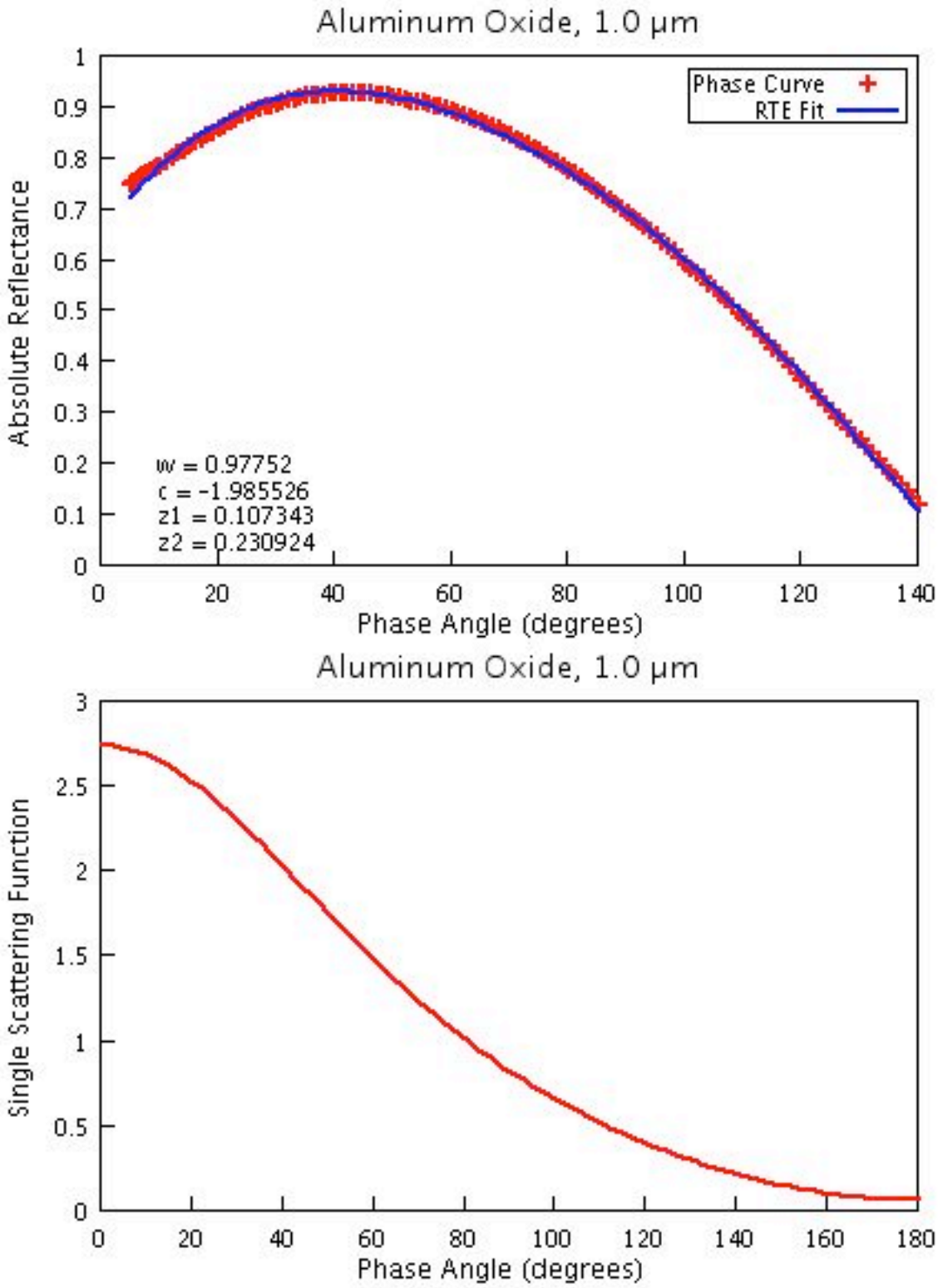

Figure 11e: Short arm phase curve and single scattering function for 1.0 μm aluminum oxide.

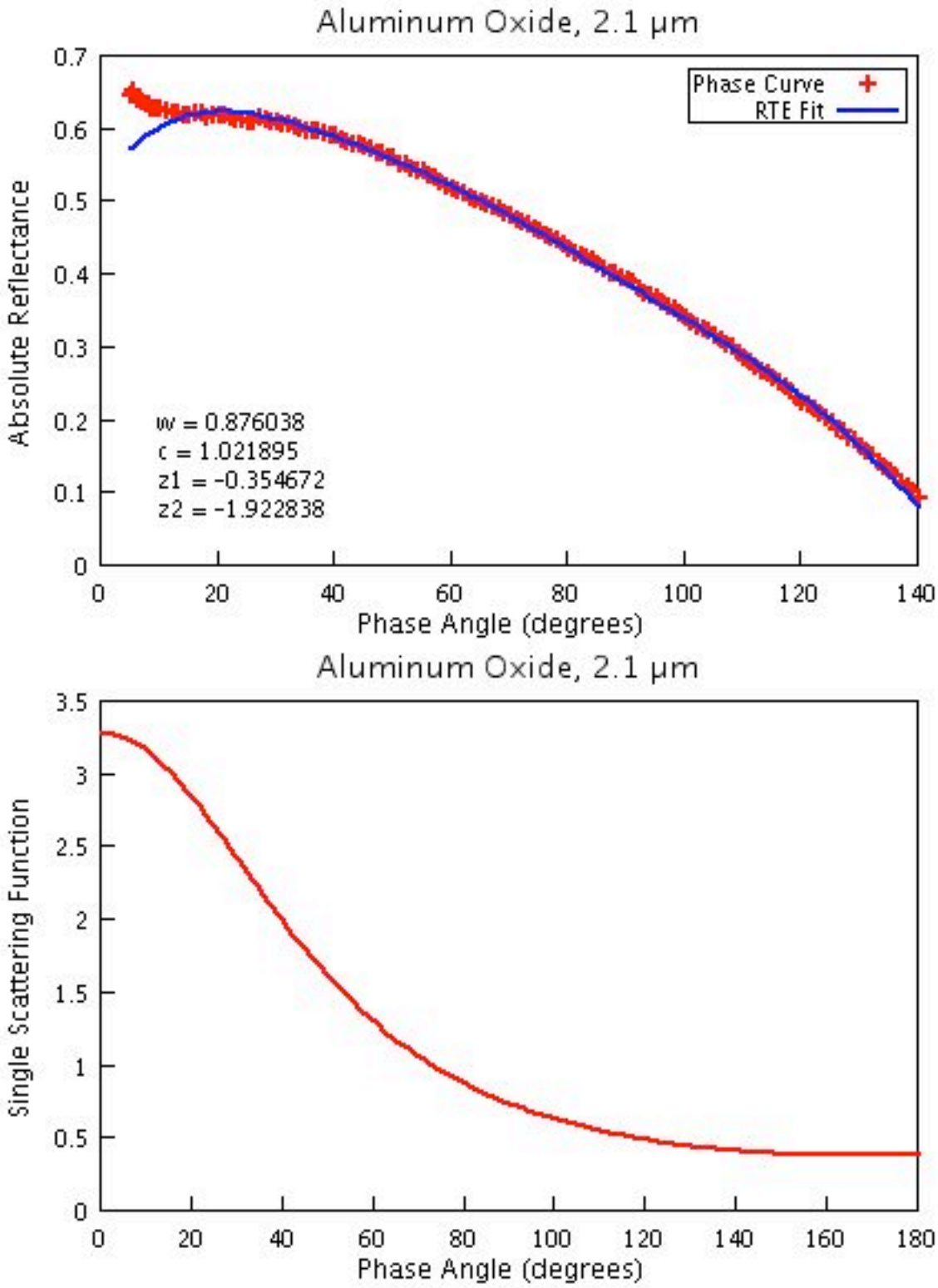

Figure 11f: Short arm phase curve and single scattering function for 2.1 μm aluminum oxide.

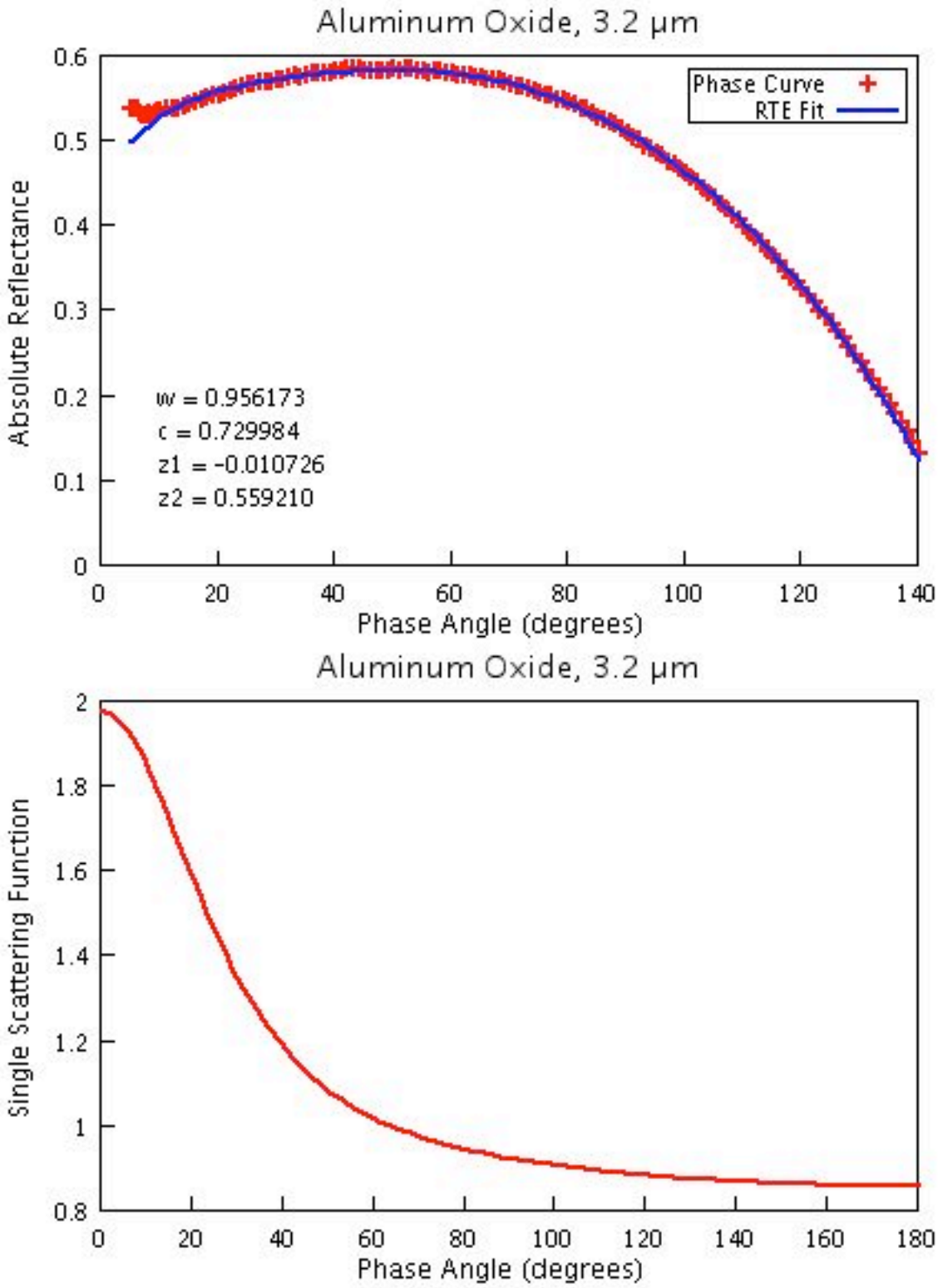

Figure 11g: Short arm phase curve and single scattering function for 3.2 μm aluminum oxide.

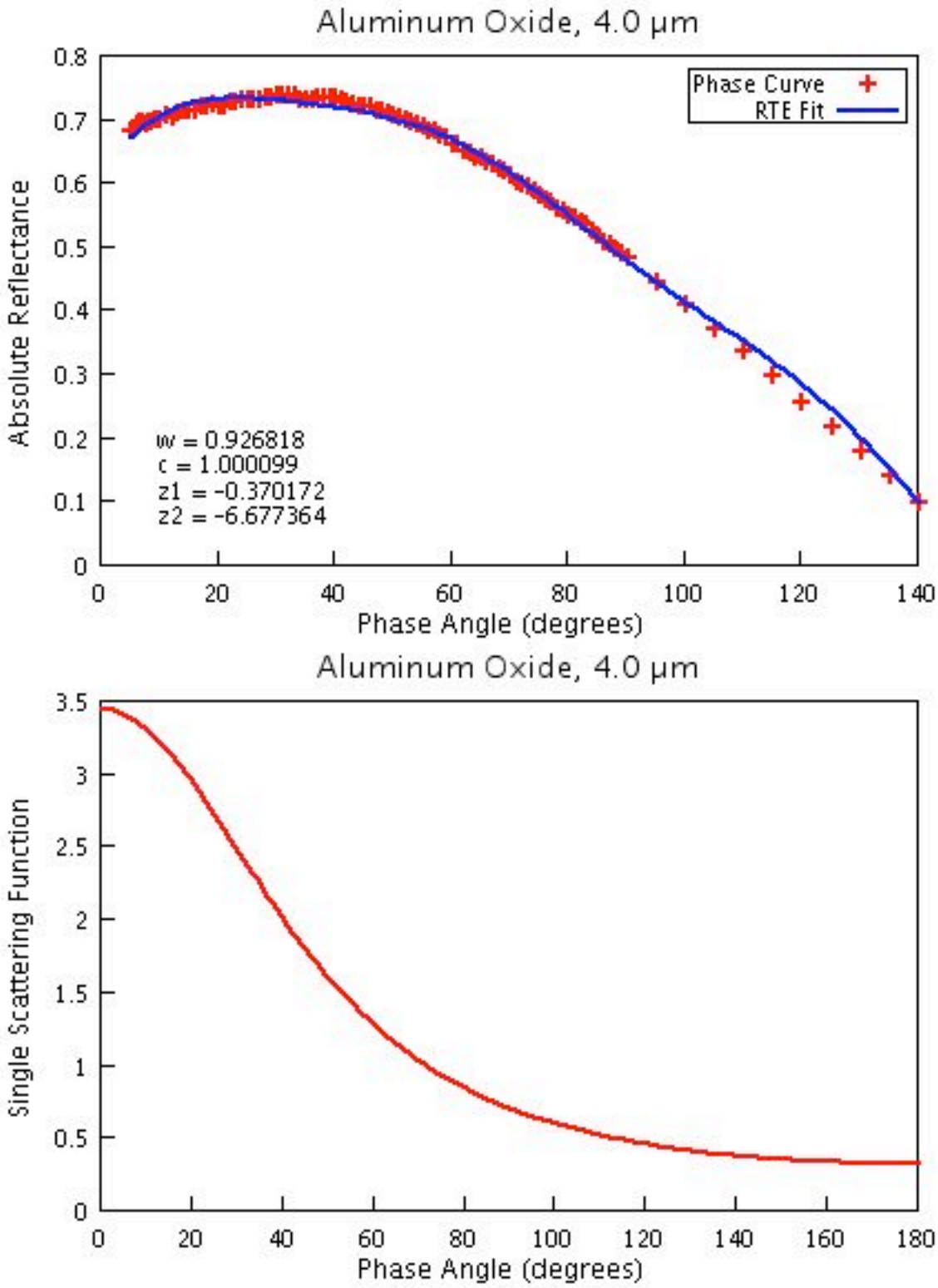

Figure 11h: Short arm phase curve and single scattering function for 4.0 μm aluminum oxide.

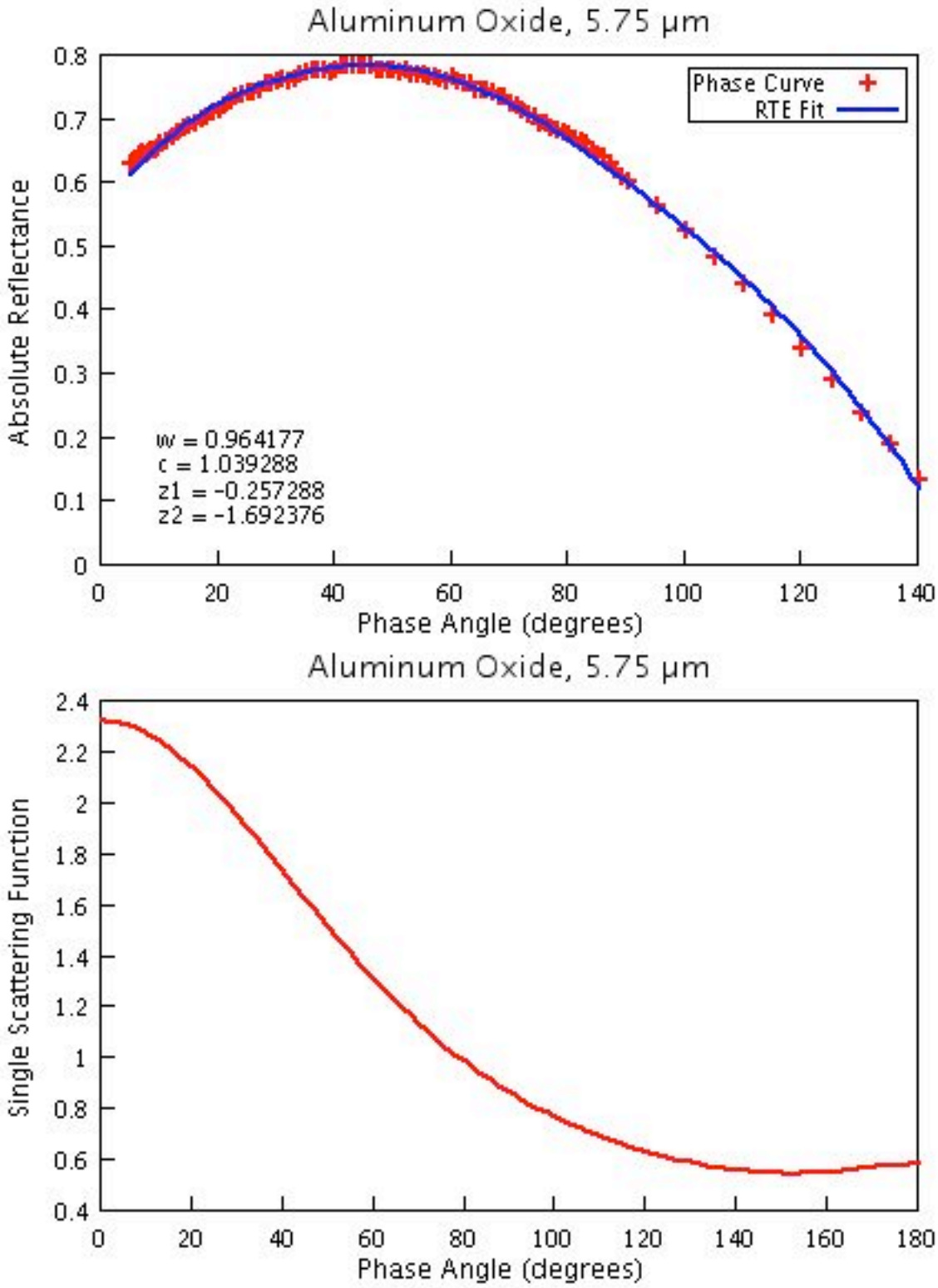

Figure 11i: Short arm phase curve and single scattering function for 5.75 μm aluminum oxide.

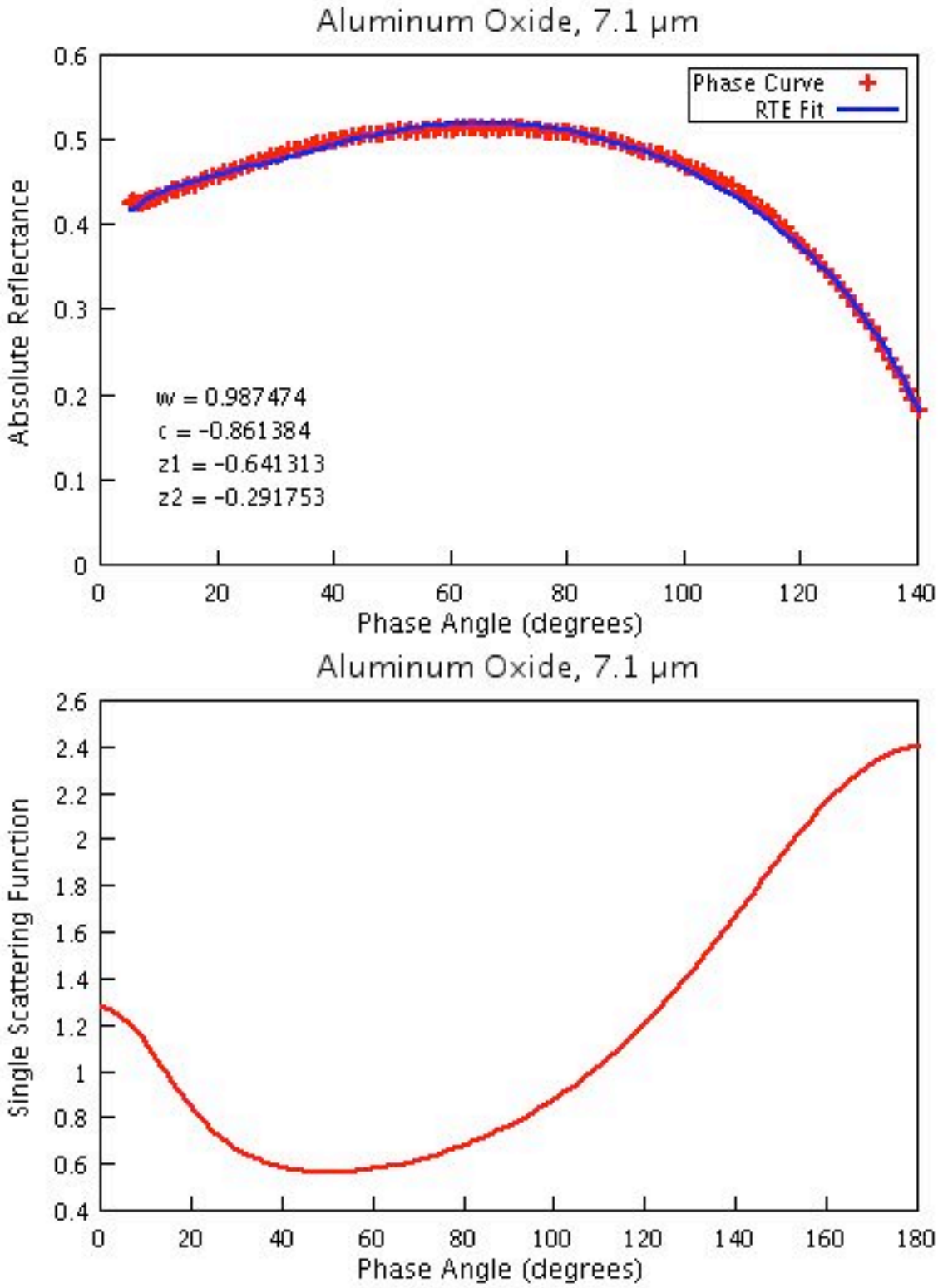

Figure 11j: Short arm phase curve and single scattering function for 7.1 μm aluminum oxide.

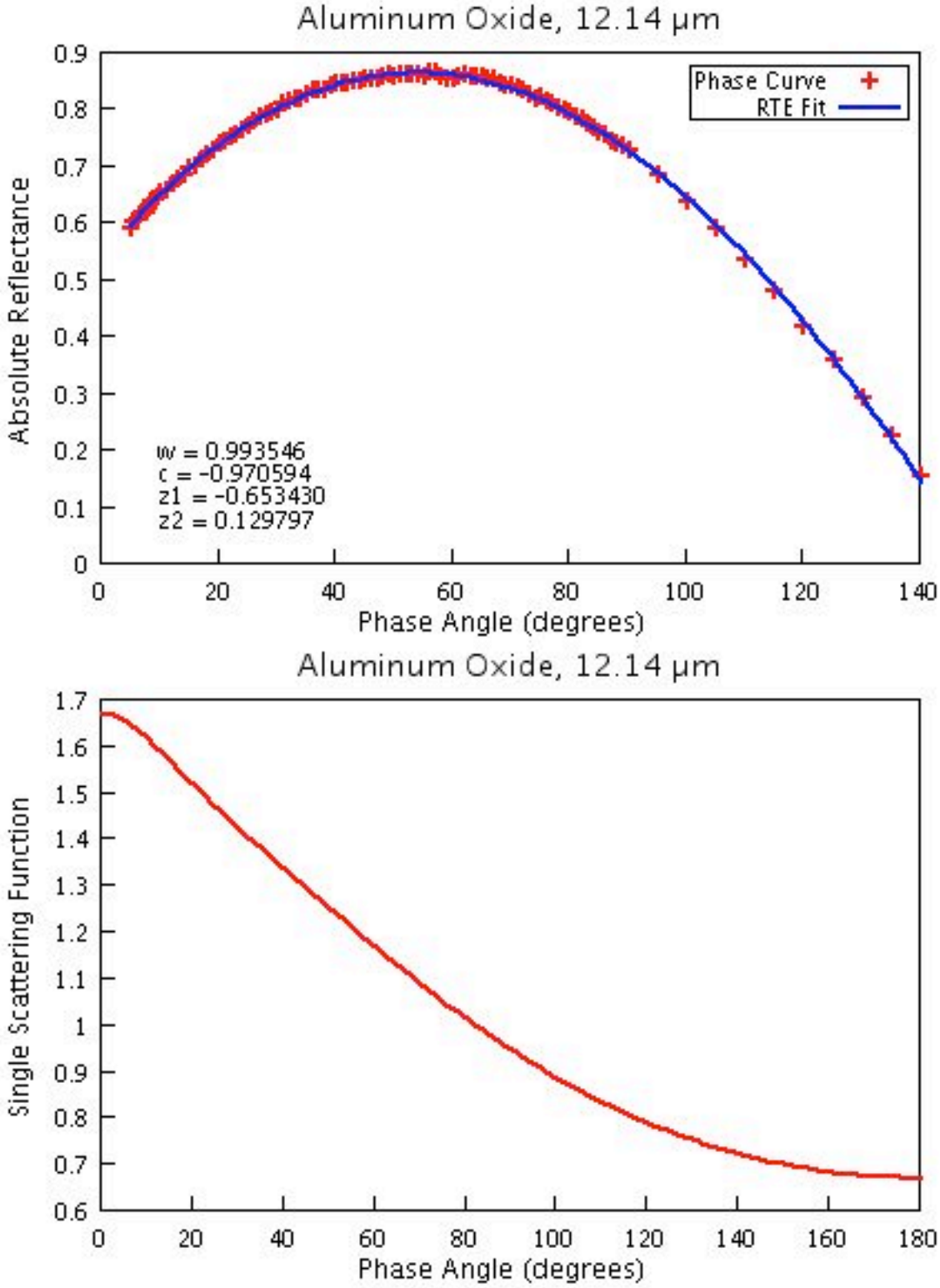

Figure 11k: Short arm phase curve and single scattering function for 12.14 μm aluminum oxide.

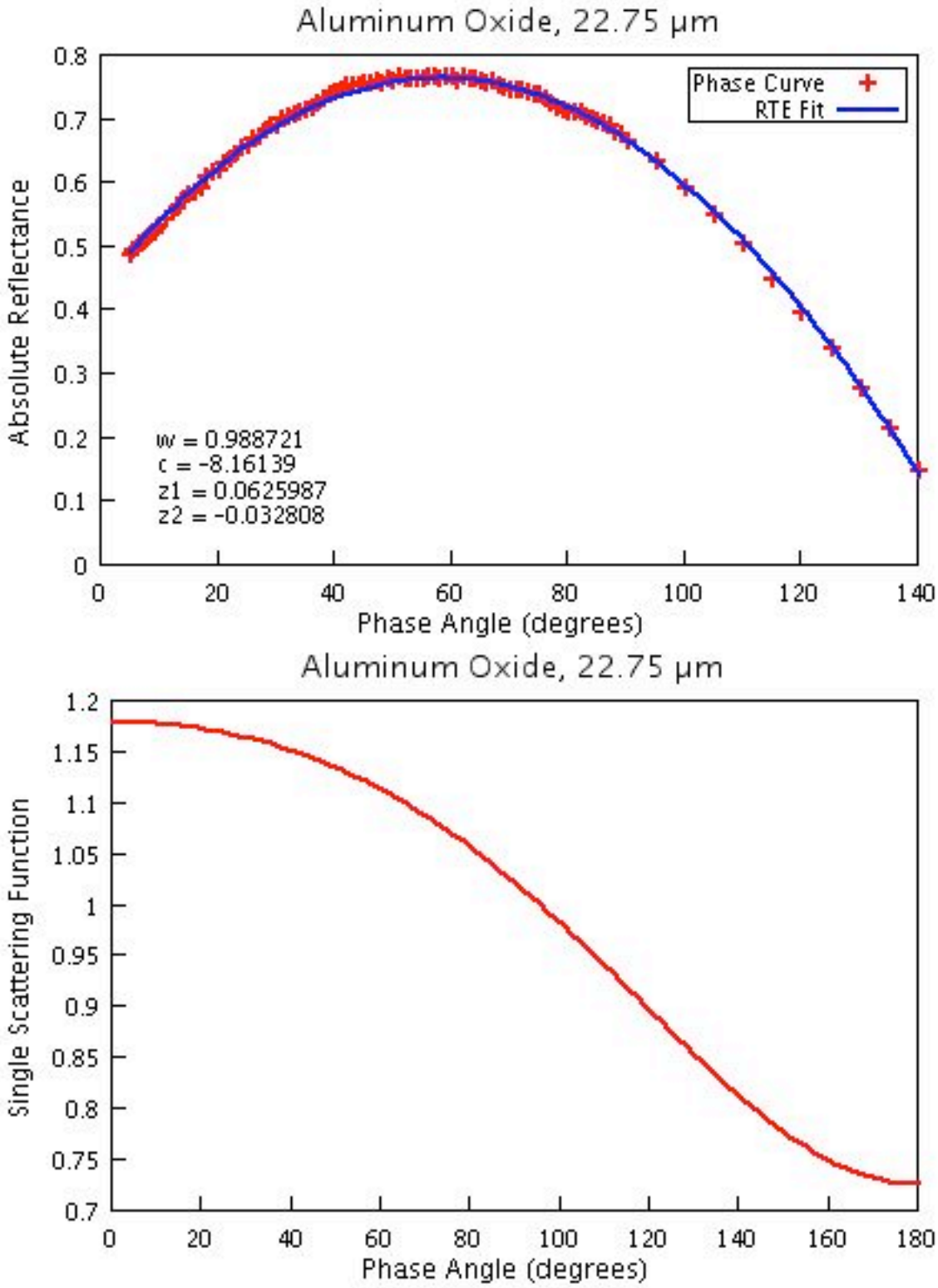

Figure 11l: Short arm phase curve and single scattering function for 22.75 μm aluminum oxide.

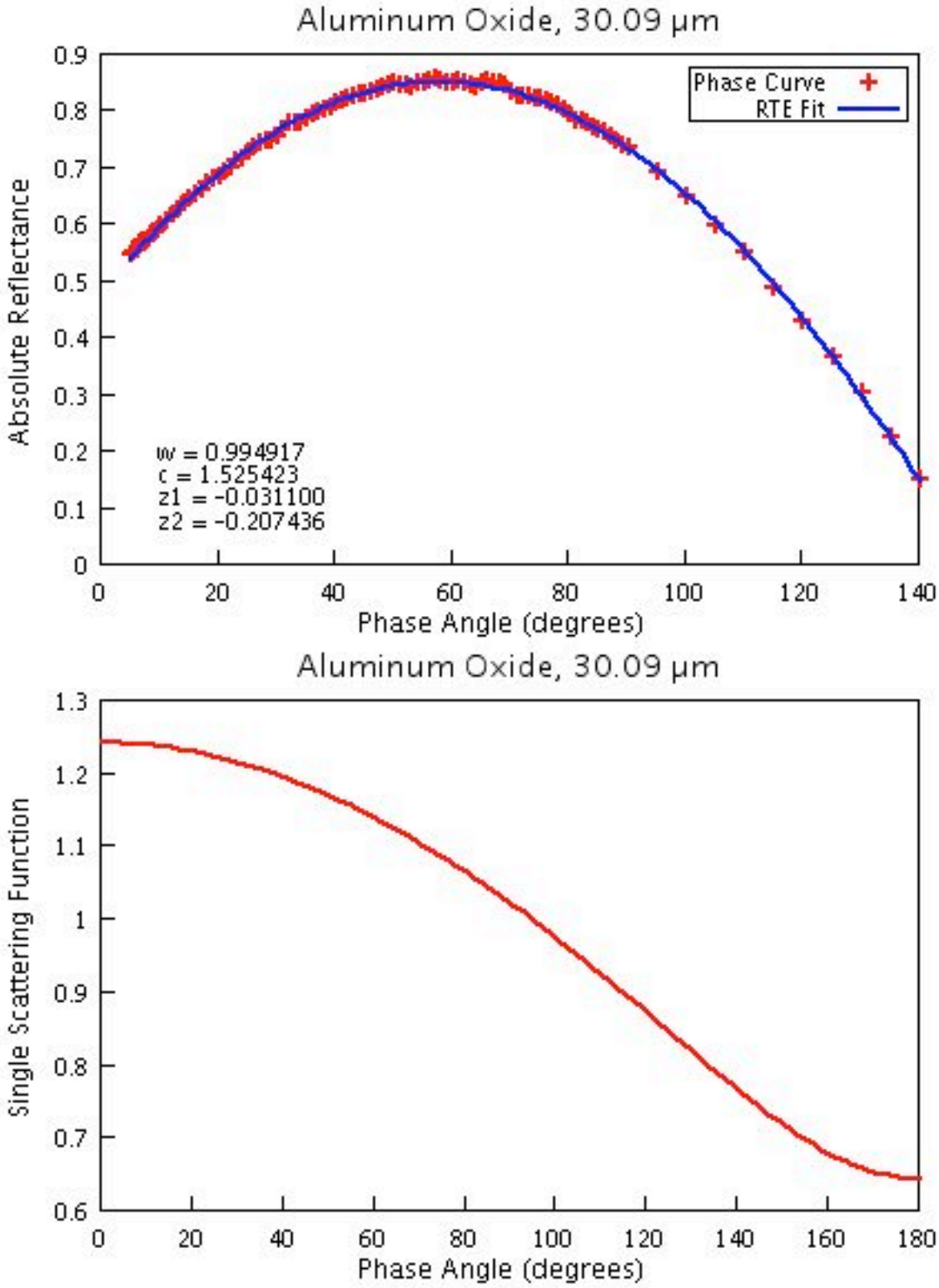

Figure 11m: Short arm phase curve and single scattering function for 30.09 μm aluminum oxide.

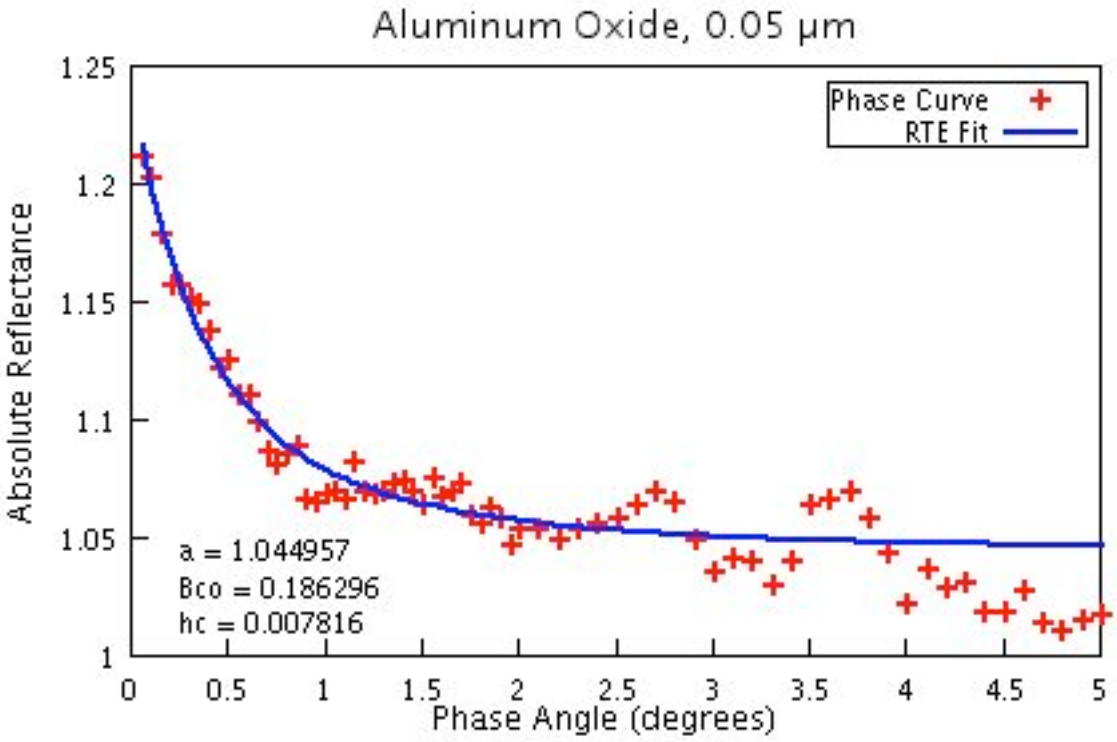

Figure 12a: Aluminum oxide long arm phase curves and model fits, using the model $R = A \cdot B_{CB}$. Model parameters are listed on each graph, which are labeled by nominal particle size. Shown above is the phase curve for the 0.05 μm aluminum oxide sample.

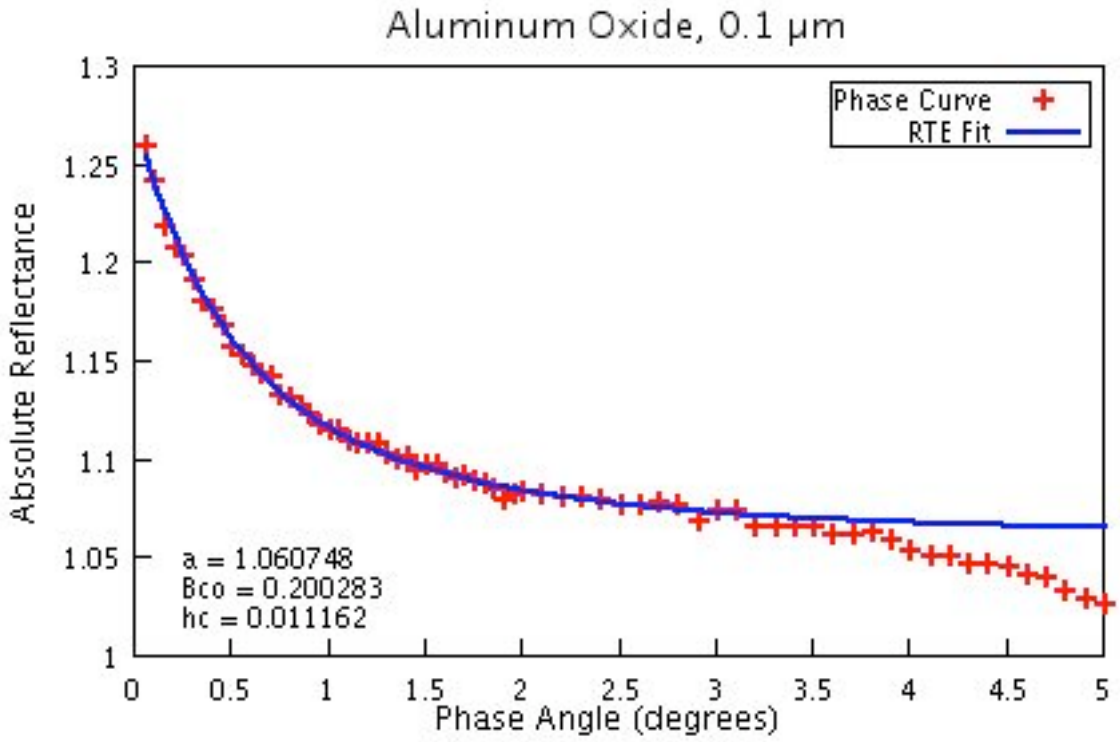

Figure 12b: Long arm phase curve for 0.1 μm aluminum oxide.

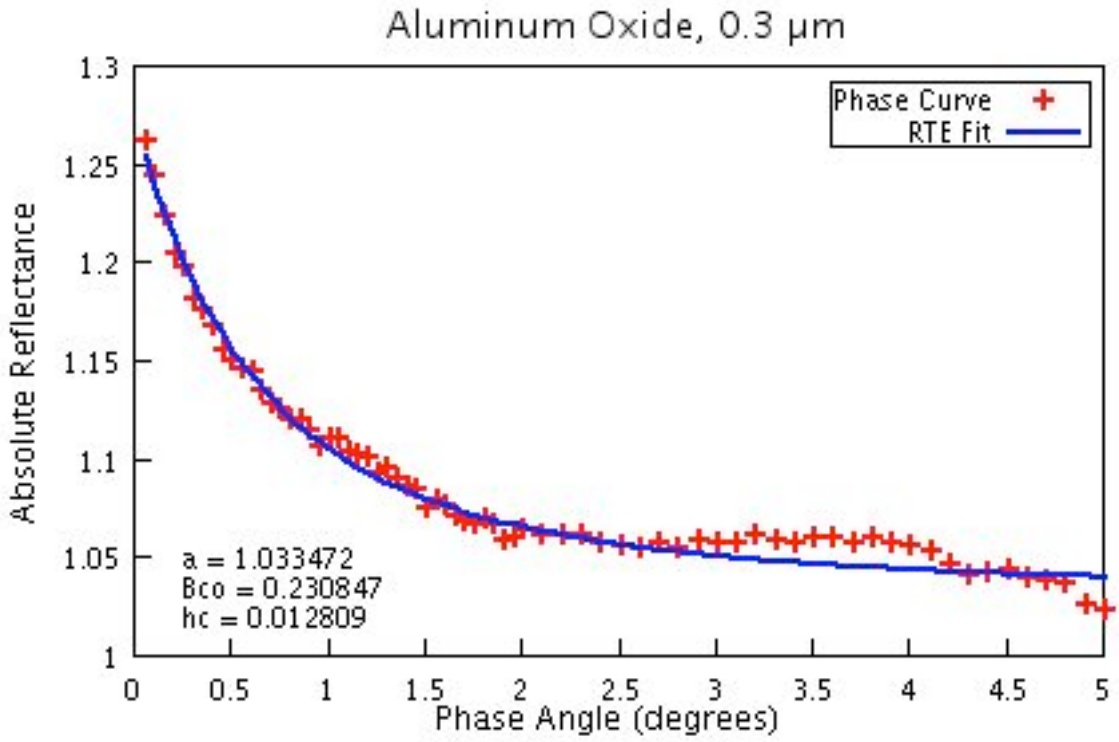

Figure 12c: Long arm phase curve for 0.3 μm aluminum oxide.

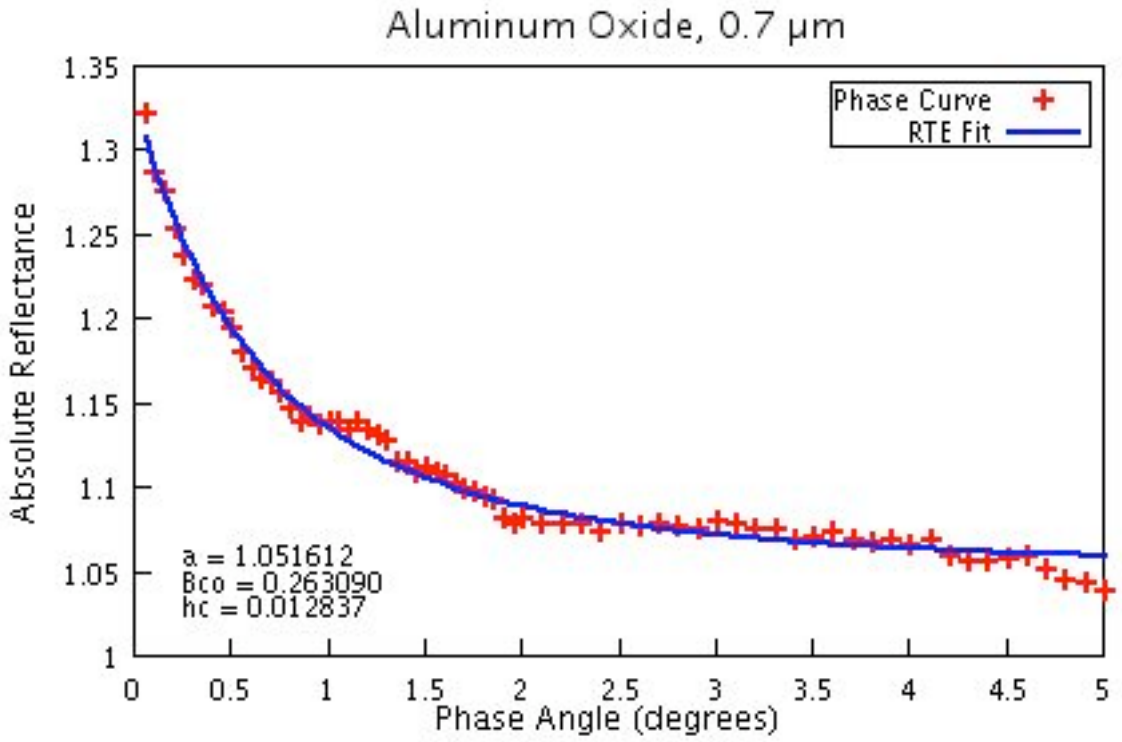

Figure 12d: Long arm phase curve for 0.7 μm aluminum oxide.

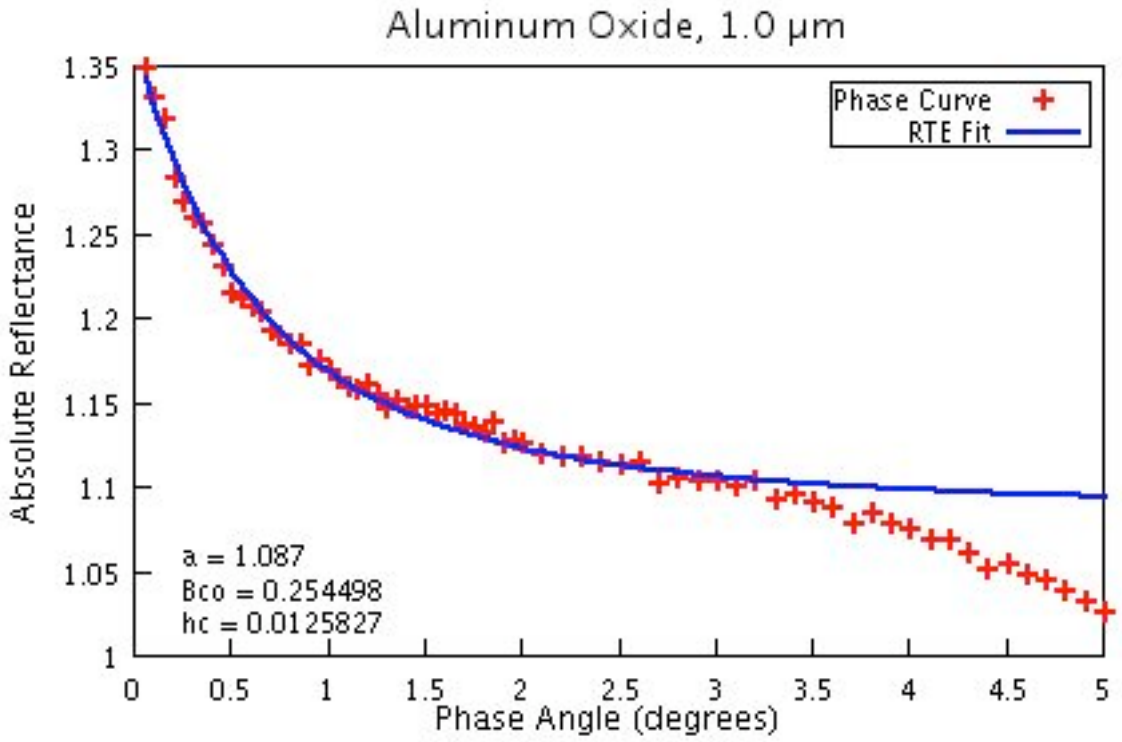

Figure 12e: Long arm phase curve for 1.0 μm aluminum oxide.

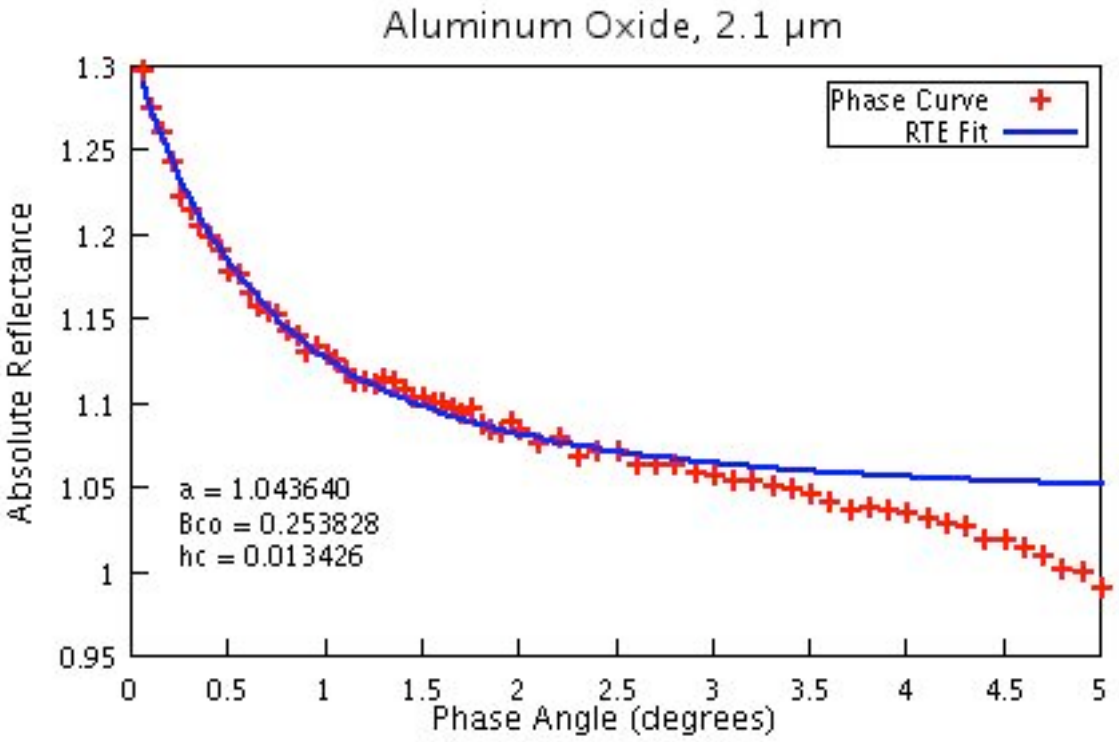

Figure 12f: Long arm phase curve for 2.1 μm aluminum oxide.

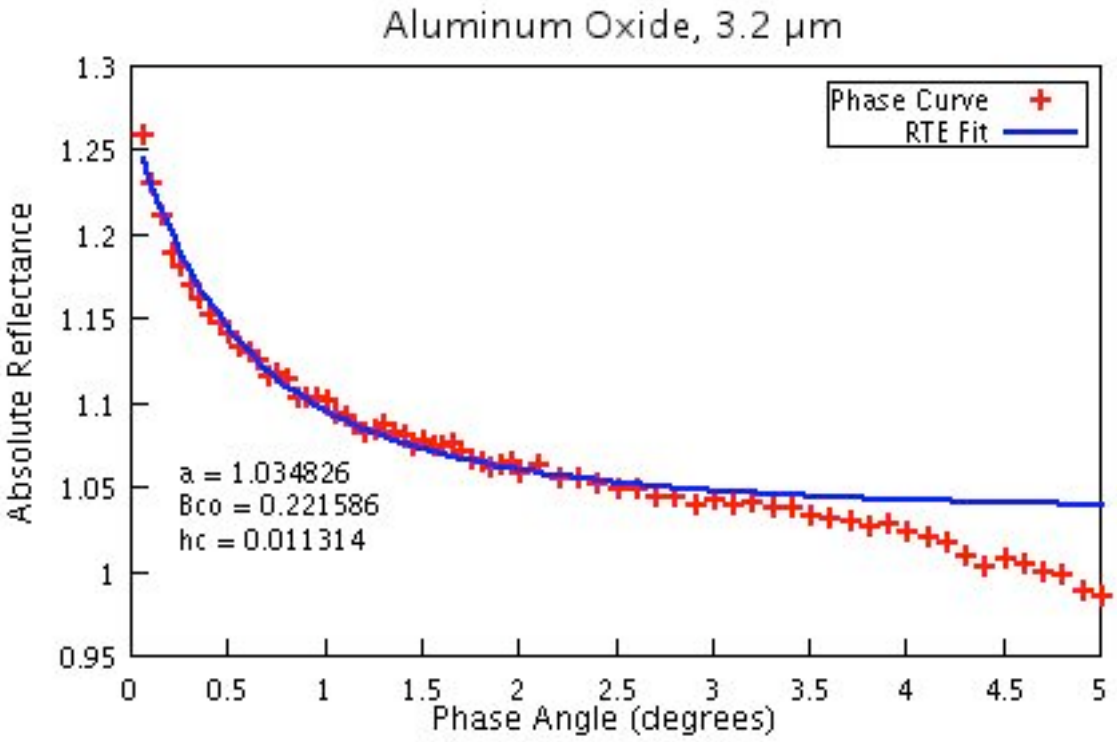

Figure 12g: Long arm phase curve for 3.2 μm aluminum oxide.

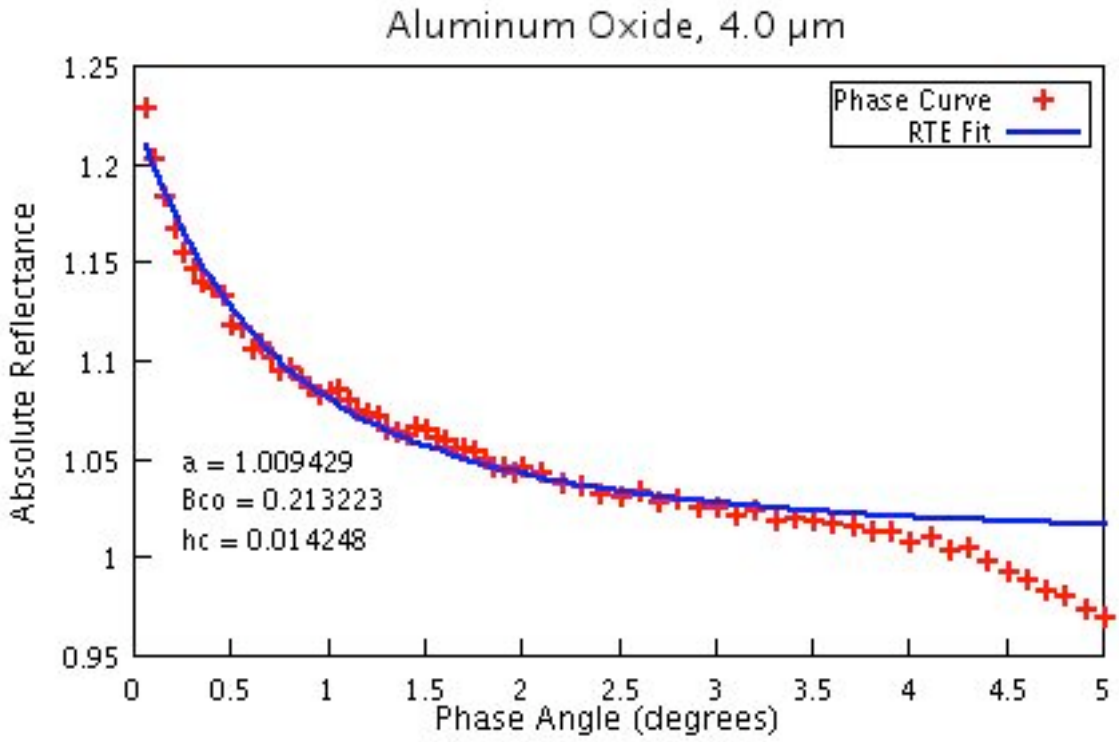

Figure 12h: Long arm phase curve for 4.0 μm aluminum oxide.

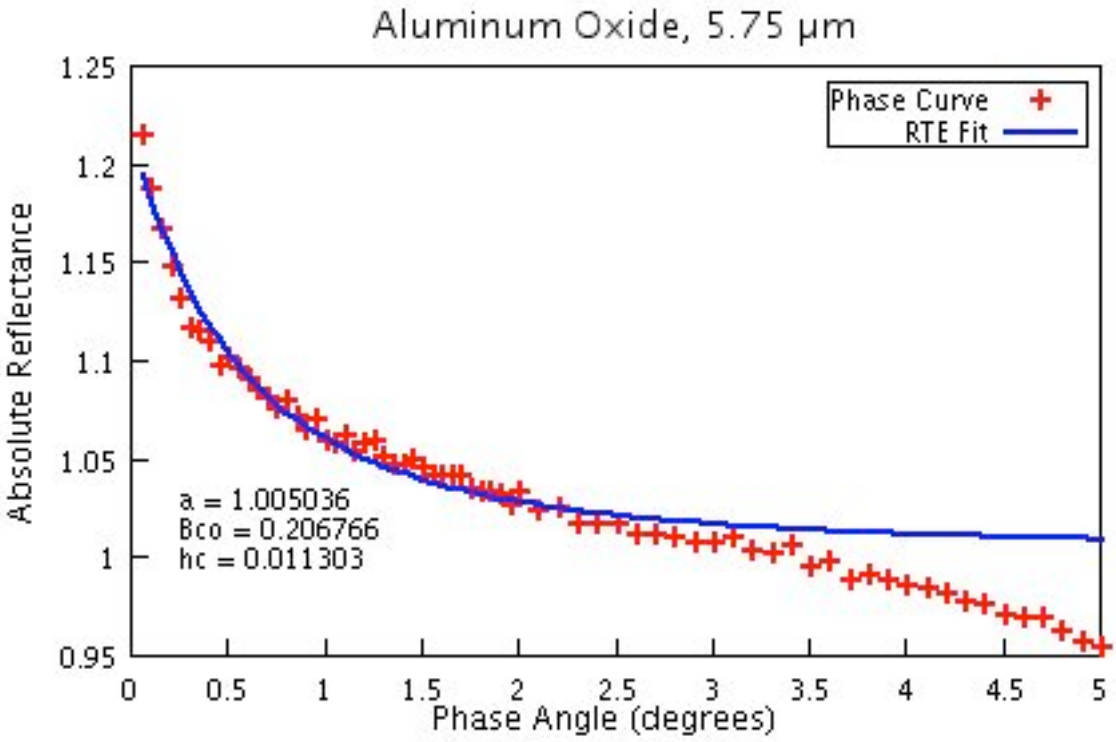

Figure 12i: Long arm phase curve for 5.75 μm aluminum oxide.

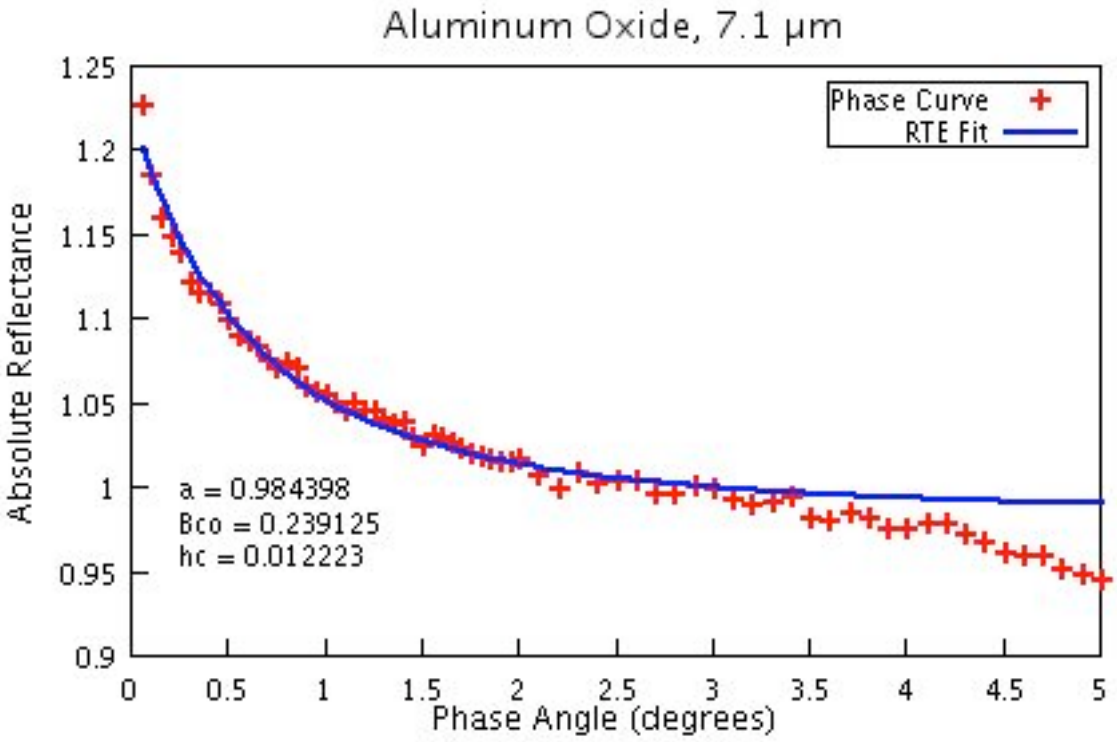

Figure 12j: Long arm phase curve for 7.1 μm aluminum oxide.

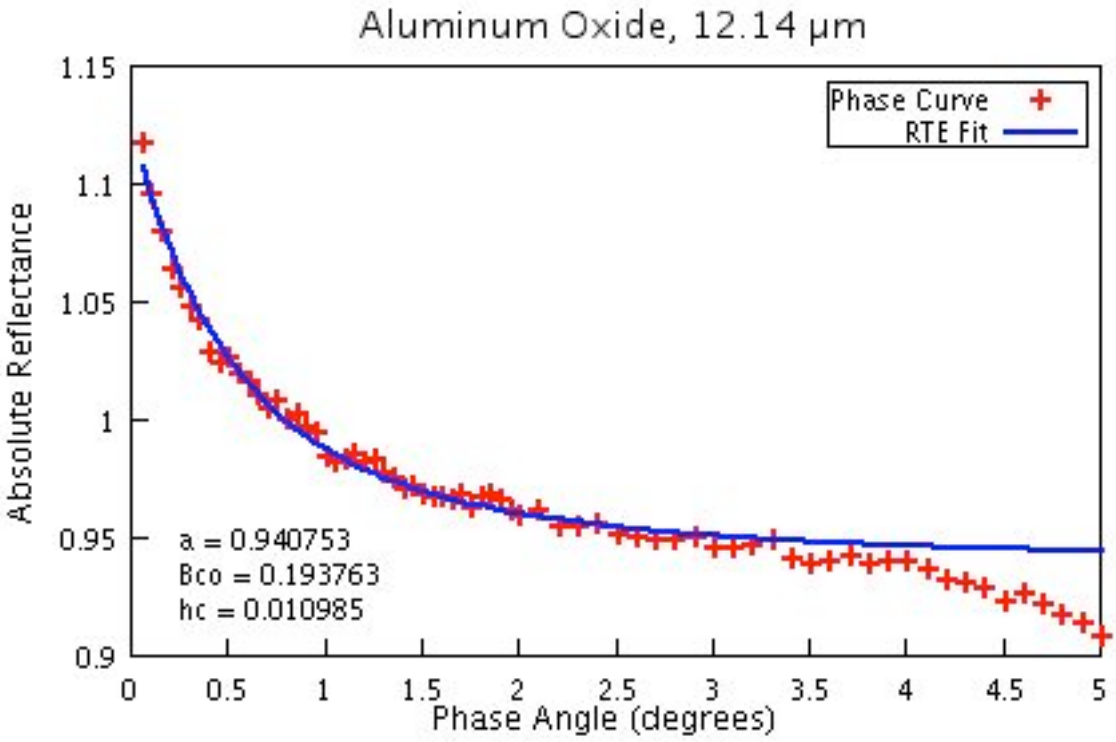

Figure 12k: Long arm phase curve for 12.14 μm aluminum oxide.

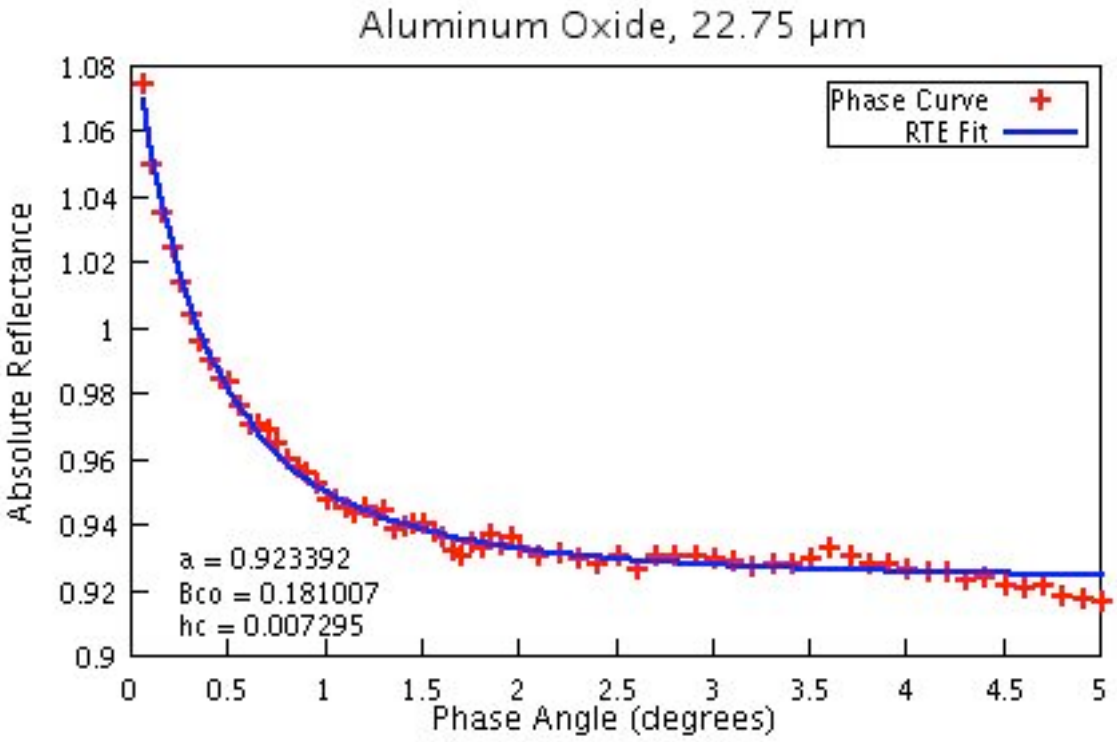

Figure 12l: Long arm phase curve for 22.75 μm aluminum oxide

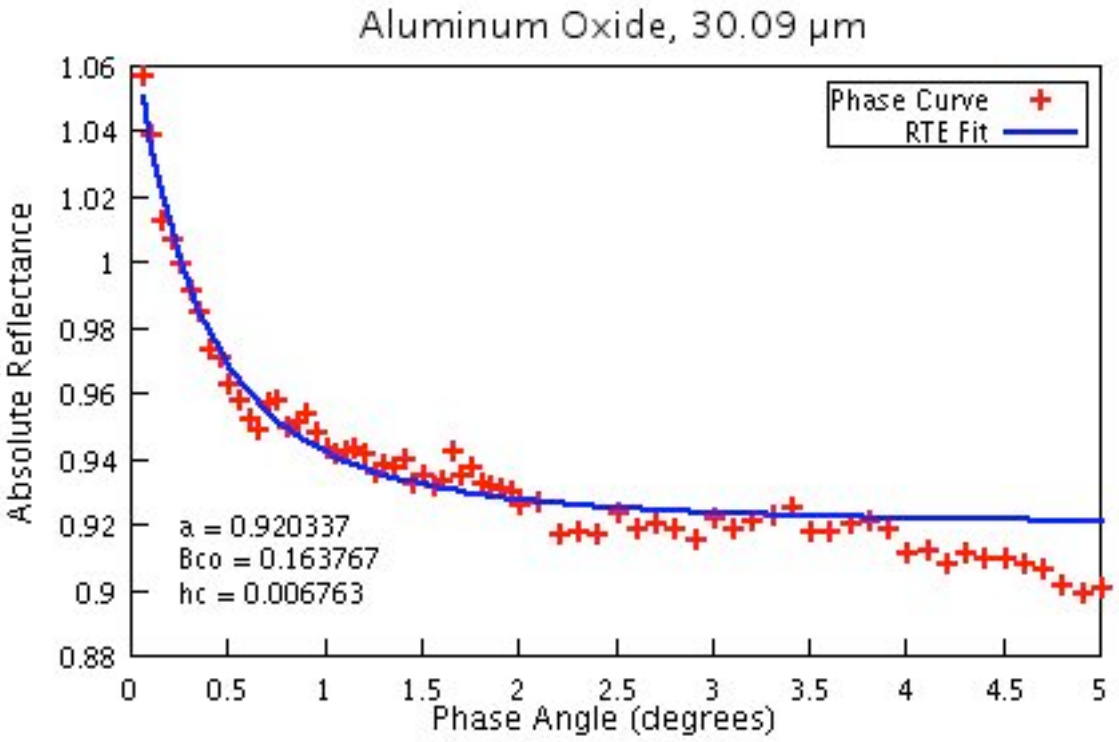

Figure 12m: Long arm phase curve for 30.09 μm aluminum oxide.

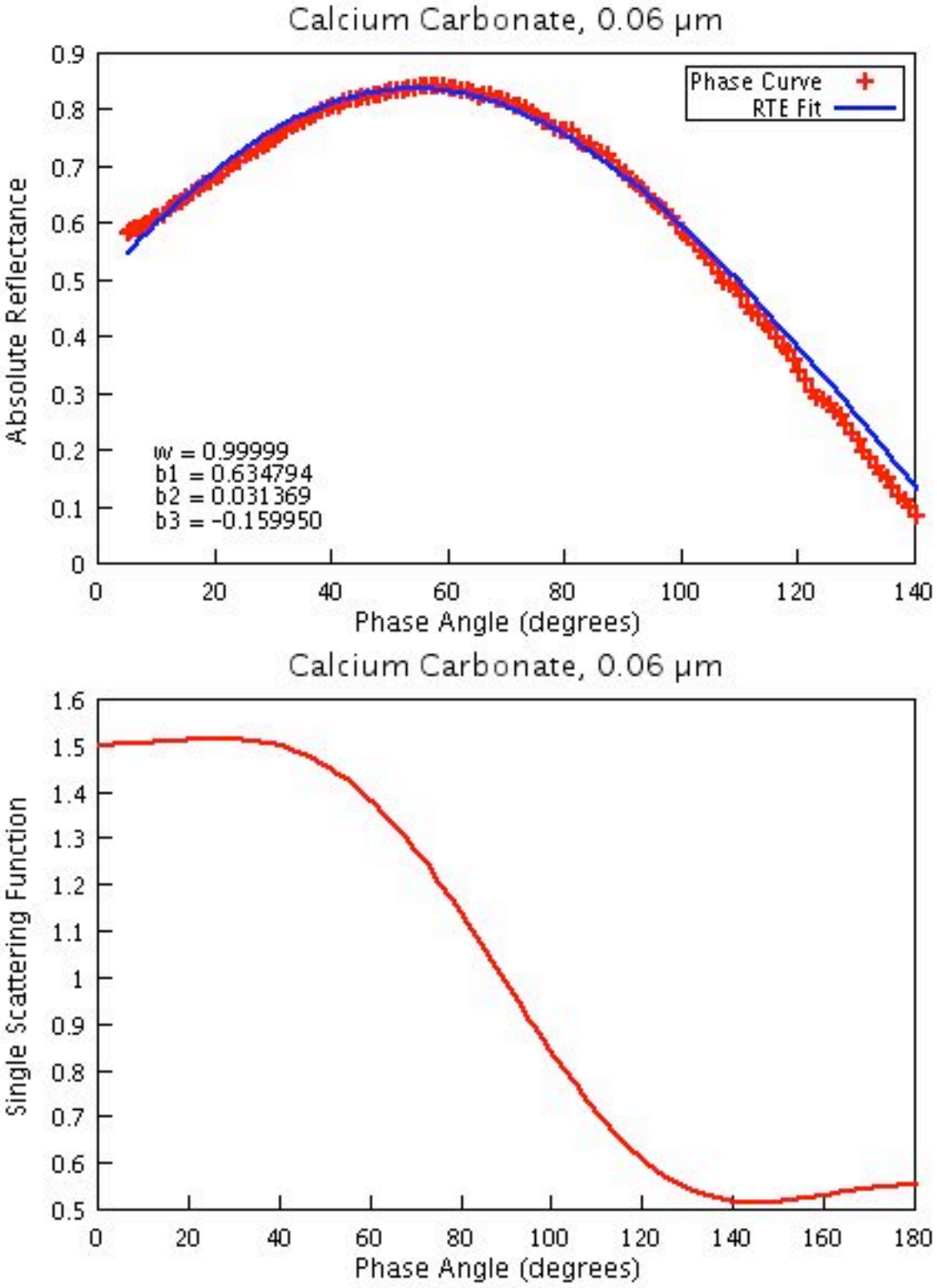

Figure 13a: Calcium carbonate short arm phase curves and model fits, and single scattering functions, expressed as 3rd order Legendre polynomial expansions. Figures are labeled by manufacturer's nominal particle diameter, with model parameters given in the lower left hand corner. Shown above is the phase curve and single scattering function for the 0.06 μm sample.

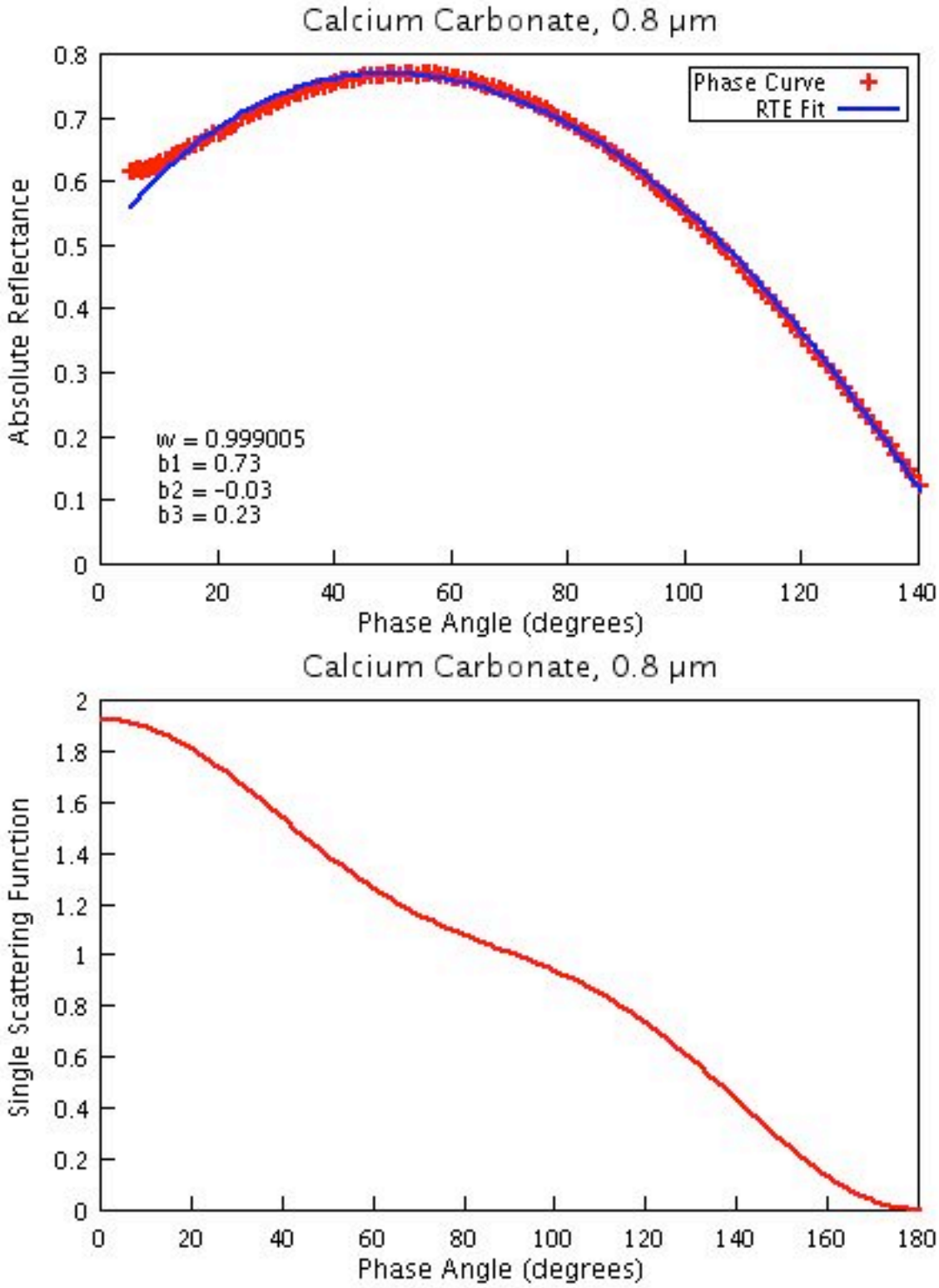

Figure 13b: Short arm phase curve and single scattering function for 0.8 μm calcium carbonate.

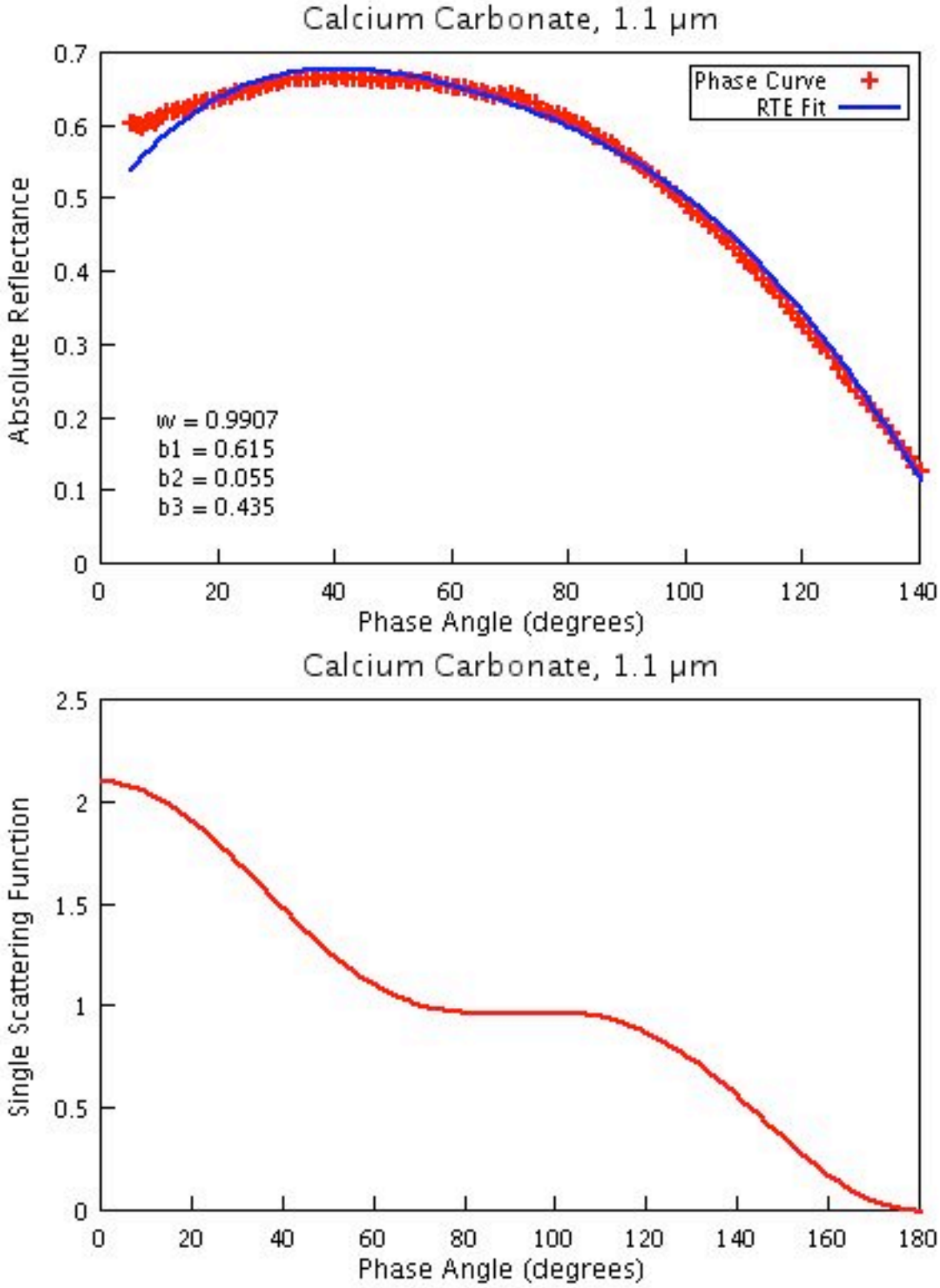

Figure 13c: Short arm phase curve and single scattering function for 1.1 μm calcium carbonate.

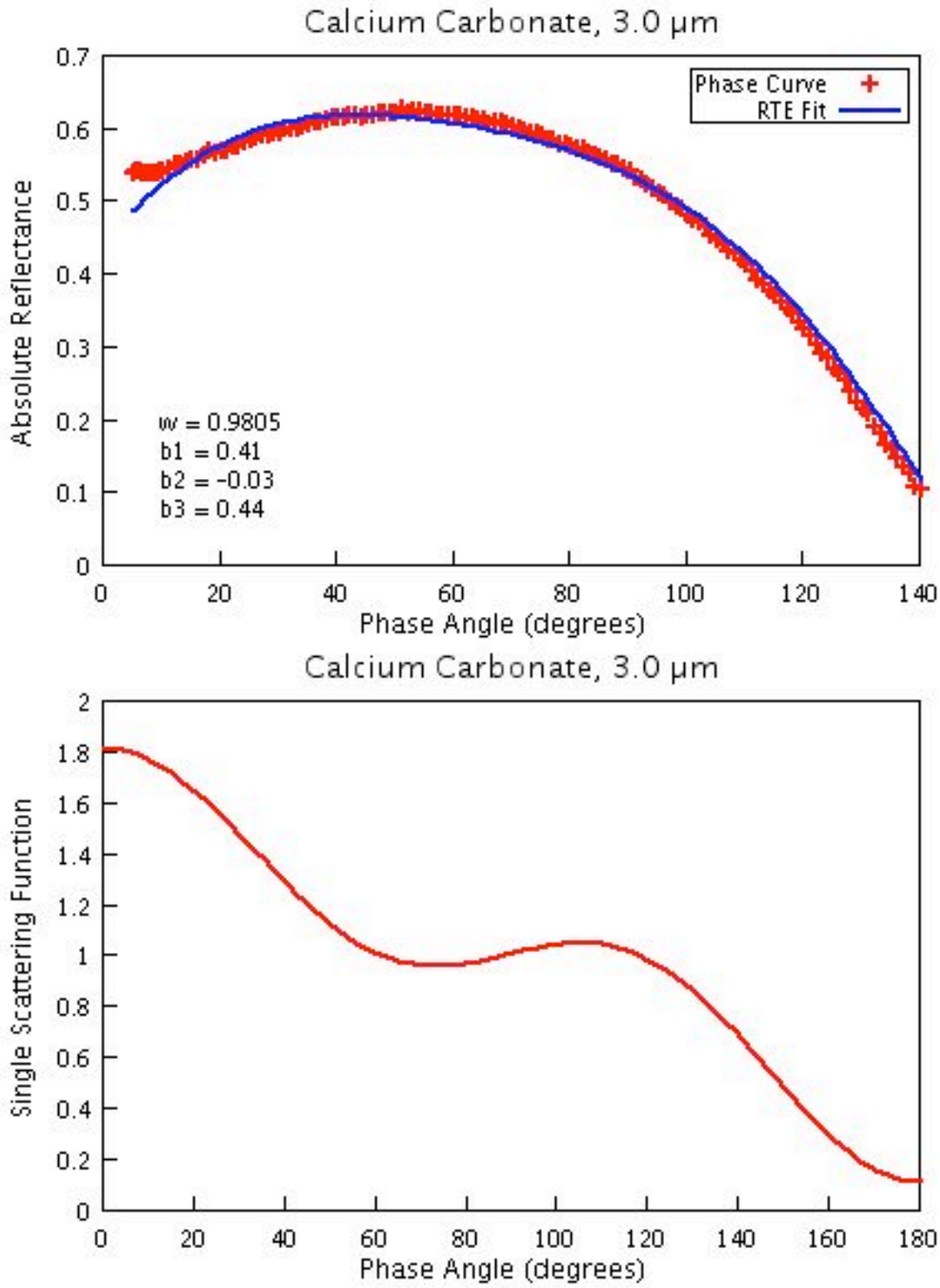

Figure 13d: Short arm phase curve and single scattering function for 3.0 μm calcium carbonate.

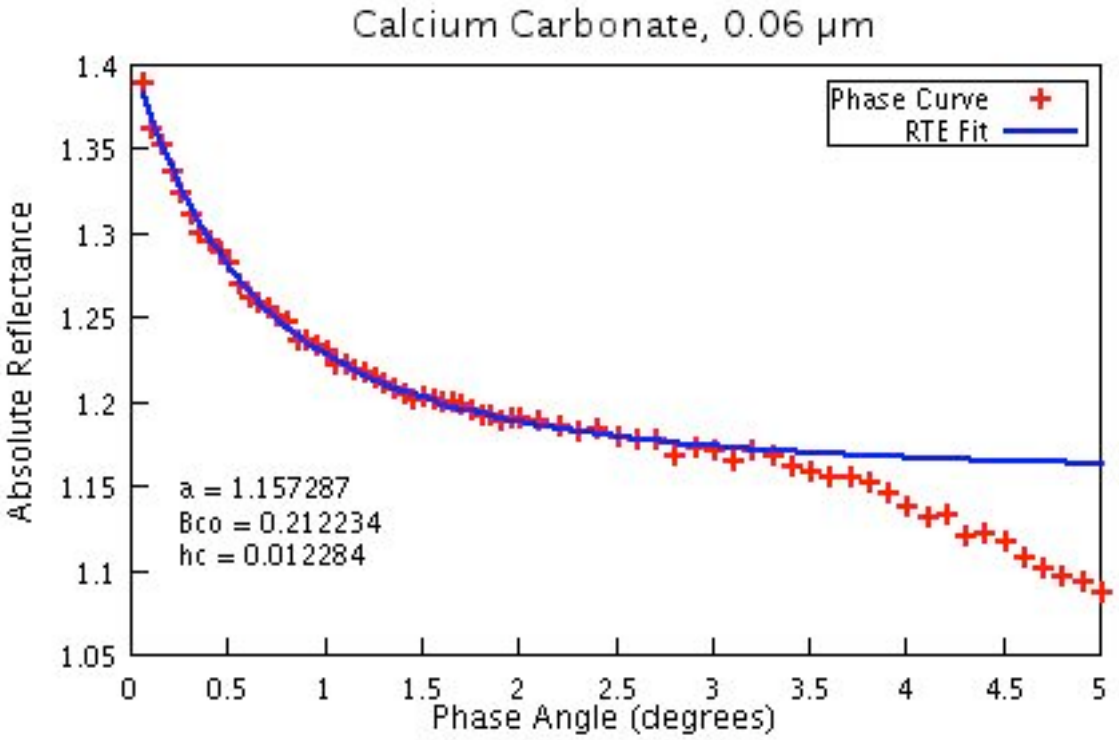

Figure 14a: Calcium carbonate long arm phase curves and model fits, using the simplified model $R = A \cdot B_{CB}$. Model parameters are listed on each graph, which are labeled by nominal particle size. Shown above is the phase curve for the 0.06 μm sample.

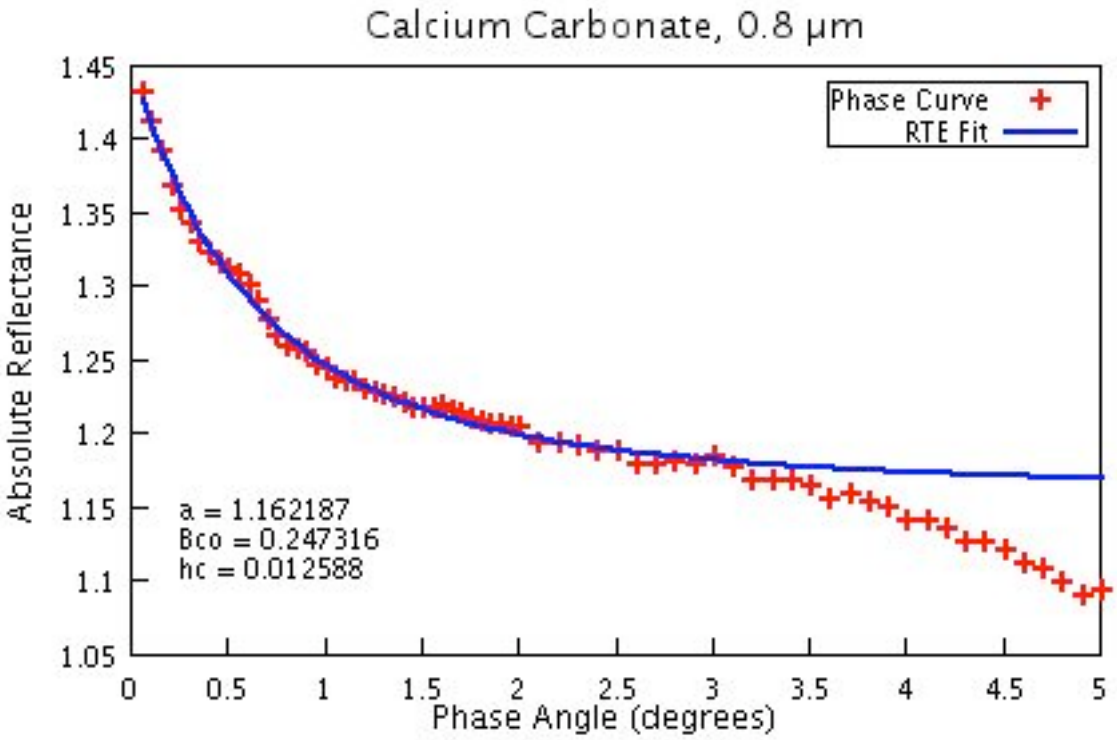

Figure 14b: Long arm phase curve for 0.8 μm calcium carbonate.

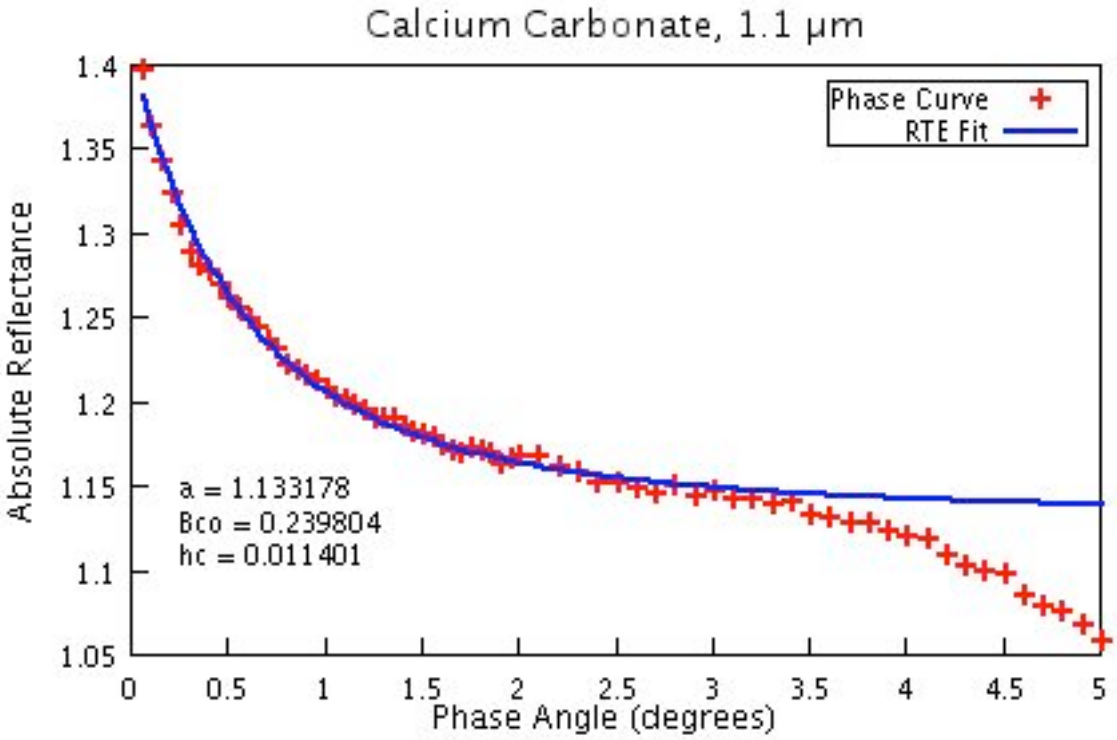

Figure 14c: Long arm phase curve for 1.1 μm calcium carbonate.

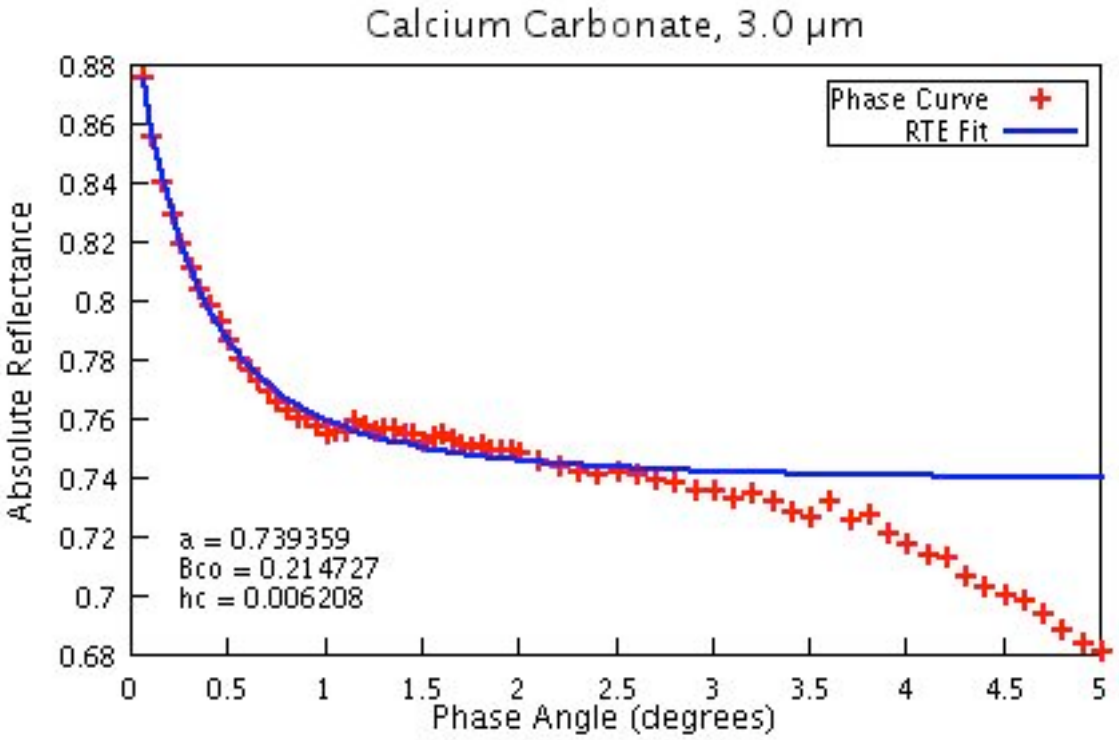

Figure 14d: Long arm phase curve for 3.0 μm calcium carbonate

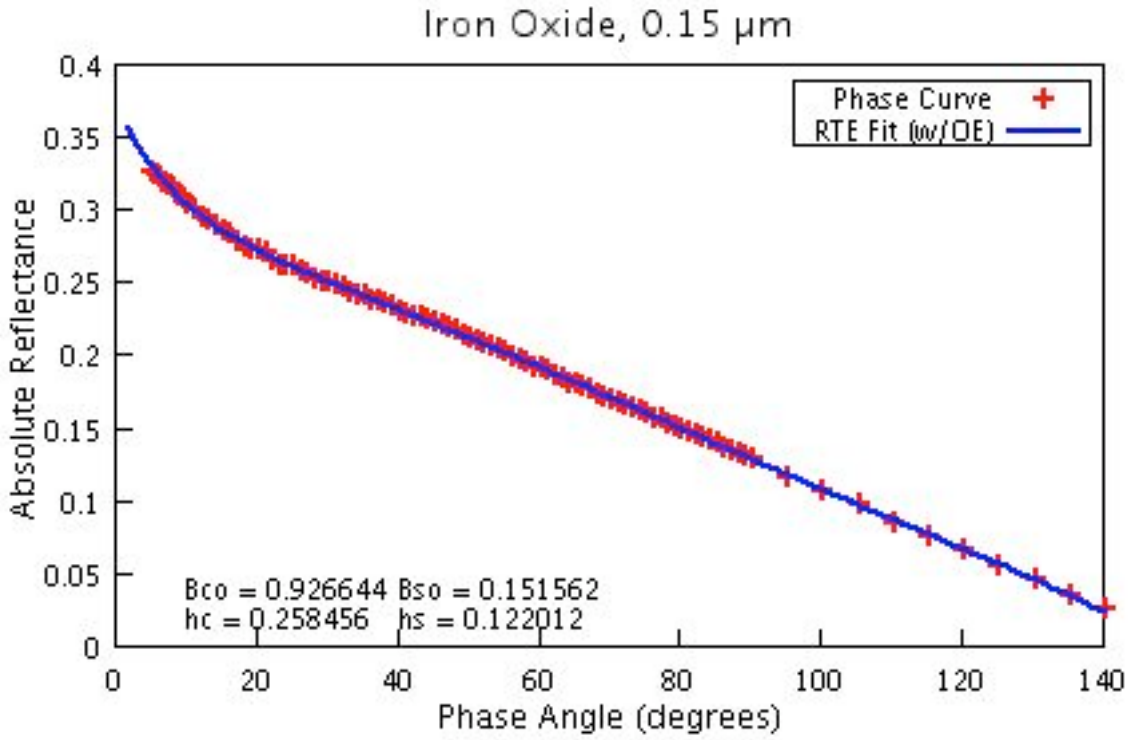

Figure 15a: Iron oxide short arm phase curves and model fits, including the opposition effect, labeled by nominal particle diameter. Single scattering functions as the same as shown in Figure 16. Opposition effect model parameters are listed in the lower left hand corner of each graph.

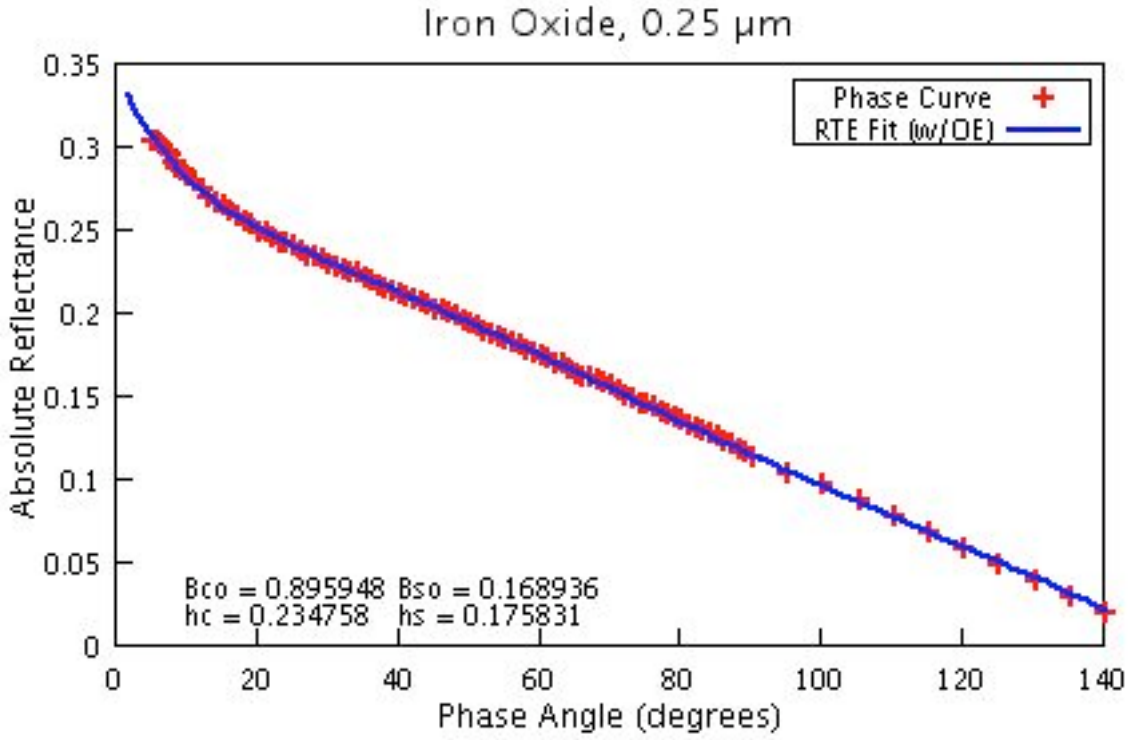

Figure 15b: Short arm phase curve and model fit (including opposition effect) for 0.25 μm iron oxide.

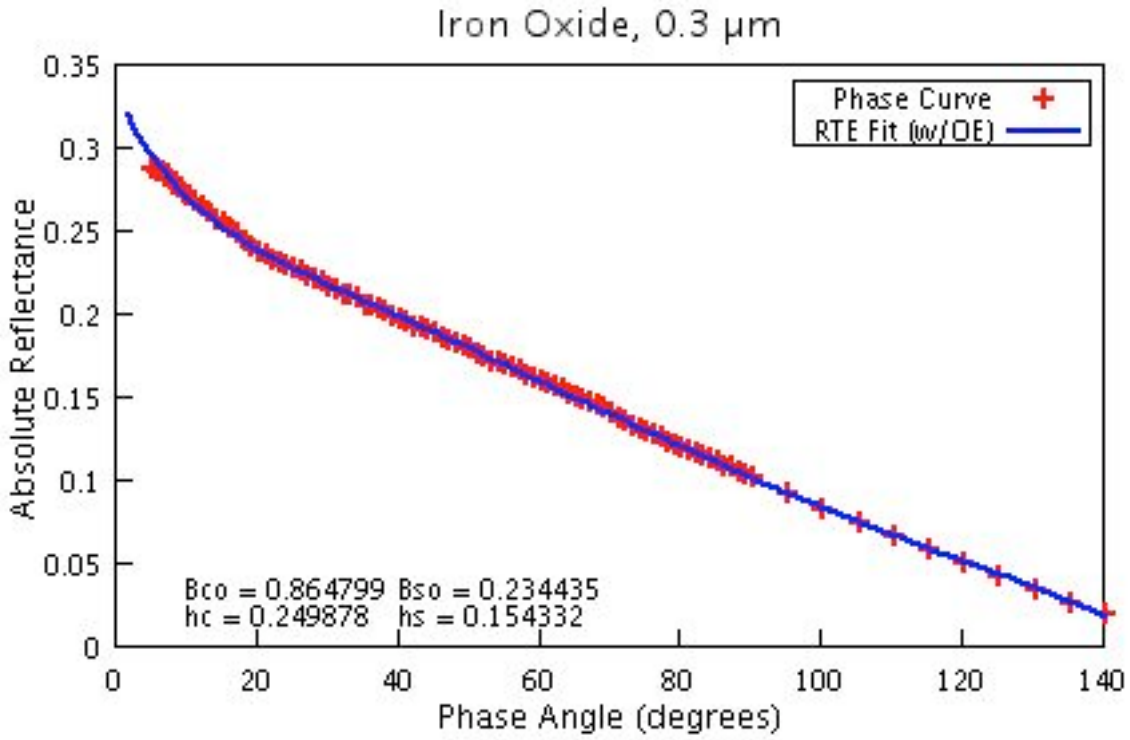

Figure 15c: Short arm phase curve and model fit (including opposition effect) for 0.3 μm iron oxide.

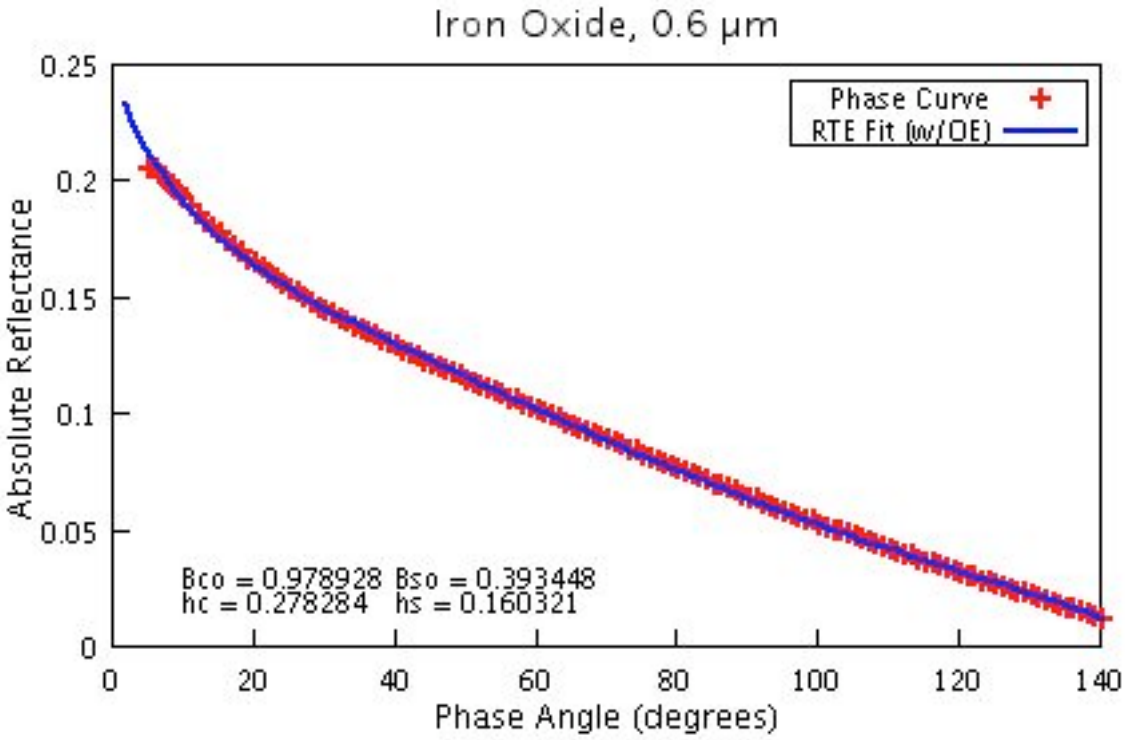

Figure 15d: Short arm phase curve and model fit (including opposition effect) for 0.6 μm iron oxide.

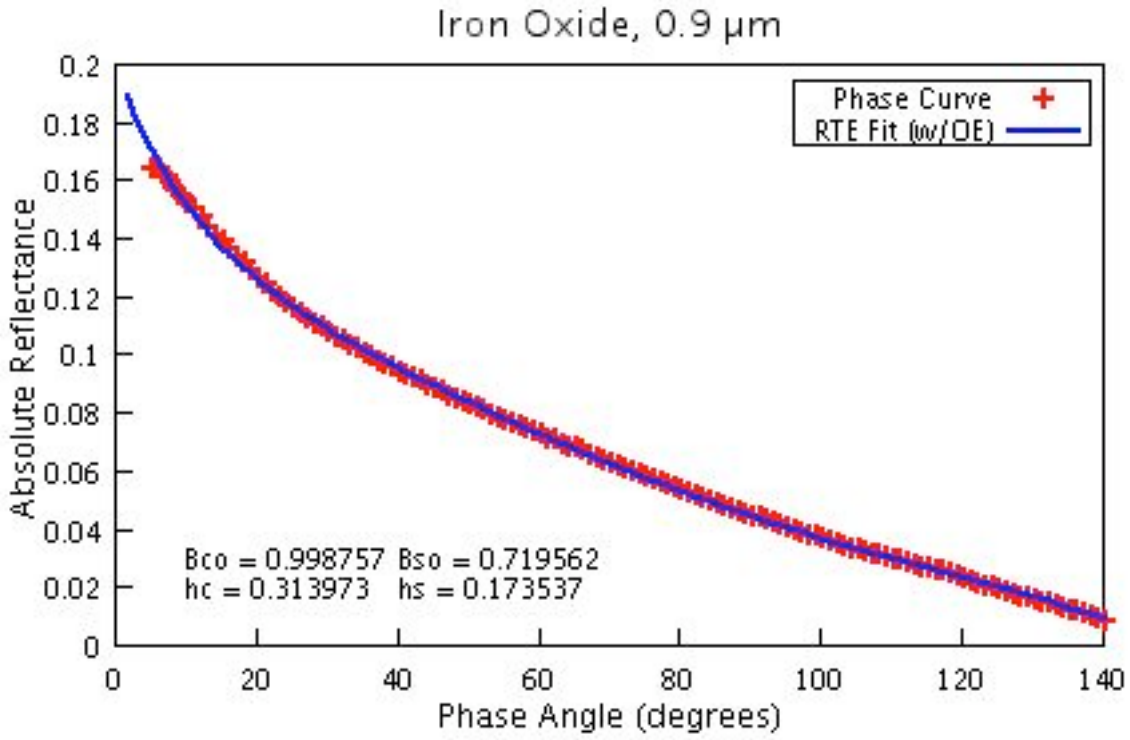

Figure 15e: Short arm phase curve and model fit (including opposition effect) for 0.9 μm iron oxide.

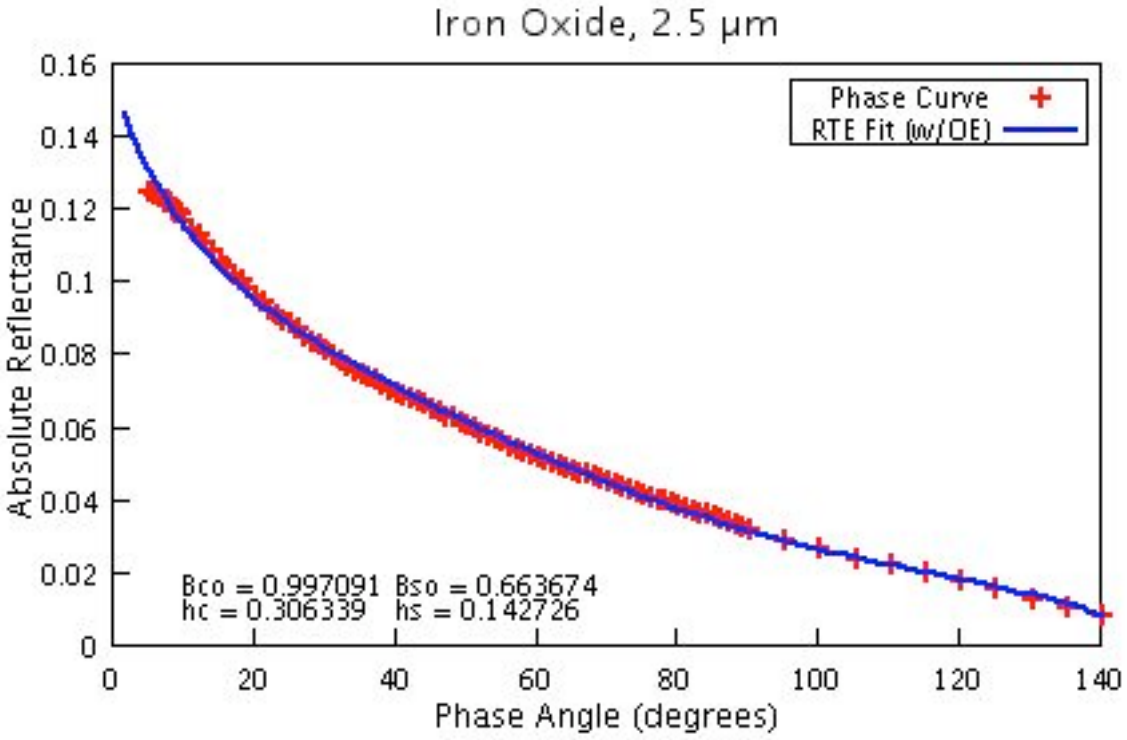

Figure 15f: Short arm phase curve and model fit (including opposition effect) for 2.5 μm iron oxide.

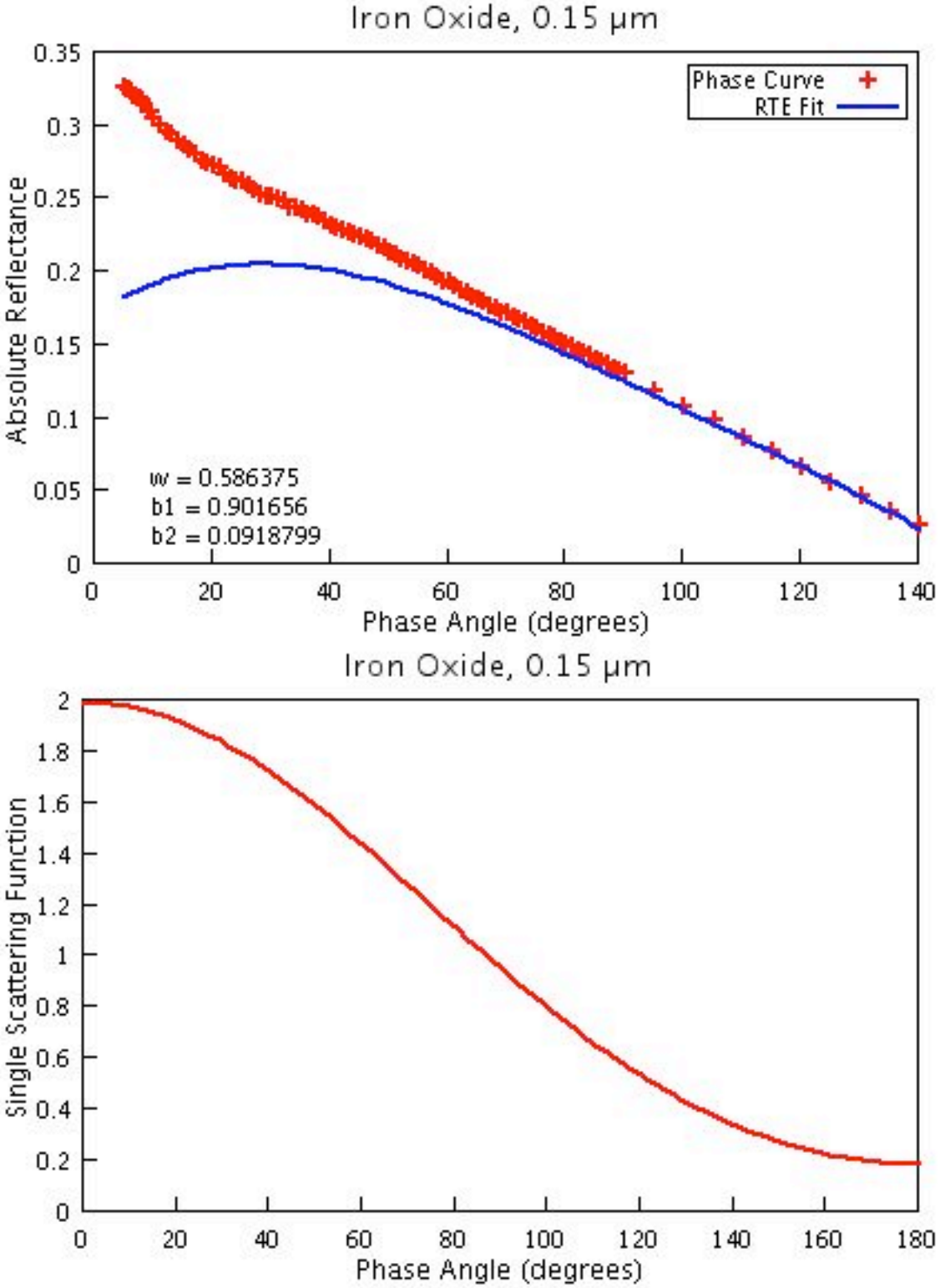

Figure 16a: Iron oxide short arm phase curves and model fits (not including the opposition effect), and single scattering functions, expressed as 2nd order Legendre polynomials. Figures are labeled by manufacturer's nominal particle diameter, and labeled with model parameters. Graphs shown above are for the 0.15 μm sample.

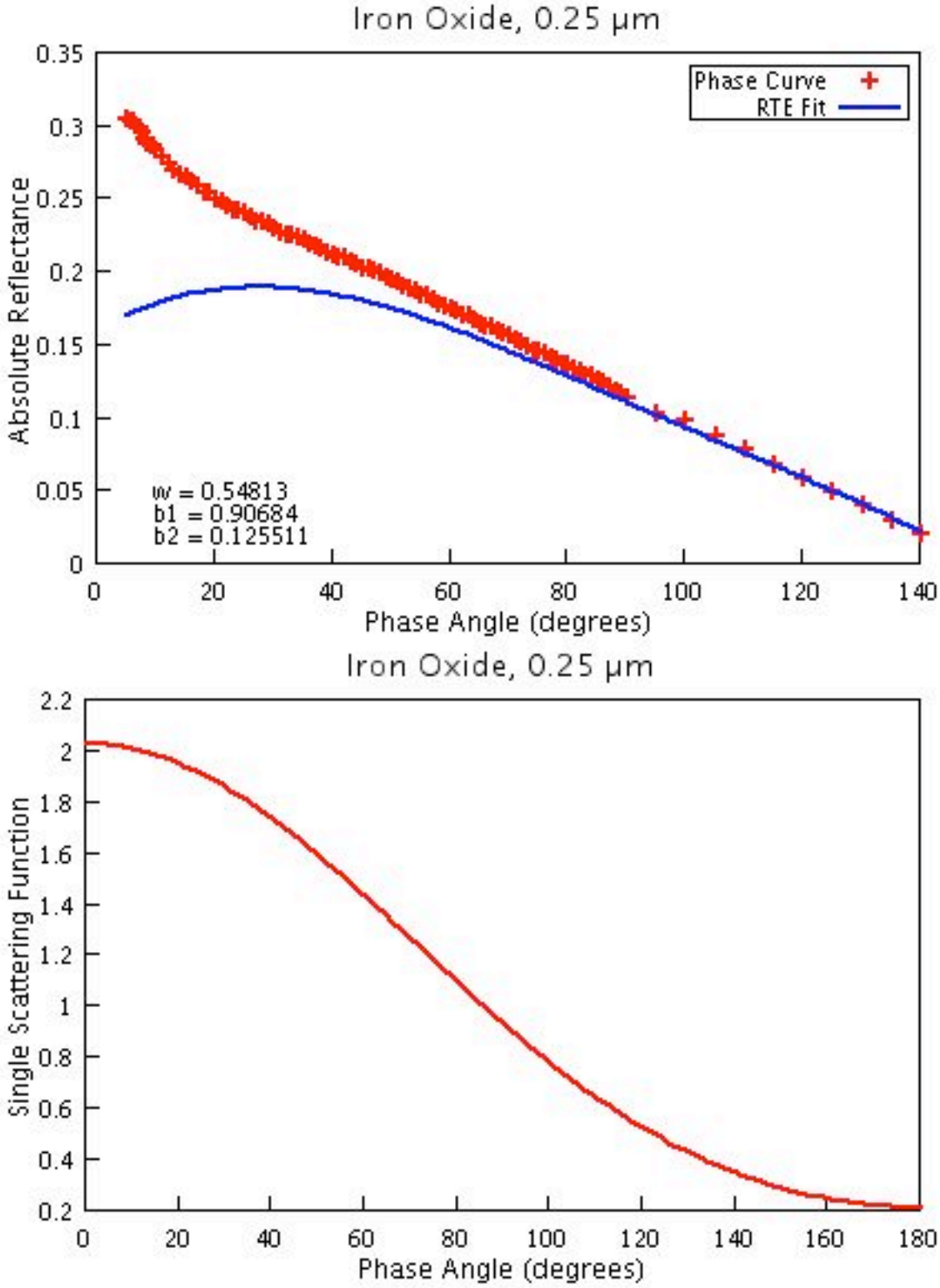

Figure 16b: Short arm phase curve, model fit, and single scattering function for 0.25 μm iron oxide.

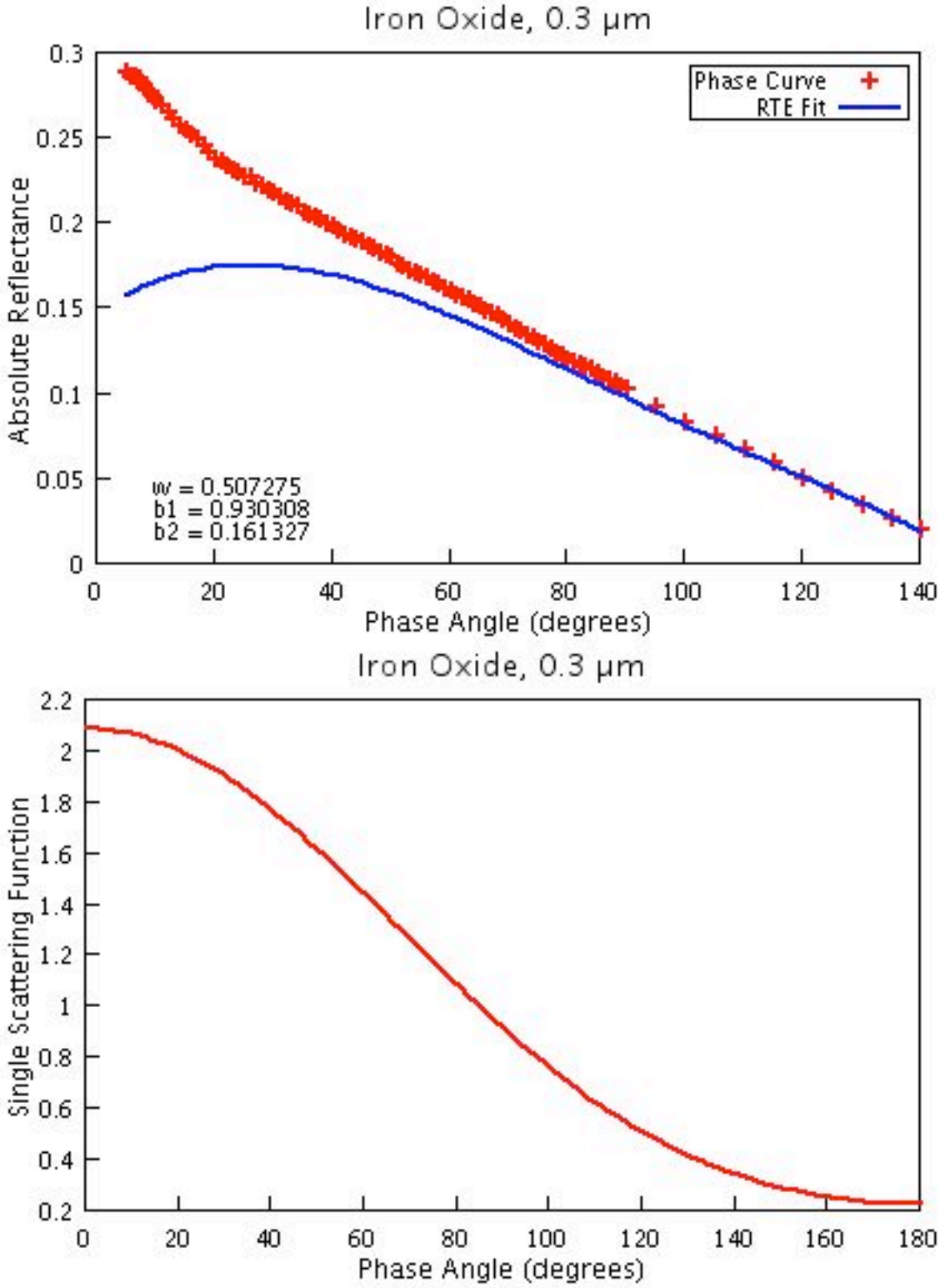

Figure 16c: Short arm phase curve, model fit, and single scattering function for 0.3 μm iron oxide.

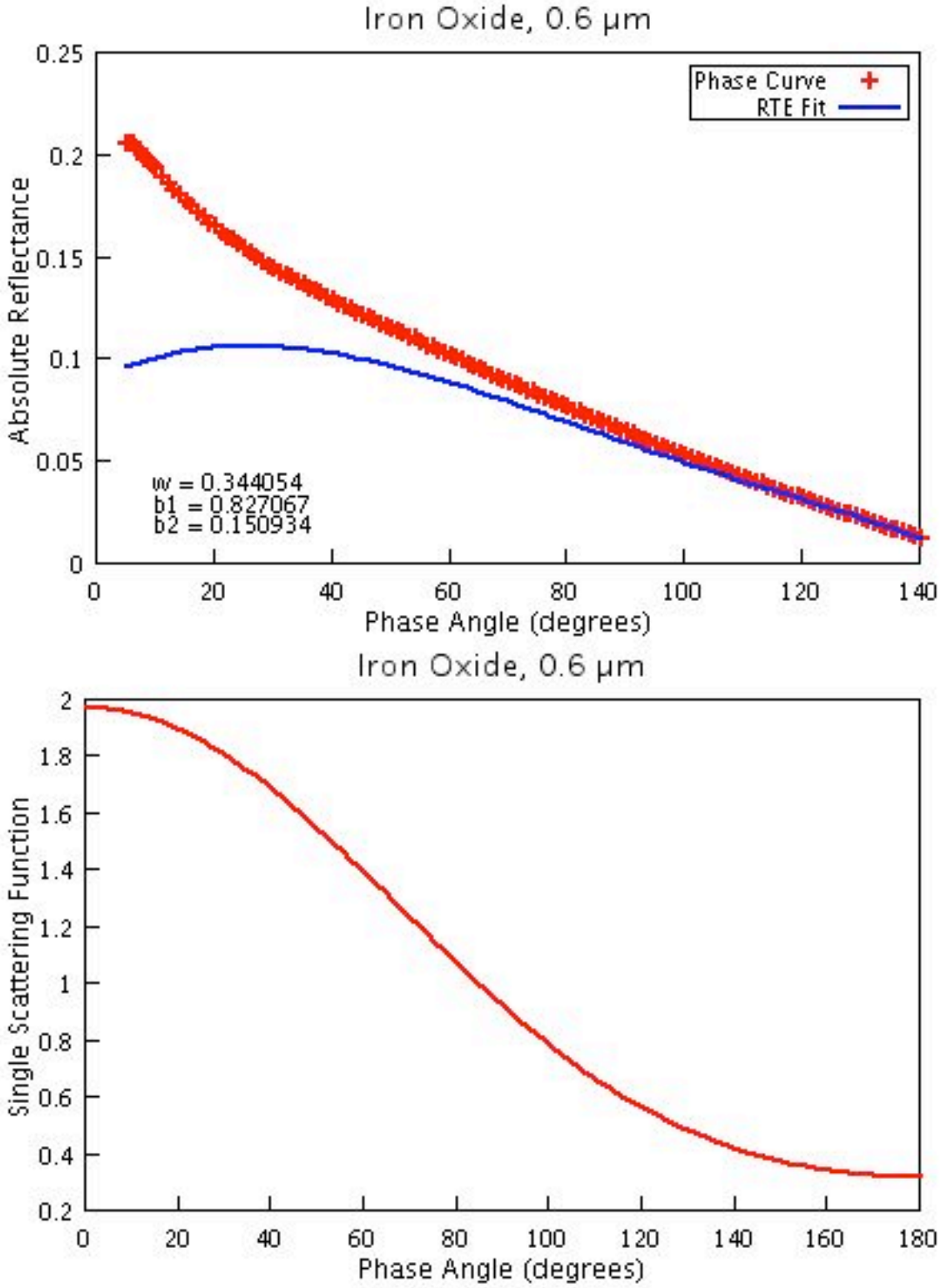

Figure 16d: Short arm phase curve, model fit, and single scattering function for 0.6 μm iron oxide.

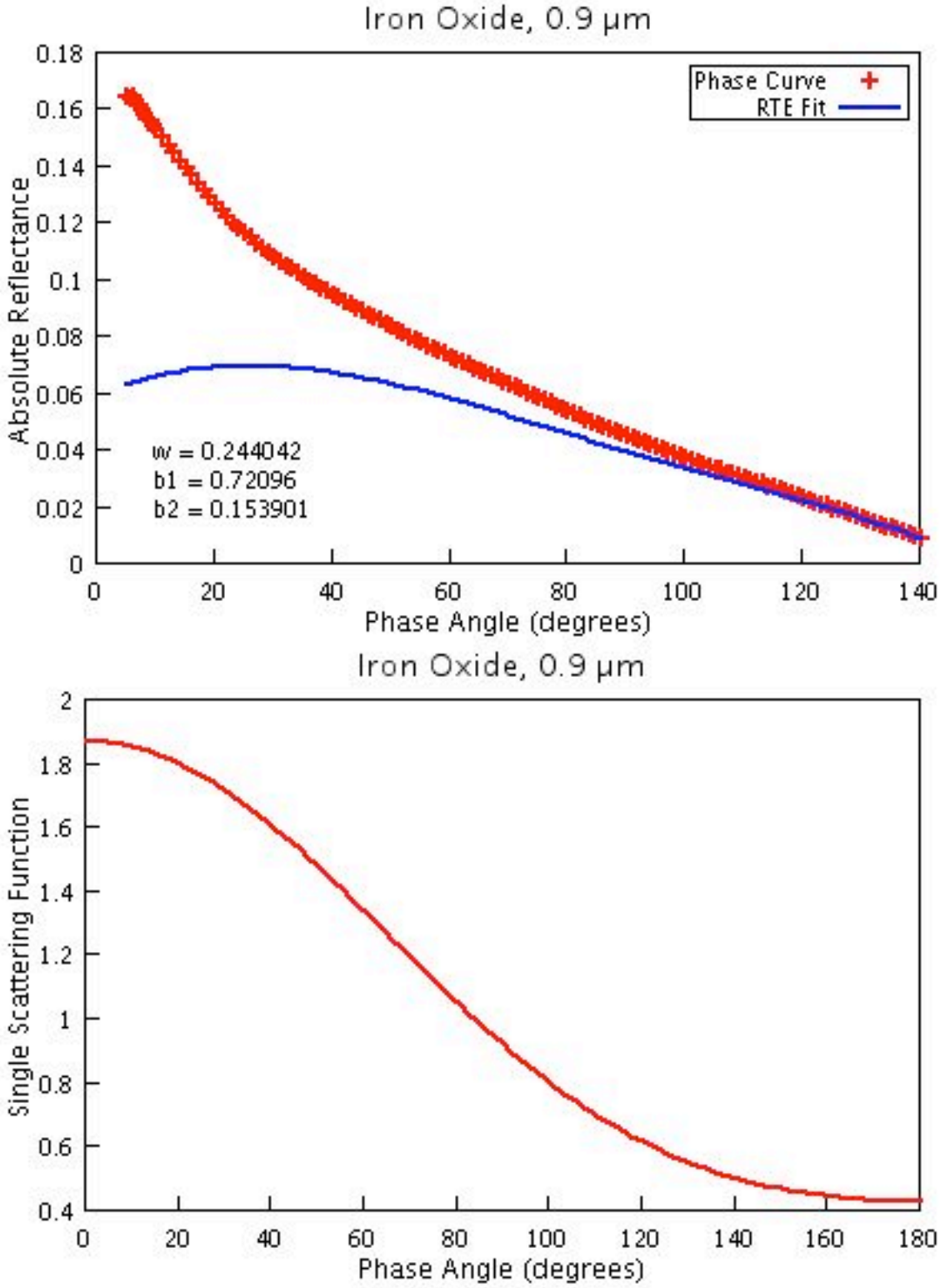

Figure 16e: Short arm phase curve, model fit, and single scattering function for 0.9 μm iron oxide.

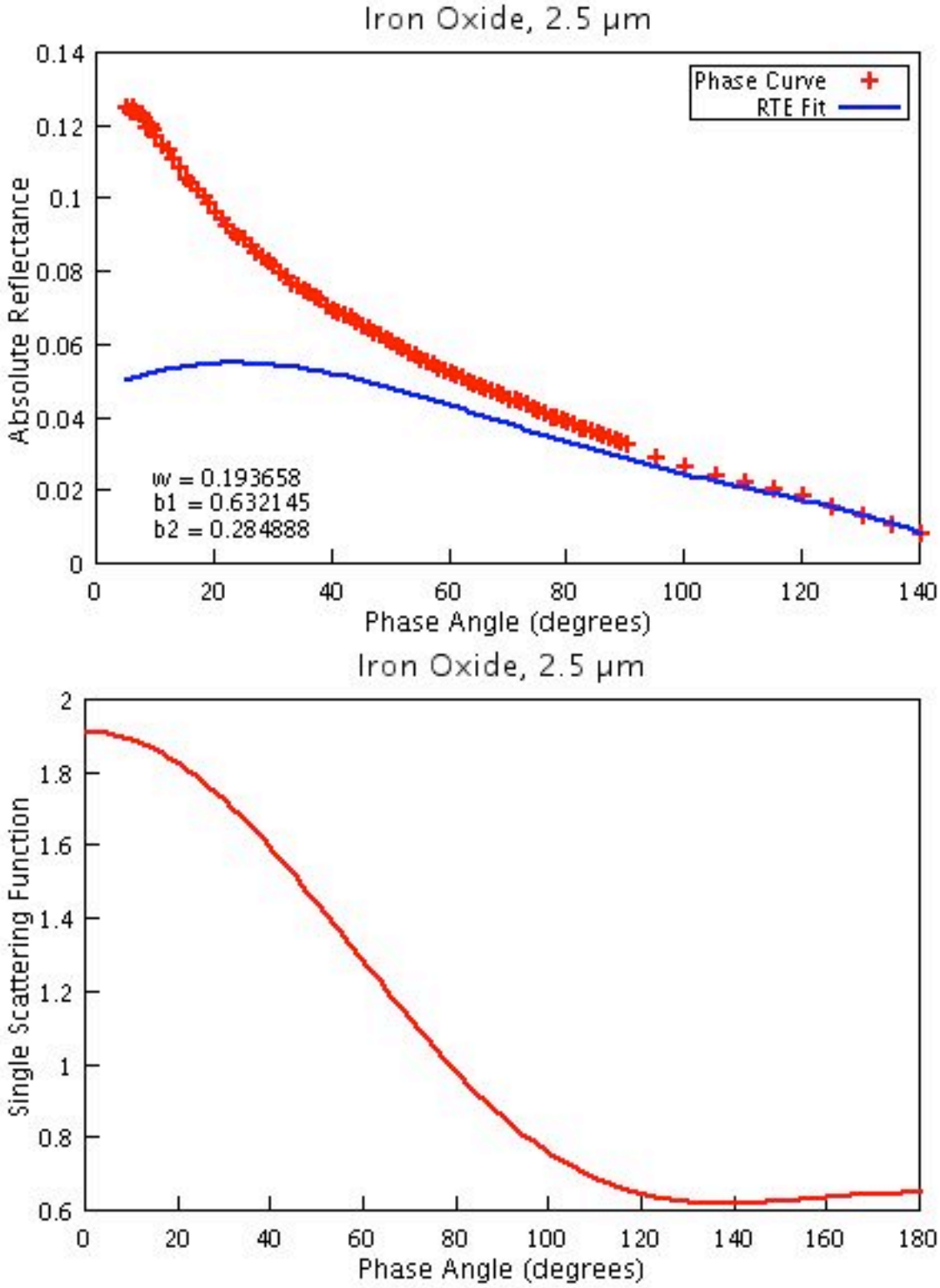

Figure 16f: Short arm phase curve, model fit, and single scattering function for 2.5 μm iron oxide.

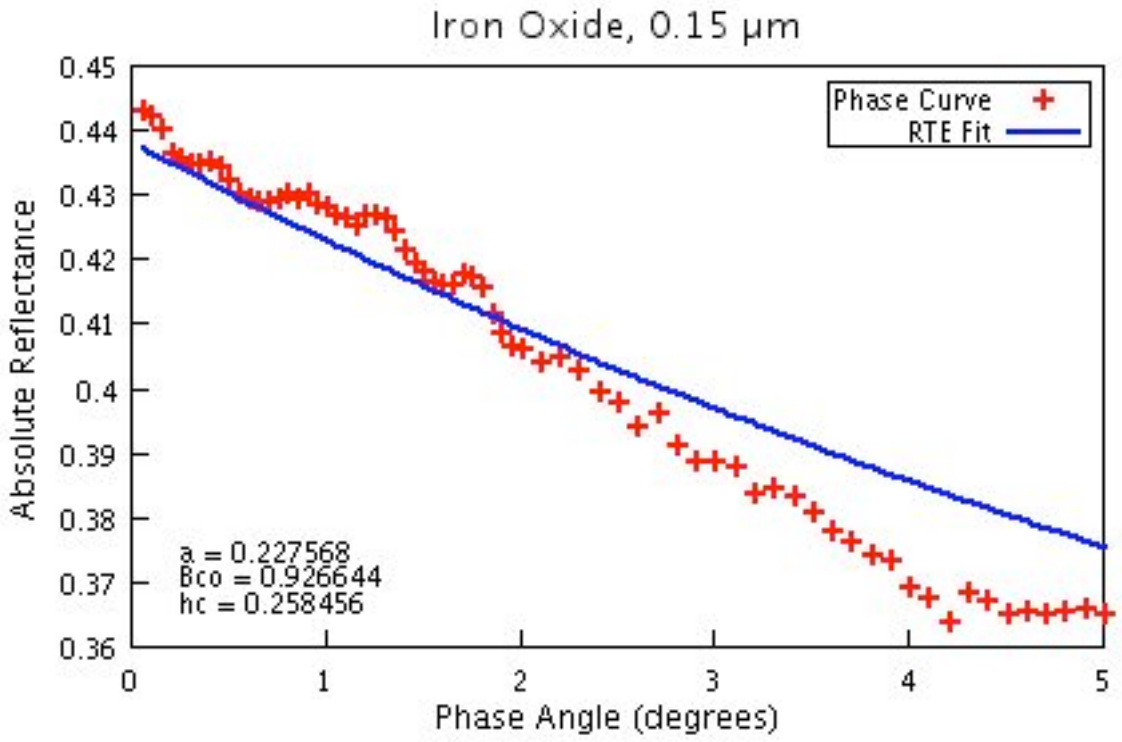

Figure 17a: Iron oxide long arm phase curves and model fits, using the simplified model $R = A \cdot B_{CB}$. Model parameters are listed on each graph: values for B_{CO} and h_c are the same as used in the shortarm fits in Figure 15. Graphs are titled with the nominal particle diameter. Shown above is the plot for 0.15 μm iron oxide.

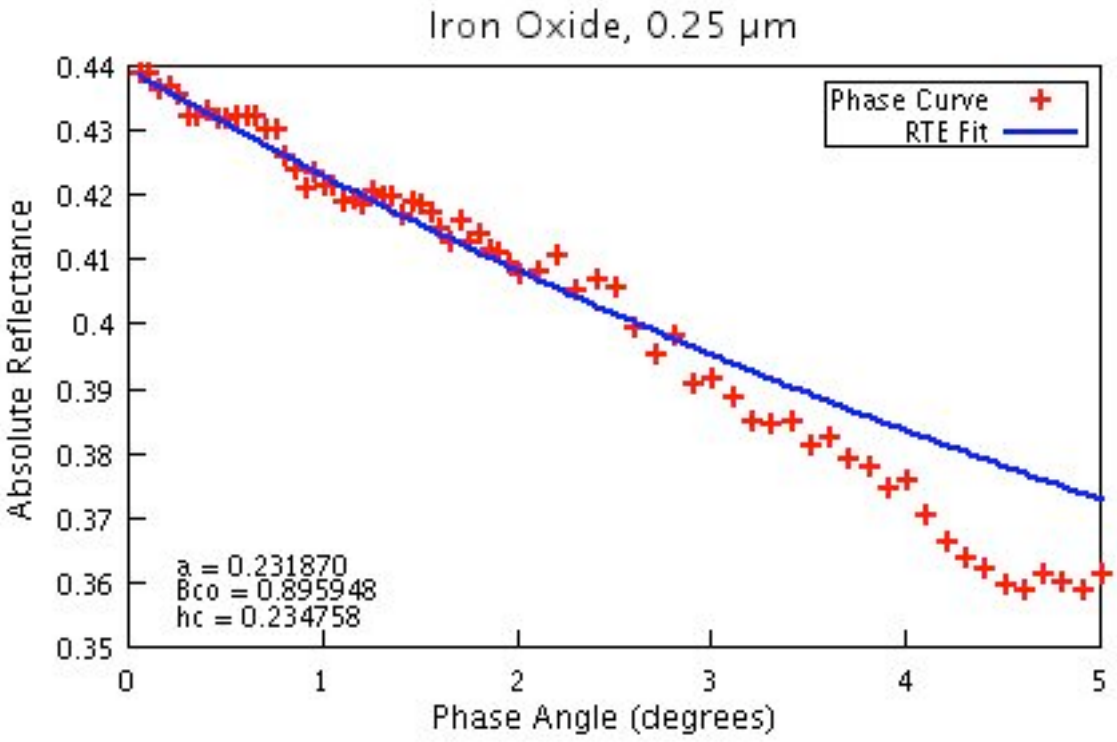

Figure 17b: Long arm phase curve and model fit for 0.25 μm iron oxide

.

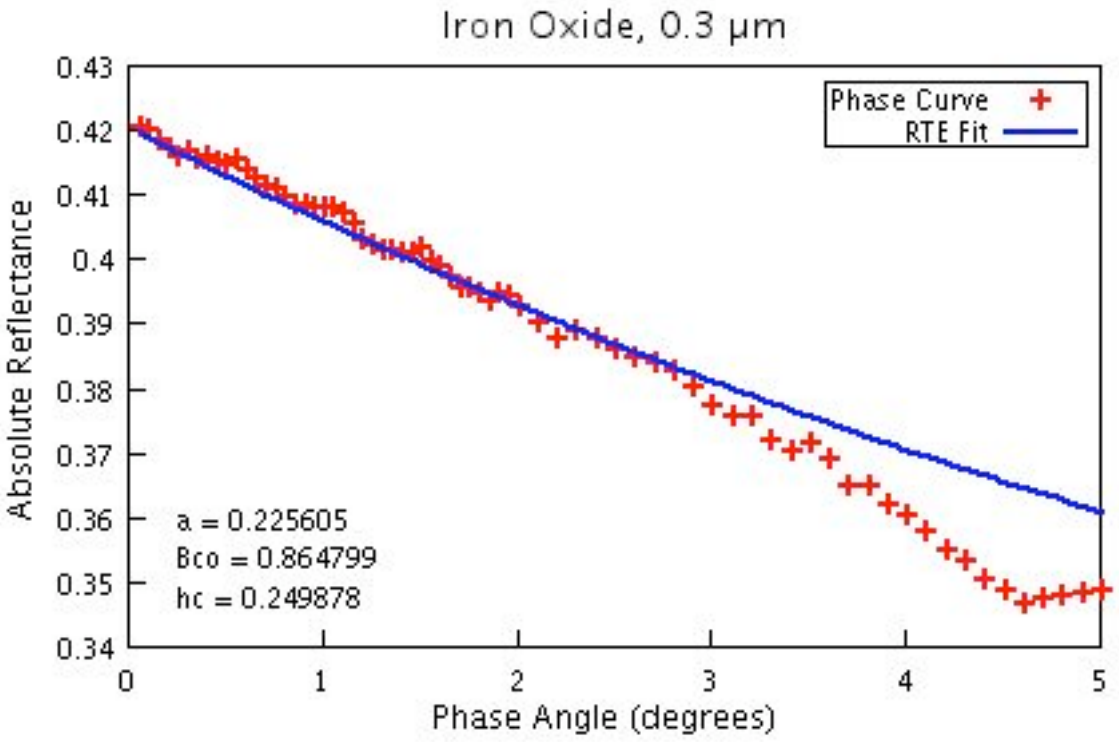

Figure 17c: Long arm phase curve and model fit for 0.3 μm iron oxide.

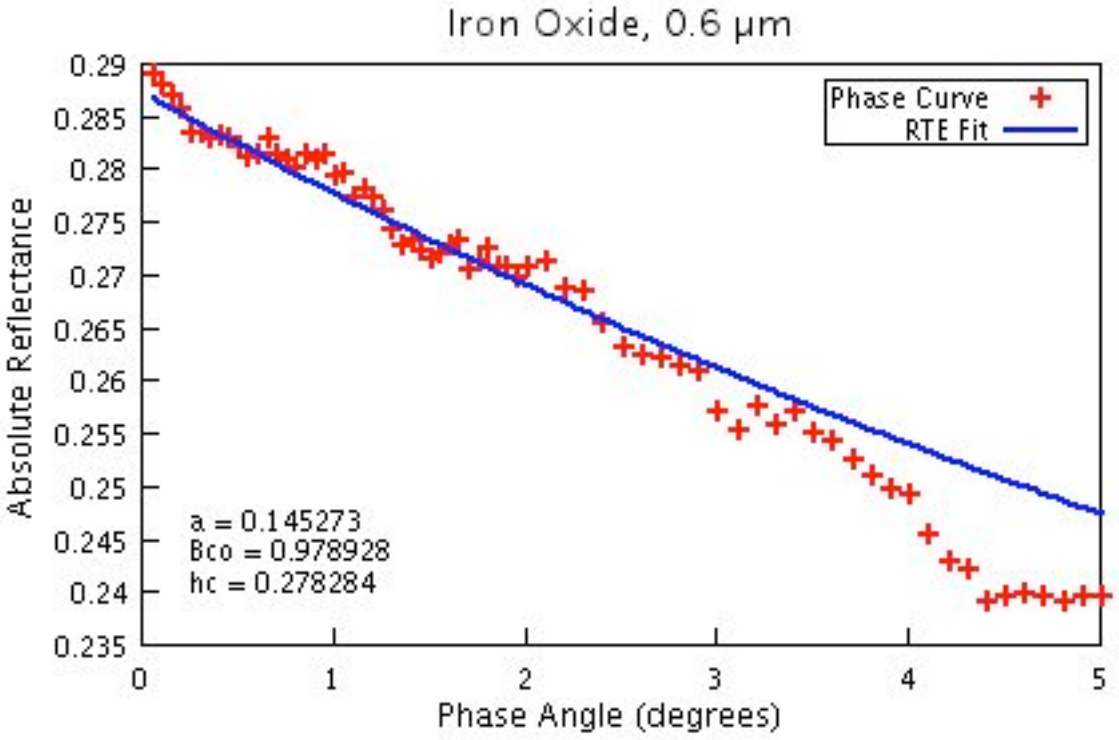

Figure 17d: Long arm phase curve and model fit for 0.6 μm iron oxide.

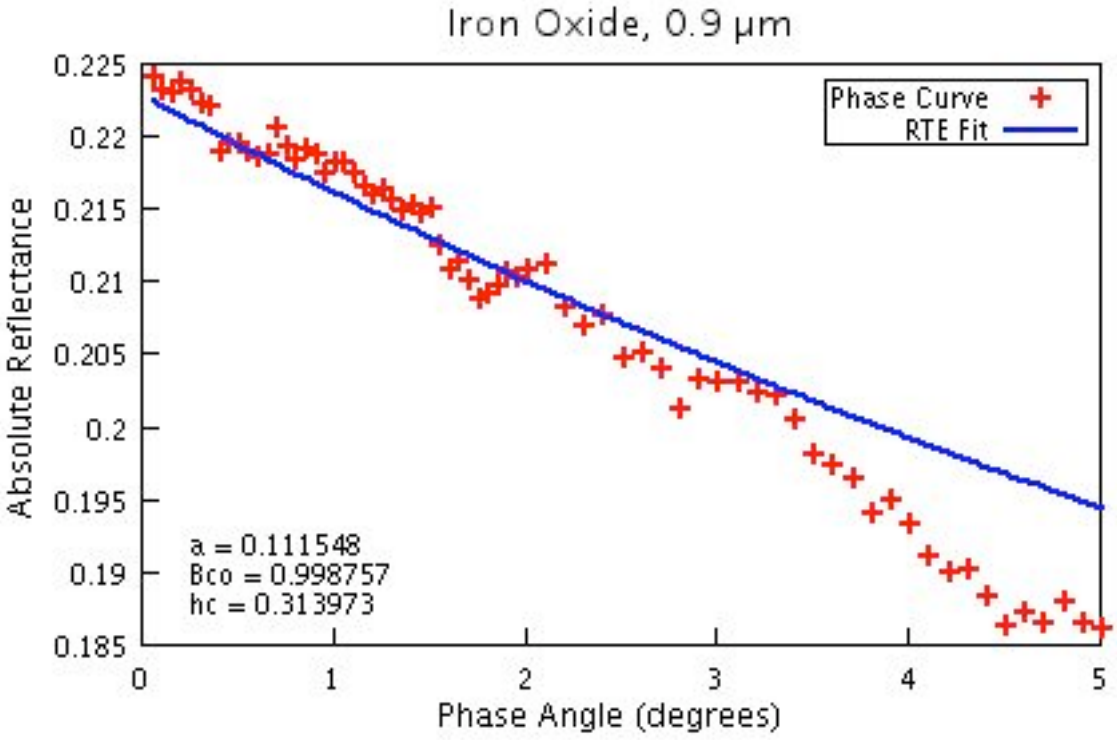

Figure 17e: Long arm phase curve and model fit for 0.9 μm iron oxide.

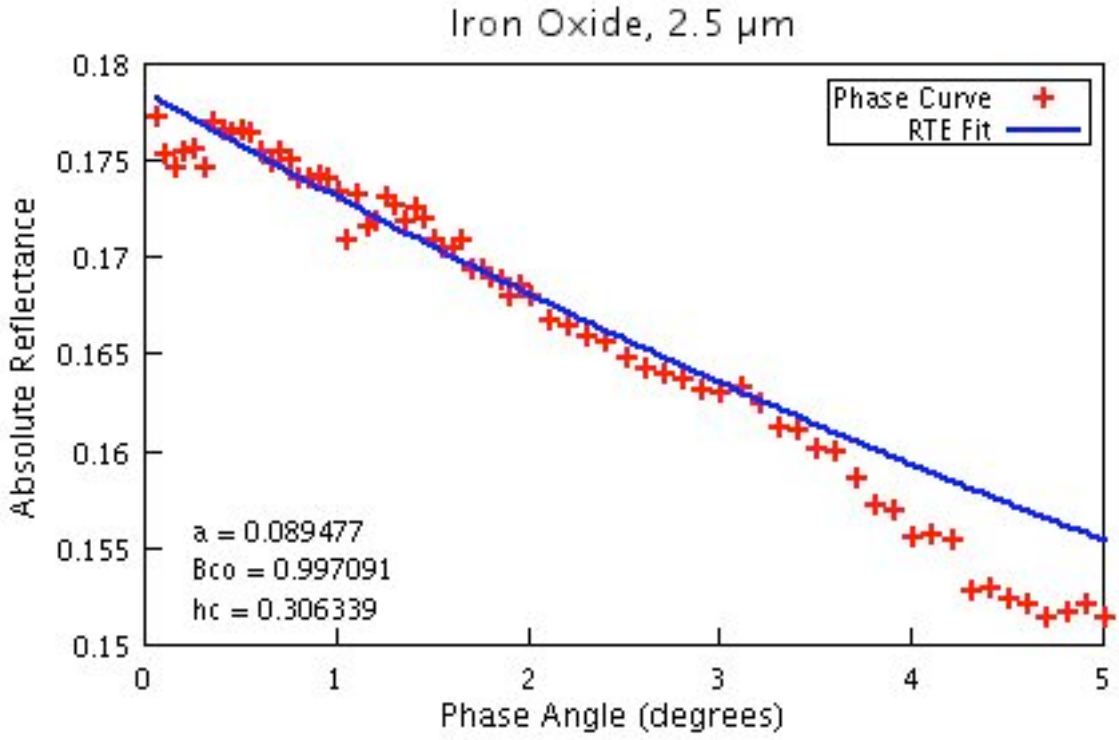

Figure 17f: Long arm phase curve and model fit for 2.5 μm iron oxide.

Because there are more data points in each phase curve than parameters, the fitting problem is mathematically over-determined. As is always true for an over-determined situation, the uniqueness of these fits is debatable. It should be clear, from an examination of the curve fits, that no fit is perfect. This is certainly due in part to experimental error, and this makes the curve fitting difficult. In this case, the "best" fit was determined to be the curve that by visual inspection seemed to best fit as much of the data as possible, and also a point where additional iterations did not provide a better fit. In some cases a good fit could not be obtained over the entire shortarm phase curve. In this case, it was assumed that the surface of the sample was not perfectly smooth, causing shadows at the largest phase angles. If an acceptable fit to the entire curve could not be determined, the result that best fit the smallest phase angles while remaining somewhat close to the larger phase angles was subjectively chosen as the "best fit".

The curve fits were completed using both user-guided fitting and unassisted computer fitting. Two computer applications were utilized for this purpose: gnuplot 3.7.1, and grace 5.1.4. Both public domain software packages are available at no cost online (at this time, gnuplot at http://www.gnuplot.info, and grace at http://plasma-gate.weizmann.ac.il/Grace). The gnuplot program does not have a GUI interface, but its strong point is its availability for a number of operating systems (including Unix, Linux, Macintosh, and Windows); for this study, a laptop running RedHat Linux 6.2 and a desktop G4 Macintosh running OS X were both used to produce fits. Grace is an improved version of the old Unix application xmgr, and has both a GUI and command line mode. Among other features, Grace is capable of placing constraints on parameters to be fit (limiting the albedo to a number between 0 and 1, for example), and can also be used to manipulate datasets mathematically (subtract a fit from a dataset to produce another suite of data, for example). Gnuplot has neither of these capabilities. On the con side, Grace is

only available for systems running X windows (in this case, X windows running over Linux or Mac OS X), and the length of the equation to be fitted is limited.

In both cases, the model equations were stored in a text file using a C-like syntax, and were loaded when necessary. User-guided fitting entailed plugging acceptable-seeming numbers into the model and seeing what the result was; the parameters could then be changed to obtain a better fit. This method was useful for roughly determining the scattering parameters before allowing the computer algorithm to continue on its own. For the unassisted computer fitting, the application was given a set of input parameters and allowed to vary them until it had found a set of "best fit" parameters. Both programs use a Marquardt-Levenberg algorithm to do non-linear fits such as this one. This particular algorithm takes the difference between the calculated curve and the data, squares it, and attempts to minimize this number. A least-squares residual fitting method such as this is commonly used in any number of curve-fitting software packages (this particular algorithm is a popular choice by these programs as well). There are difficulties in using such a method; this algorithm has a tendency to focus on local maxima or minima in the fit, and requires a relatively accurate set of input parameters. If the input parameters are way off, or if the iterations through the algorithm produce a parameter that is quite distant from reality, then the result is a completely unacceptable fit. This is the reason that the initial parameter fits were undertaken by hand rather than unassisted, and why assigning limits to parameter values can be particularly useful.

The curve fitting routine noted above fits parameters, not functions. This leaves the user to input some equation to represent the single scattering function. For this study, the original attempts to fit the data used a common approximation for the single scattering function –

representation as a Legendre polynomial series. In this case, the series is expanded to include the 2nd order term:

$$p(g) = 1 + b1\cos g + (b1/2)(3\cos^2 g - 1) \quad (21)$$

where b1 and b2 are simply coefficients to the appropriate Legendre polynomials, and are varied to fit the curve. The only constraint on these parameters is that the single scattering function, which represents the amount of light scattered by a particle at a given phase angle, must be positive for all angles between 0° and 180°. This representation was sufficient to fit the iron oxide data, but it was impossible to fit the aluminum oxide data with a single scattering function of this style,, and the fits to the calcium carbonate data were unsatisfactory as well. For the latter samples, a third order Legendre polynomial:

$$p(g) = 1 + b1\cos g + (b2/2)(3\cos^2 g - 1) + (b3/2)(5\cos^3 g - 3\cos g) \quad (22)$$

proved to be sufficient to fit the data, but this was not the case for the remaining samples. Simply put, the aluminum oxides were too reflective; the combination of a 2nd or 3rd order Legendre polynomial expansion and the single scattering albedo (plus the appropriate constraints) did not produce enough reflectance to match the observed phase curves. The solution was to replace the Legendre polynomial expansion with a double Henyey-Greenstein function.

An expression for the single scattering function that is common in the literature is a double Henyey-Greenstein function (Henyey and Greenstein, 1941, eq. 2), which has the form:

$$p(g) = \frac{1-c}{2}\left[\frac{1-\gamma_1^2}{(1+2\gamma_1\cos g+\gamma_1^2)^{3/2}}\right] + \frac{1+c}{2}\left[\frac{1-\gamma_2^2}{(1-2\gamma_2\cos g+\gamma_2^2)^{3/2}}\right] \quad (23)$$

where c, γ_1, and γ_2 are parameters to be identified during fits. Commonly, γ_1 and γ_2 are replaced by one term (γ); this is referred to as a symmetric double Henyey-Greenstein function, while the

form given above is asymmetric. While both versions were used to try to fit the aluminum oxide shortarm data, the asymmetric version invariably produced a better fit. A 5th order Legendre polynomial expansion of this function was necessary to calculate the components of the multiple-scattered term. For the asymmetric case, this expansion is (based on the expansion of Hapke, 2002, for a symmetric double Henyey-Greenstein function, p. 529):

$$\begin{aligned} p(g) &= \frac{1+c}{2}\left[1+\sum_{n=1}(2n+1)(b_1)^n P_n(\cos g)\right]+\frac{1-c}{2}\left[1+\sum_{n=1}(2n+1)(-b_2)^n P_n(\cos g)\right] \\ &= 1+\sum_{n=1}\frac{(2n+1)}{2}\left[(1+c)(b_1)^n+(1-c)(-b_2)^n\right]P_n(\cos g) \end{aligned} \tag{24}$$

where $P_n(\cos g)$ are nth degree Legendre polynomials. The components of the multiple-scattering term M can then be calculated from this representation (see Appendix 2).

For each given representation of p(g), there are two or three parameters that are introduced into the model equations. Combined with the single scattering albedo and the parameters for both the opposition effect terms, there are seven or eight variables that are varied to produce best fits. This is a rather large number to manipulate while fitting, so first order fits were completed by ignoring the opposition effect and fitting the short arm phase curves with only the single scattering function and the single scattering albedo as fit parameters. The values of the parameters are limited to those that produce single scattering functions that are positive for all angles 0-180° inclusive, and for $0 < w < 1$. For the calcium carbonate and aluminum oxide samples, the fits to the short arm phase curves showed little or no effect of the opposition surge in the shortest phase angles; that is, the parameters that fit the largest phase angles produced a curve that fit all but the smallest phase angles measured. For these samples, the long arm phase curves were used to determine the contributions of the opposition effect.

The long arm phase curves used here were obtained after the Goniometer Laboratory at JPL had changed locations. During the move, the long arm goniometer had to be disassembled. Data taken after the move showed a drop-off in sample reflectance at phase angles larger than 3°. The cause was later determined to be a kink in the fiberoptic cable that formed when the detector arm moved beyond a certain point; this kink reduced the signal that reached the detector. Although this situation has now been rectified, all of the long arm data used in this study have this particular defect, so all data beyond 2.5° were ignored during fitting. Because of the lack of this larger phase angle data, it was impossible to fit the shadow hiding opposition surge, which should be wider than the coherent backscatter surge and therefore best fit at the larger phase angles. In addition, the magnitude of the long arm and short arm phase curves did not always match at g=5°, so it was not possible to simply transfer the model parameters from the short arm fits to the long arm. Instead, a simpler equation was used to fit these data:

$$R = A \cdot B_{CB} \tag{25}$$

where A is a constant representing the background intensity, and B_{CB} is the coherent backscatter term defined in Equation (20). The assumption of a constant background intensity is valid for a small range of phase angles (such as this), over which the background phase curve doesn't change significantly. This background term A, as well as the width and amplitude of the coherent backscatter opposition surge, were varied to best fit the long arm curves at phase angles smaller than 2.5°, with the constraint that the amplitude parameter must not exceed 1. The results are shown in Figures 12, and 14. Data from the long arm goniometer for the aluminum oxide samples was previously published by Nelson *et al.* (2000). The data in this work were not marred by the kinked fiberoptic cable, and extend out to 5°. For comparison purposes, these data have also been analyzed using fit method described above. The results for the analyses

performed on their data using the methods of this study agree well with the results for the data obtained for this study. All further discussion of the aluminum oxide long arm data will focus on the results determined from the data acquired for this study.

The iron oxide samples were completely different. The circular polarization ratio — defined as the ratio of scattered intensity with same helicity detected as incident over the scattered intensity with the same helicity incident but the opposite detected — shows a sharp upturn at small phase angles when the coherent backscatter opposition surge is present. For the iron oxide samples, this observation showed that the coherent backscatter opposition surge for these samples is extremely wide – ~40° (see Figure 18). In this case, the long arm phase curves would be too small to show the full opposition surge, so the contribution of both opposition effects were added into the model equations and fit to the data. First, the original variables (single scattering function and single scattering albedo) were fixed at values that fit only the large phase angles. The parameters of the opposition surges were then fit to the smaller phase angles (keeping the amplitudes of both opposition surges less than 1). This produced only fair model fits, so these values were then used as starting parameters for a final iteration, where all the parameters were allowed to vary. This final iteration produced the best fit curves shown in Figure 15; the same models without the contribution of the opposition surge are shown in Figure 16, and these illustrate the unusual width of the opposition surges for this material. In order to confirm the values for the coherent backscatter surge determined by the shortarm fits, these values were inserted into equation (25), and the background intensity term A was varied. In all six cases, this produced a very good fit to the long arm data (results are shown in Figure 17).

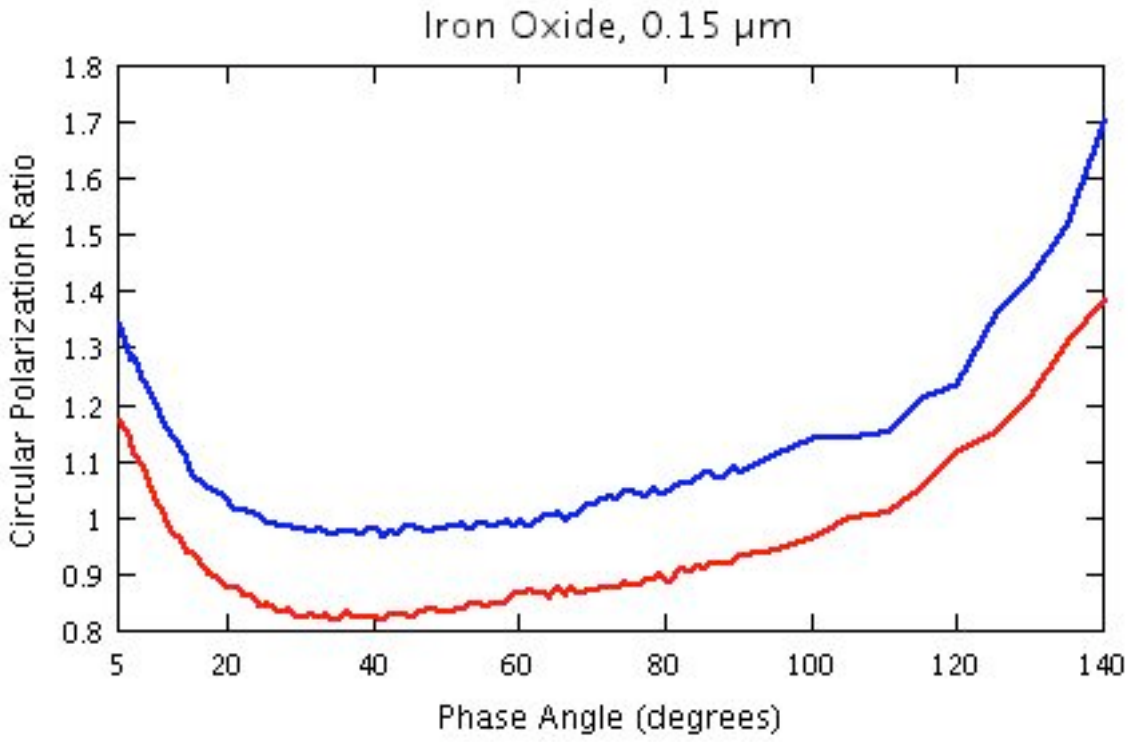

Figure 18a: Circular polarization ratios for iron oxide shortarm runs. The upturn at the smaller phase angles is the contribution of the coherent backscatter opposition surge. Shown in this figure are the results for the 0.15 μm sample.

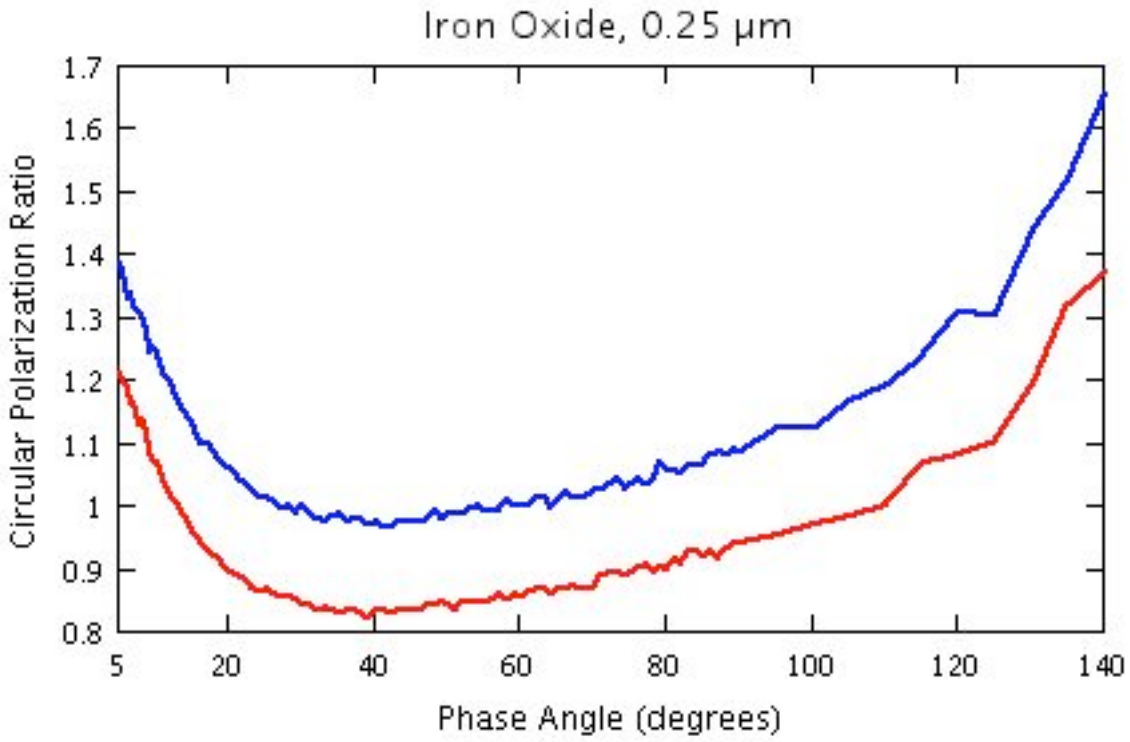

Figure 18b: Circular polarization ratios from short arm data for the 0.25 μm iron oxide.

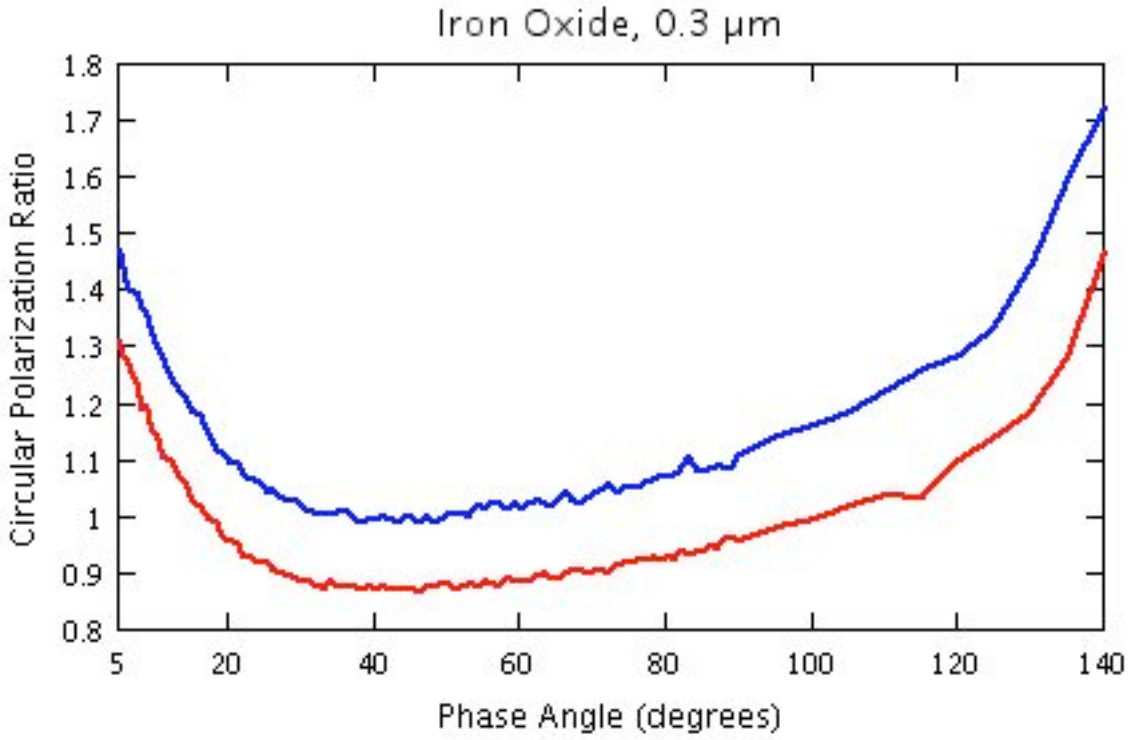

Figure 18c: Circular polarization ratios from short arm data for the 0.3 μm iron oxide.

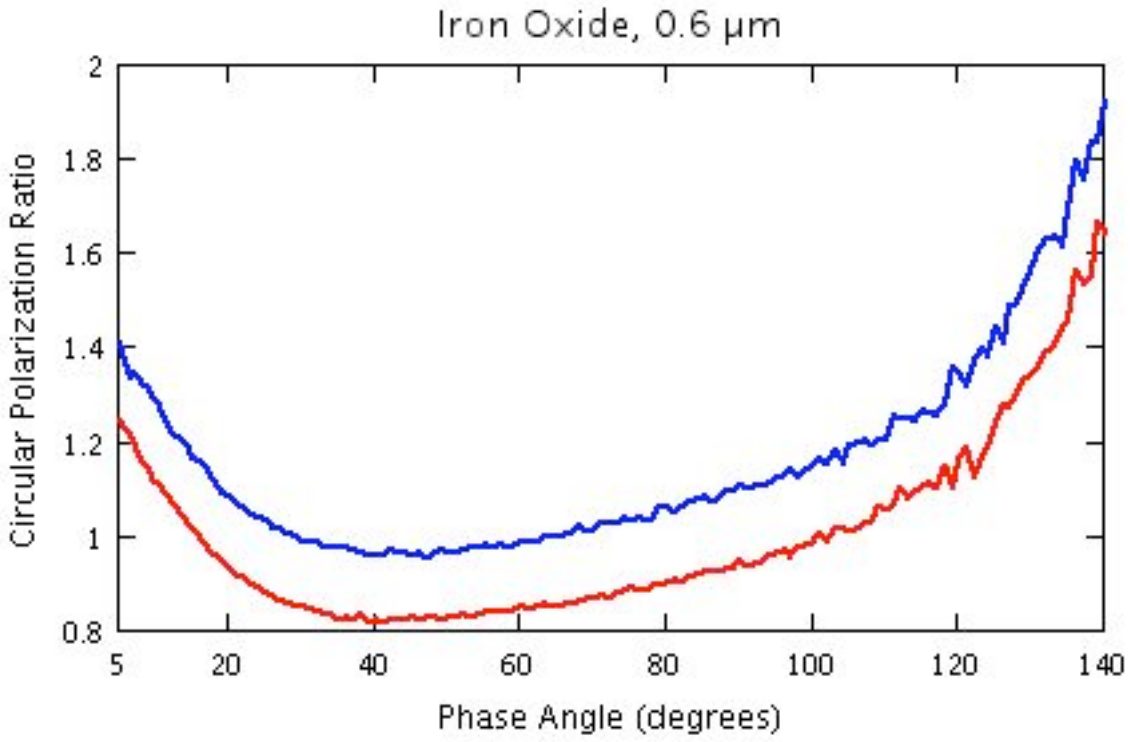

Figure 18d: Circular polarization ratios from short arm data for the 0.6 μm iron oxide.

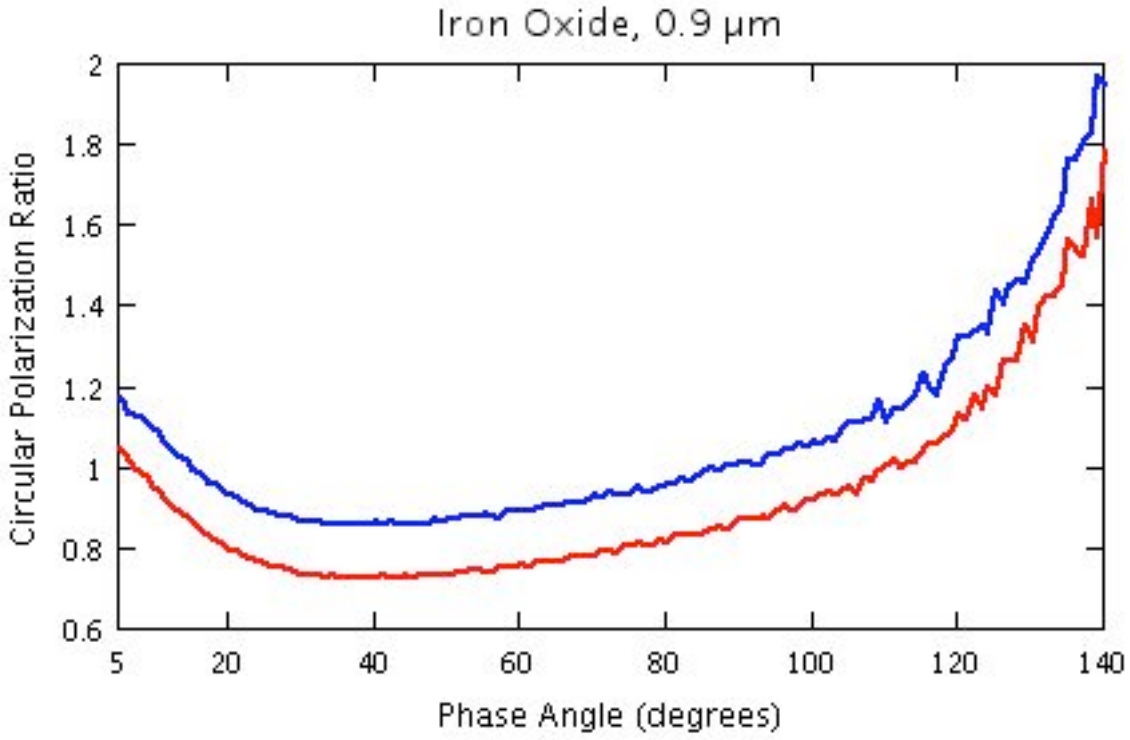

Figure 18e: Circular polarization ratios from short arm data for the 0.9 μm iron oxide.

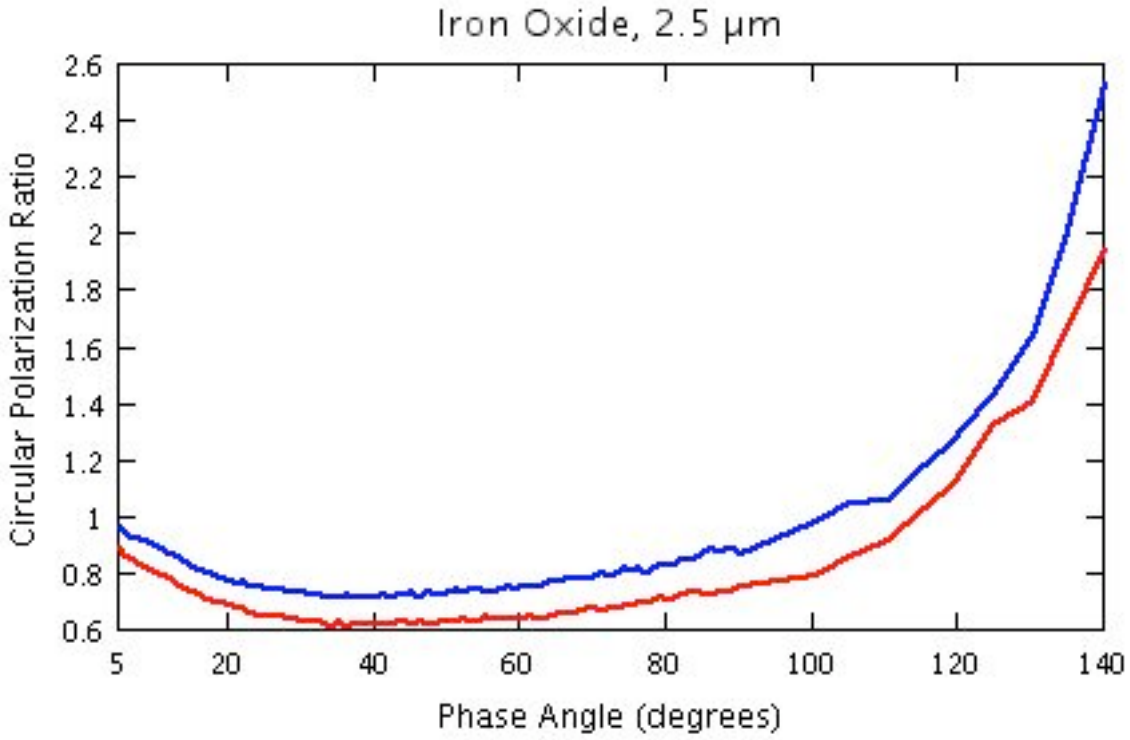

Figure 18f: Circular polarization ratios from short arm data for the 2.5 μm iron oxide.

The parameters that were determined directly from the model curve fits were the single scattering albedo, the single scattering function, and the width and amplitude of the coherent backscatter opposition surge. These parameters can then be directly related to the transport mean free path (L), the average scattering angle (<cosθ>), the scattering coefficient (S), and the extinction coefficient (E) by the equations given earlier. For the iron oxides, the width and amplitude of the shadow hiding opposition surge were determined as well. The transport mean free path of the sample can be directly calculated from the angular width term of the coherent backscatter opposition surge (measured in radians):

$$L = \frac{\lambda}{4\pi h_c} \tag{26}$$

where λ is the wavelength of the laser light (van Albada *et al*., 1987, page 362; Hapke, 2002, eq. 34). The half width at half maximum (HWHM) of the coherent backscatter opposition surge can be related to the transport mean free path (van Albada *et al*., 1987, caption of Figure 1):

$$HWHM = \frac{0.36\lambda}{2\pi L} \tag{27}$$

Replacing the transport mean free path L by the definition from equation (26) produces:

$$HWHM = 0.72 h_c \tag{28}$$

where the resulting half-width is measured in radians, rather than degrees.

Modeling of Media of Fundamentally Scattering Particles

In order to validate the fundamental particle scattering assumption, it was necessary to apply this assumption in calculating scattering parameters for comparison with those determined from laboratory experiments. Fundamental particle scattering theory assumes that the particles are the scattering units of the medium, and that the light scattered from each particle does not interact with the light from any of the other particles around it (hence the name). This is a

method of simplifying the mathematics involved. Additional simplifications often used include assumptions about particle geometry, size, and composition. The most widely used assumption is that of isolated spherical particles of a single size and composition, and we also adopt this assumption. Even though our particles are not perfect spheres, the scattering properties of spheres are representative of all particles, and should be sufficient to indicate the magnitudes and trends to be expected from media of independently scattering particles.

The solution to the scattering problem of a sphere can be derived directly from Maxwell's equations (Mie, 1908), and is commonly referred to as Mie theory. Rigorous derivations of this theory appear in a number of optics references (including van de Hulst, 1957; Born and Wolf, 1980; and Bohren and Huffman, 1983), and will not be reproduced here. The most efficient way of calculating Mie scattering parameters is through use of a FORTRAN program, such as the one given in the appendix of Bohren and Huffman (1983). Inputs for the program include the size of the particles, the wavelength of the scattered light, and the optical constants of the material (which are related to the composition).

Since the powders used in this study are known to have a range of particle sizes, rather than a single particle size per powder, a Mie code capable of including a size distribution was required. Such a program was described by Mishchenko *et al*. (1999a), which is available online at http://www.giss.nasa.gov/~crmim. The program requires an input size distribution in one of six different forms: gamma distribution, modified gamma distribution, power law, modified power law, log normal, and bimodal log normal. The last of these, the bimodal log normal defined by:

$$N(x) = C_1 r^{-4} \left[\exp\left[-\frac{\left(\ln x - \ln x_{g1}\right)^2}{2\ln^2 \sigma_{g1}} \right] + \exp\left[-\frac{\left(\ln x - \ln x_{g2}\right)^2}{2\ln^2 \sigma_{g2}} \right] \right], \tag{29}$$

provided the best fit to size histograms taken from SEM counting of samples used here (this function from Mishchenko *et al.*, 1999b, eq. 11 – corrected in an erratum; the remaining size distributions are discussed in Mishchenko *et al.*, 1999a): N(x) is the number of particles of radius x. The values of x_{g1}, x_{g2}, $(\ln^2\sigma_{g1})$, $(\ln^2\sigma_{g2})$, and α are parameters that were fitted to the measured distribution, and were used along with the minimum and maximum particle radius as inputs for the Mie code. The Mie code normalizes the size distribution via the constant C_1 such that (Mishchenko *et al.,* 1999a, eq. 25):

$$\int_{x_{min}}^{x_{max}} N(x)dx = 1. \tag{30}$$

Regardless of the code used for calculation of Mie scattering parameters, a necessary input is the complex index of refraction (m) of the material in question:

$$m(\lambda) = n(\lambda) + ik(\lambda) \tag{31}$$

where the real portion (n) and the imaginary portion (k) are referred to as the "optical constants" of a material. The dependence on wavelength is often left out in notation, but is of vital importance to the nature of the interaction of light and matter; it is because of this variation that the principle of spectroscopy exists, and why objects have different colors (rather than just varying shades of grey). The optical constants of crystalline materials are not easy to calculate, and have been determined only for a few materials in a few select wavelength regions; because of the dependence on wavelength, it is not possible to simply extrapolate from one region to another. For this study, optical constants were required for three substances, only one of which had been rigorously studied in the visible portion of the spectrum — the optical constants for the iron oxides (assumed to be hematite, based on XRD results) used were those of Goetz (2002). Published values of the imaginary part of the refractive index were not available in the visible part of the spectrum for aluminum oxide or calcium carbonate (values published by Querry *et al.*,

1978 were obtained from limestone samples with very low albedos, which are not consistent with those observed in these samples). Instead, published values of the real part of the refractive index (taken from Gervais, 1991 for Al_2O_3 at 0.635 μm, and from Deer *et al.*, 1992 for $CaCO_3$) were used. To estimate the imaginary portion, the value of k was varied until the albedo calculated for the largest peak particle size distribution by the Mie code matched that measured in the lab. This result was used to calculate scattering parameters for the remaining samples. Optical constants used in Mie calculations are tabulated in Table 2.

These theoretical calculations produce values for a number of output variables. The important results, for comparison with earlier model fits, are the single scattering albedo, the average extinction and scattering cross sections per particle (C_{ext} and C_{sca}), the average cosine of the scattering angle (<cosθ>), the average geometric cross section per particle (<σ>) and the average volume per particle (<v>). These parameters are determined from the size distribution and the extinction and scattering efficiencies:

$$\begin{aligned}
\langle \sigma \rangle &= \frac{\int N(x)A(x)dx}{\int N(x)dx} = \frac{\pi \int N(x)x^2 dx}{\int N(x)dx} \\
\langle v \rangle &= \frac{\int N(x)V(x)dx}{\int N(x)dx} = \frac{4/3\pi \int N(x)x^3 dx}{\int N(x)dx} \\
C_{ext} &= \frac{\int N(x)Q_E(x)A(x)dx}{\int N(x)dx} \equiv \langle \sigma \rangle \langle Q_E \rangle \\
C_{sca} &= \frac{\int N(x)Q_S(x)A(x)dx}{\int N(x)dx} \equiv \langle \sigma \rangle \langle Q_S \rangle
\end{aligned} \tag{32}$$

where A(x) is the cross section of a particle with radius x (=πx^2 for a sphere), V(x) is the volume of a particle with radius x (=4/3πx^3 for a sphere), N is the number of particles per unit volume with radius x, <Q_E> is the mean extinction efficiency, and <Q_S> is the mean scattering efficiency. These geometric terms are used to transform the average extinction and scattering

cross sections into the scattering and extinction coefficients expected in laboratory experiments. The relationship between the cross sections and the extinction and scattering coefficients is a bit more complex. For well separated particles, the definition for the extinction coefficient can be determined as (Hapke, 1993, p. 172):

$$\begin{aligned} E &= \int N(x)A(x)Q_E(x)dx \\ &= C_{ext}\int N(x)dx \\ &= \frac{C_{ext}}{\langle v\rangle}\int N(x)V(x)dx \\ &= \frac{C_{ext}}{\langle v\rangle}\frac{\rho_B}{\rho_S} = \frac{C_{ext}}{\langle v\rangle}\phi = \frac{\langle\pi\rangle\langle Q_E\rangle}{\langle v\rangle}\phi \end{aligned} \tag{33}$$

(and similarly for the scattering coefficient) where ϕ is the filling factor, and is the ratio of the bulk density (ρ_B) of the sample to the solid density (ρ_S).

$$\begin{aligned} \rho_B &= \int N(x)V(x)\rho_S dx \\ \frac{\rho_B}{\rho_S} &= \int N(x)V(x)dx \\ \phi &= \frac{\rho_B}{\rho_S} = \langle v\rangle\int N(x)dx \end{aligned} \tag{34}$$

Bulk densities were measured by weighing a known volume of each sample, and solid densities were taken from the values of the specific gravity for the appropriate minerals in Deer *et al.* (1992). The quantity (1-ϕ) is the porosity, and describes the fraction of void space available in the sample. While equation (33) is valid for well separated scatterers, it is necessary to multiply by an additional factor (F) to this definition when dealing with closely-spaced scatterers (Hapke, 1993, p. 169):

$$F = -\frac{\ln(1-\phi)}{\phi}. \tag{35}$$

Applying this additional term to equation (33) gives a more general definition for the extinction and scattering coefficients:

$$E = F\rho\frac{C_{ext}}{\langle v\rangle} = -\ln(1-\rho)\frac{C_{ext}}{\langle v\rangle} = -\ln(1-\rho)\frac{\langle\rho\rangle\langle Q_e\rangle}{\langle v\rangle}$$
$$S = F\rho\frac{C_{sca}}{\langle v\rangle} = -\ln(1-\rho)\frac{C_{sca}}{\langle v\rangle} = -\ln(1-\rho)\frac{\langle\rho\rangle\langle Q_s\rangle}{\langle v\rangle} \quad (36)$$

Once values for S and <cosθ> are determined, they can be used to calculate the transport mean free path. These final transformations allow for direct comparison of scattering parameters determined by both model fits and theoretical predictions. Results are shown plotted versus model fit parameters in Figure 19.

Error Estimates

Determination of error in the model fit scattering parameters were determined by first estimating the error in the parameters that were directly determined from model fits to the data (coefficients of p(g), w, and h_c). Beginning with the best fit results, each parameter was increased and decreased incrementally until the fit was deemed unacceptable. When varying the parameters to determine the error, the parameters were also constrained by physical meaning: the albedo cannot be greater than 1, and the single scattering function cannot be negative in the phase range 0-180°. The magnitude of the change in each direction is given as the error for that parameter. This error was then carried through scattering parameter calculations to determine error for those parameters as well, using the general error propagation formula:

$$\Delta V = \sqrt{\left(\frac{\partial V}{\partial x}\right)^2 \Delta x^2 + \left(\frac{\partial V}{\partial y}\right)^2 \Delta y^2} \quad (37)$$

described by Beers (1957, p. 29). This equation determines the error in a calculated result (ΔV)

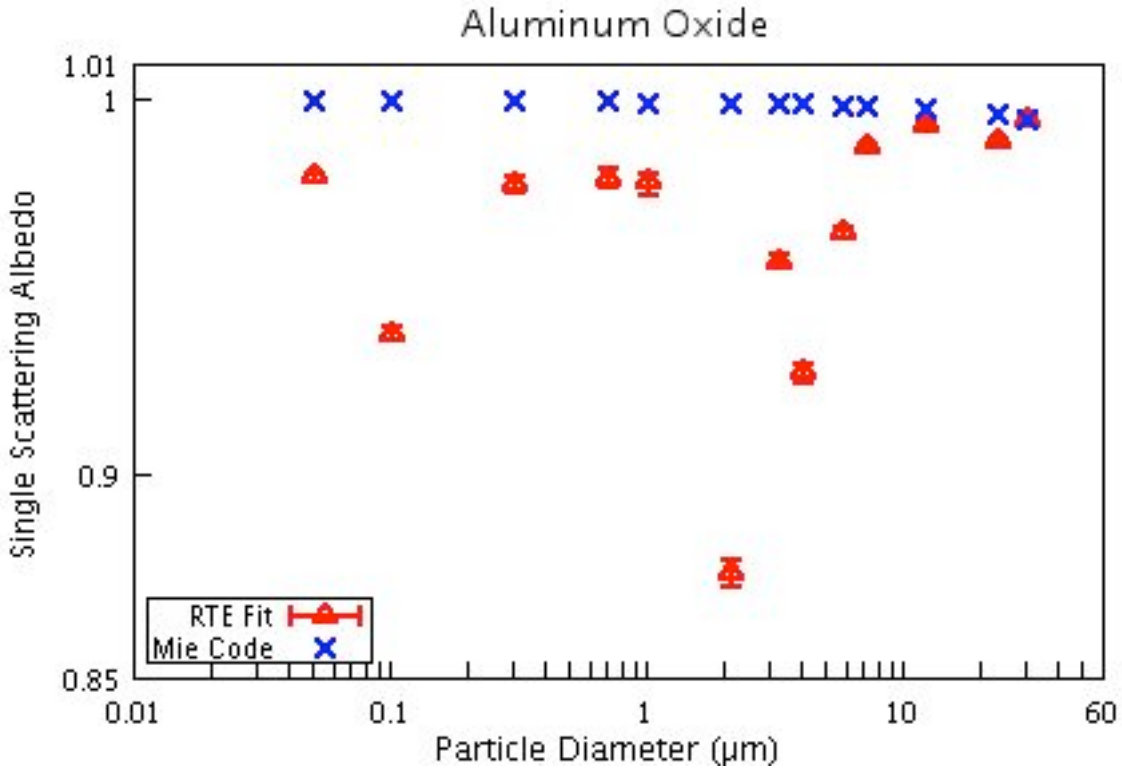

Figure 19a: Comparison of model fit parameters and Mie codes results, using estimated size distributions. Axes are log scale unless otherwise noted. Y-error bars on model fits were determined using error estimates described in the text. Above figure shows results for single scattering albedo for the aluminum oxide samples.

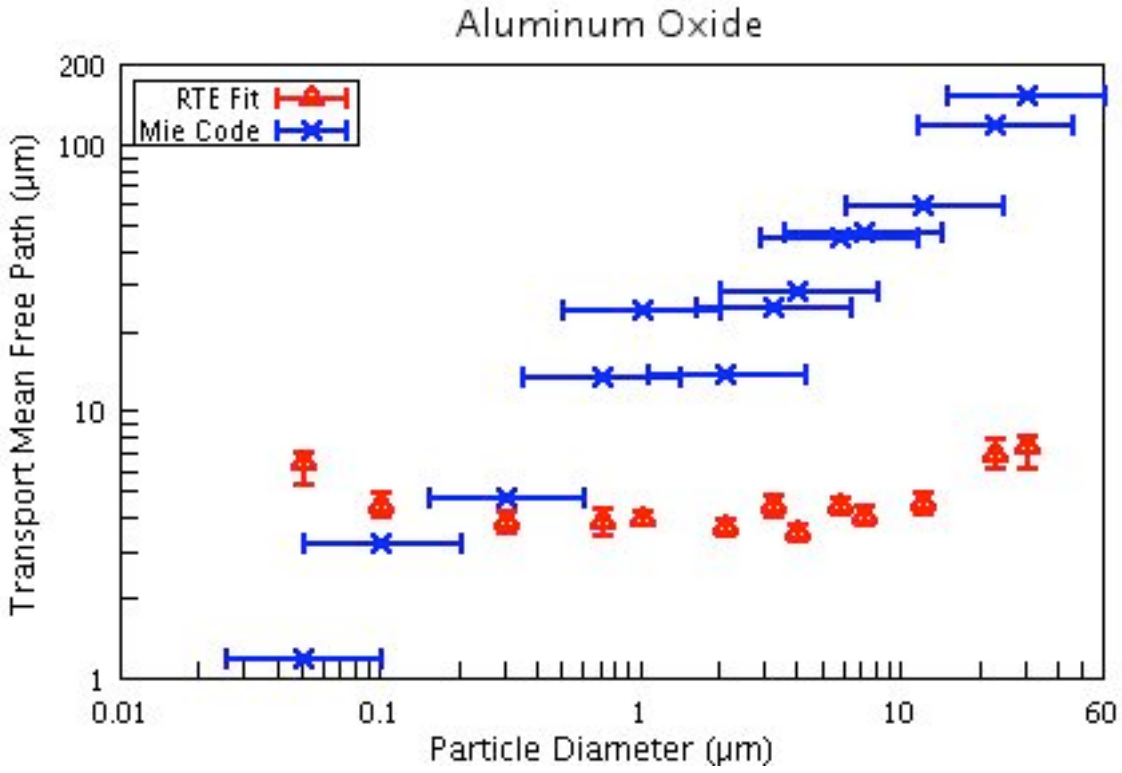

Figure 19b: Transport mean free path results for aluminum oxide samples. X-error bars on the Mie results show the half-power points of the size distributions used.

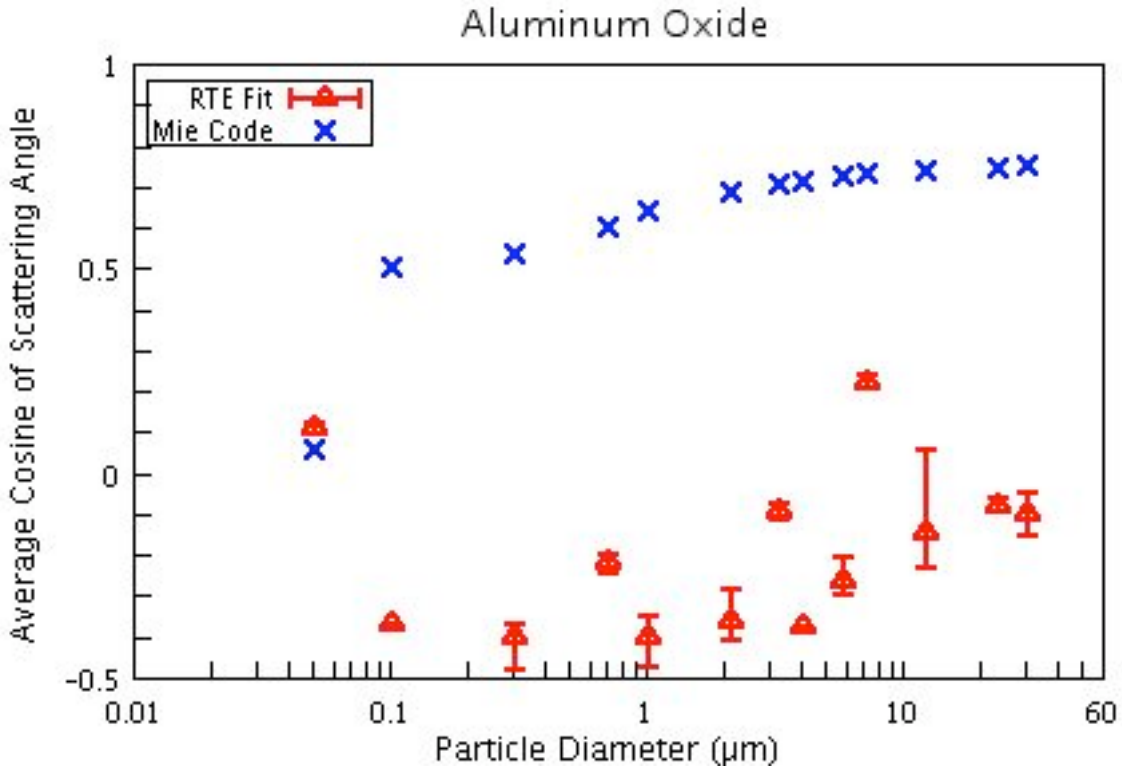

Figure 19c: Average cosine of the scattering angles results for aluminum oxide samples. The x-axis is plotted on a log scale, the y-axis on a linear scale.

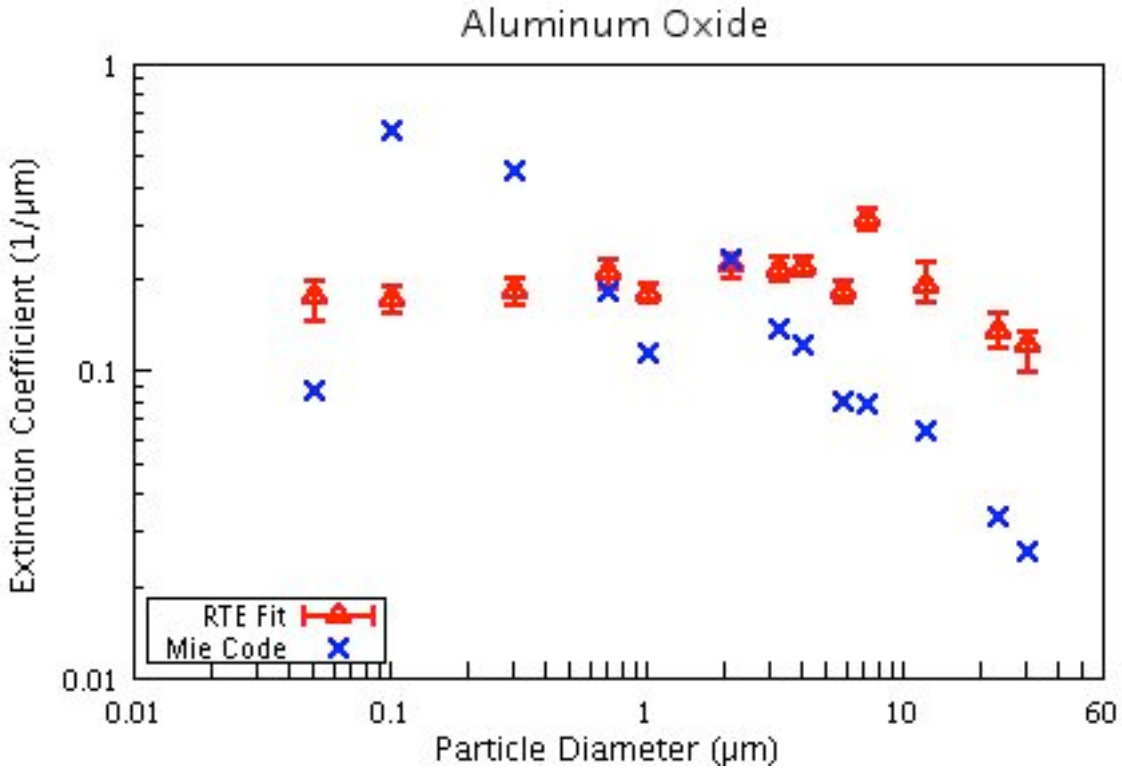

Figure 19d: Extinction coefficient results for aluminum oxide samples.

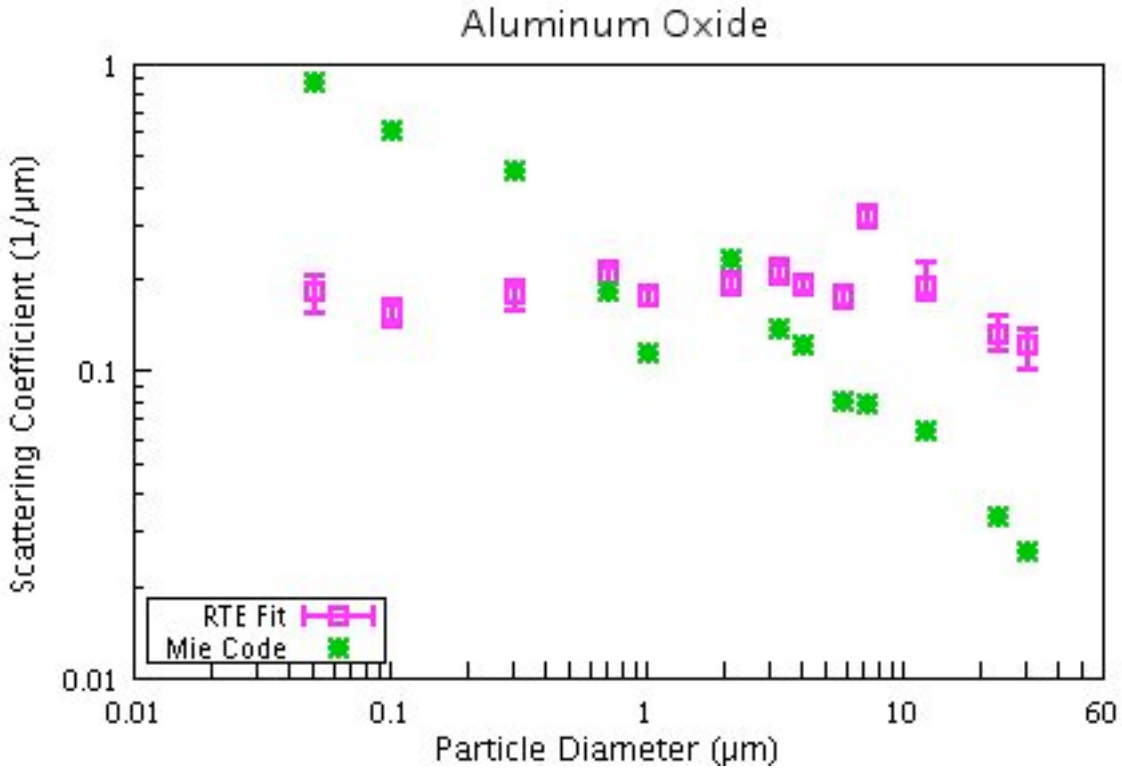

Figure 19e: Scattering coefficient results for aluminum oxide samples.

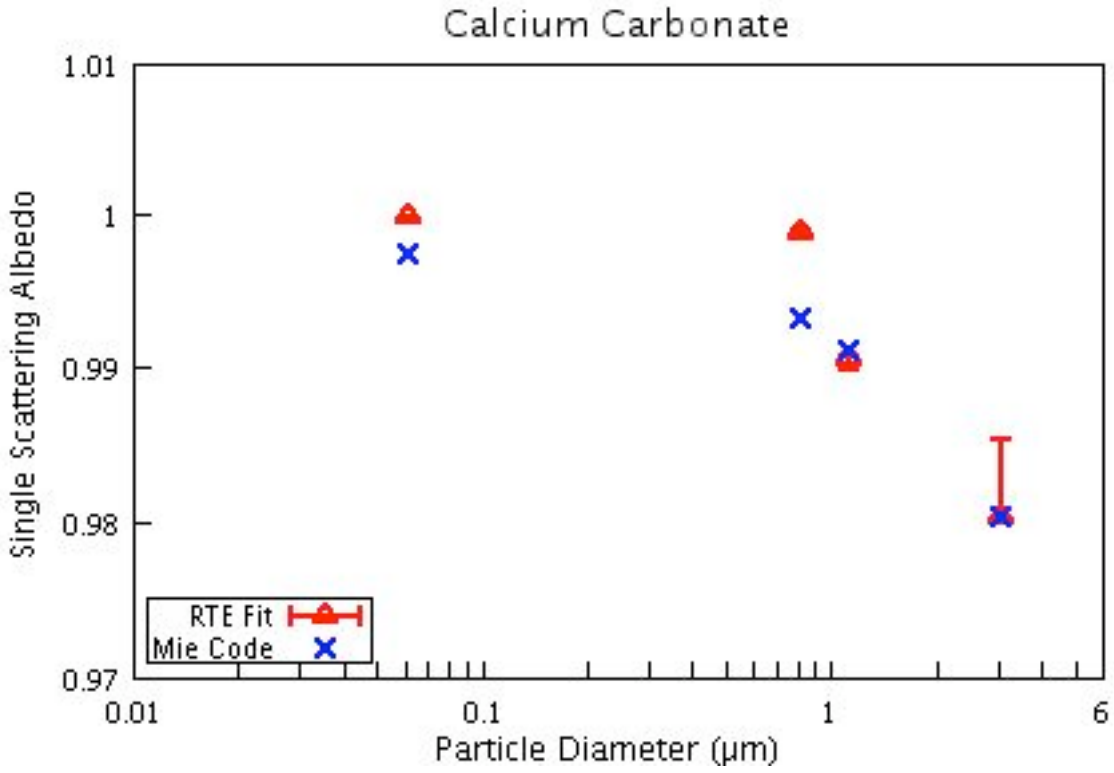

Figure 19f: Single scattering albedo results for calcium carbonate samples.

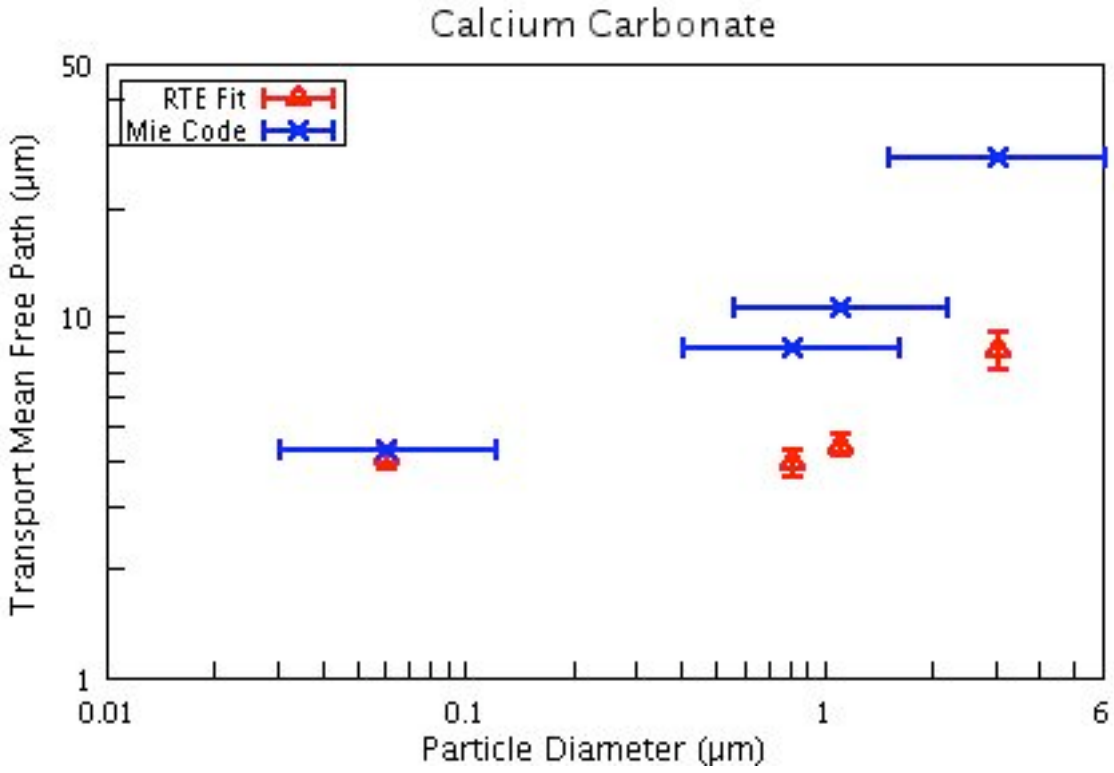

Figure 19g: Transport mean free path results for calcium carbonate samples. X-error bars on the Mie results show the half-power points of the size distributions used.

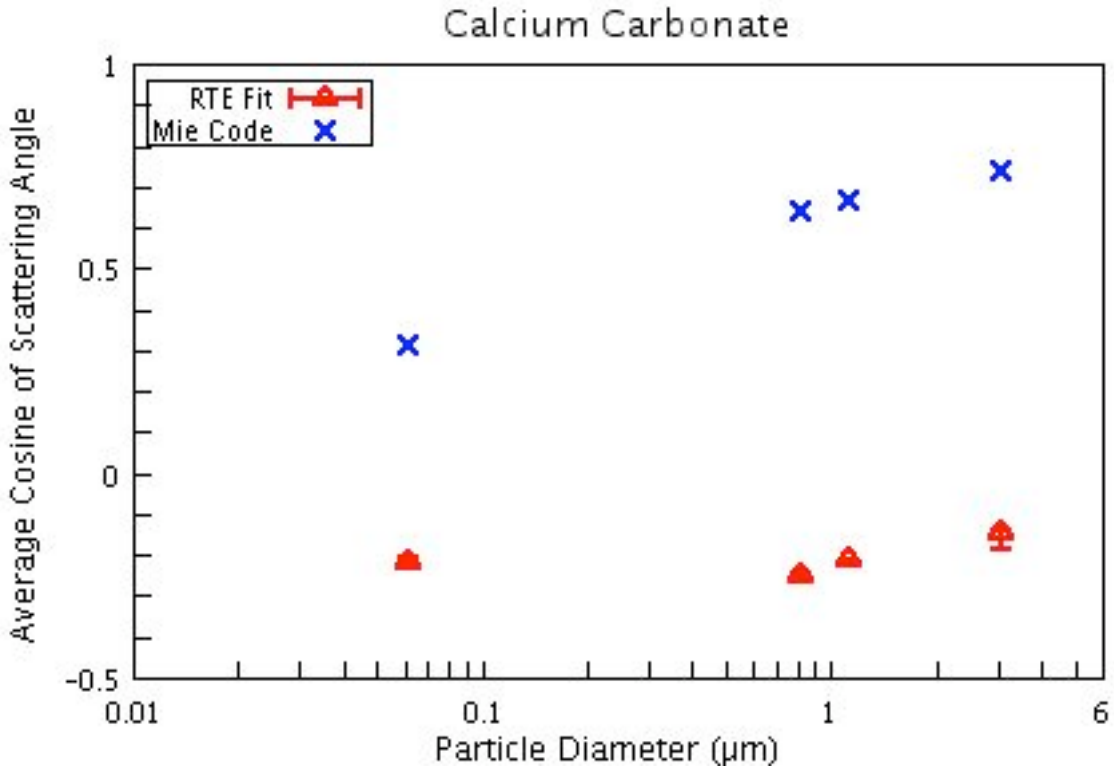

Figure 19h: Average cosine of the scattering angles results for calcium carbonate samples. The x-axis is plotted on a log scale, the y-axis on a linear scale.

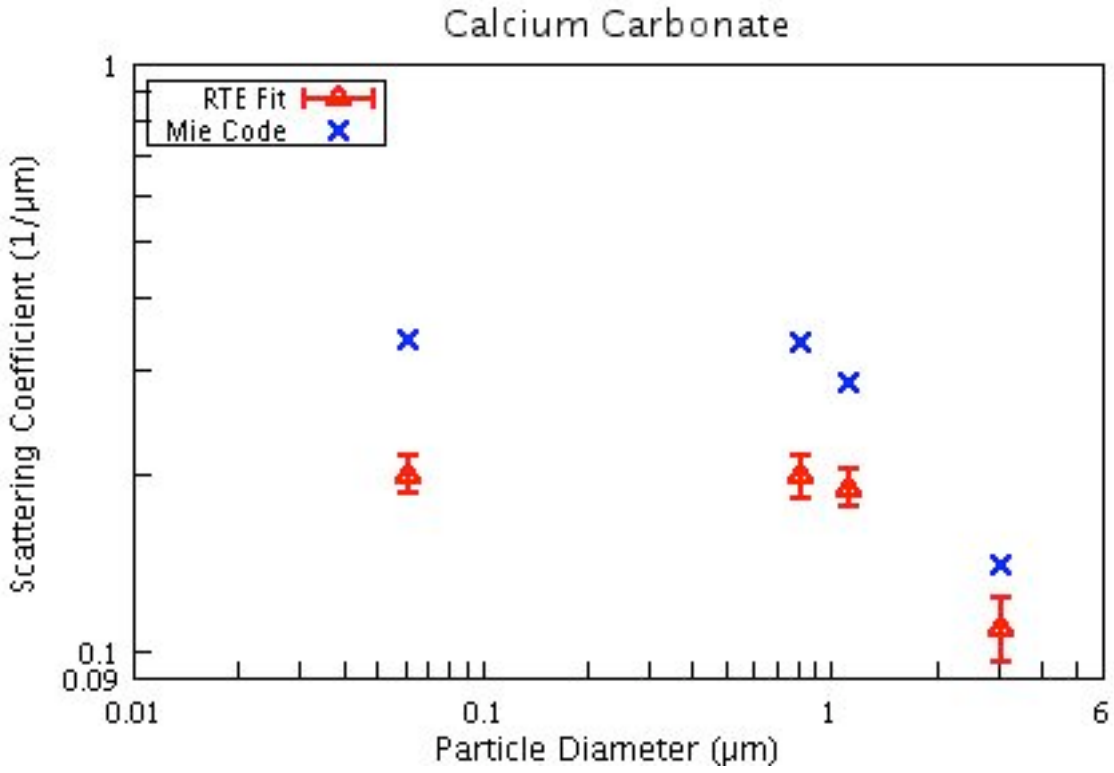

Figure 19i: Extinction coefficient results for calcium carbonate samples.

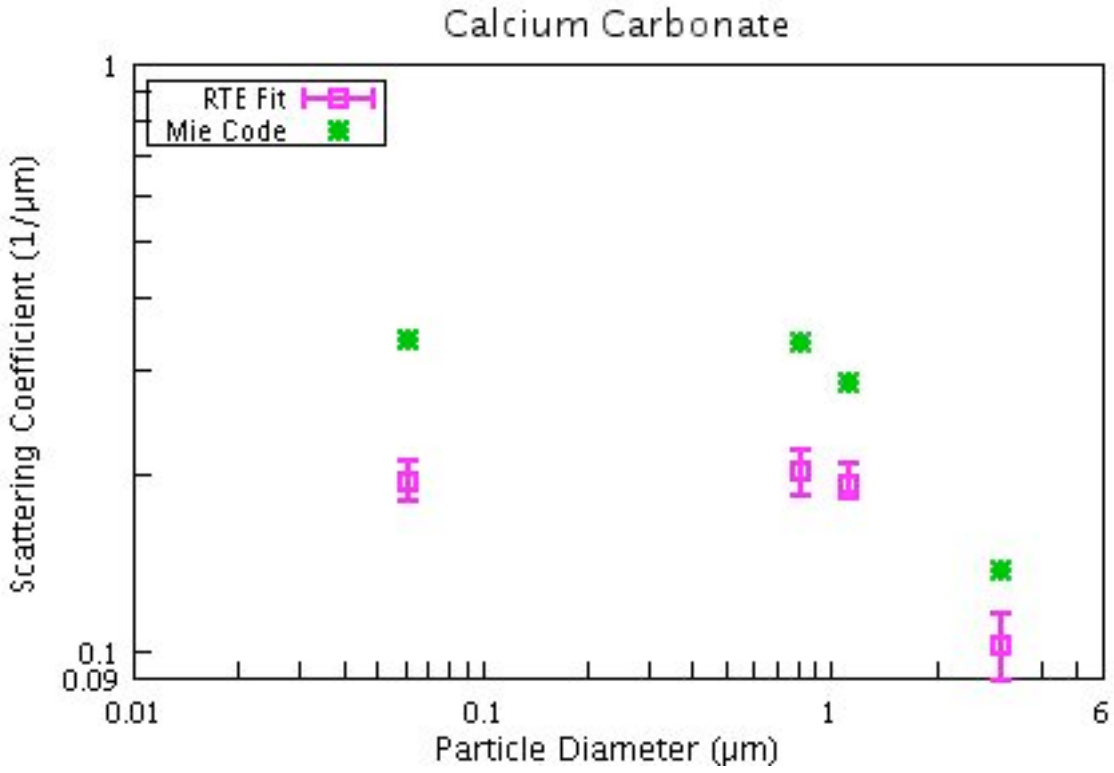

Figure 19j: Scattering coefficient results for calcium carbonate samples.

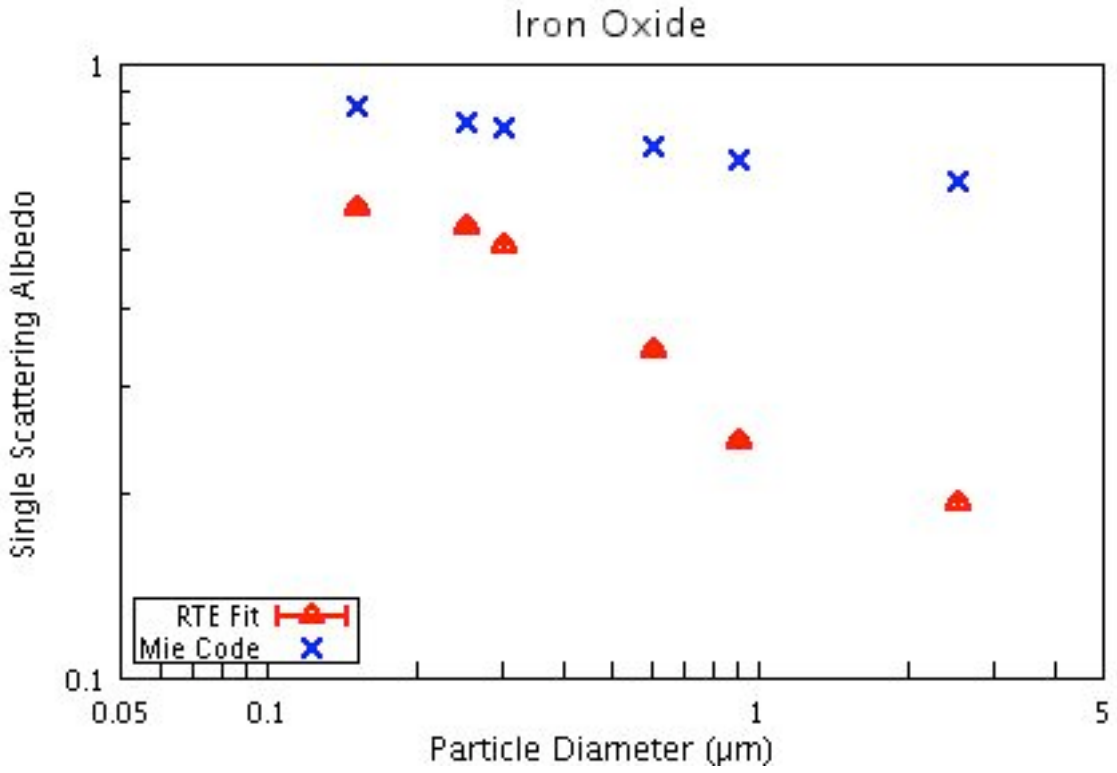

Figure 19k: Single scattering albedo results for iron oxide samples.

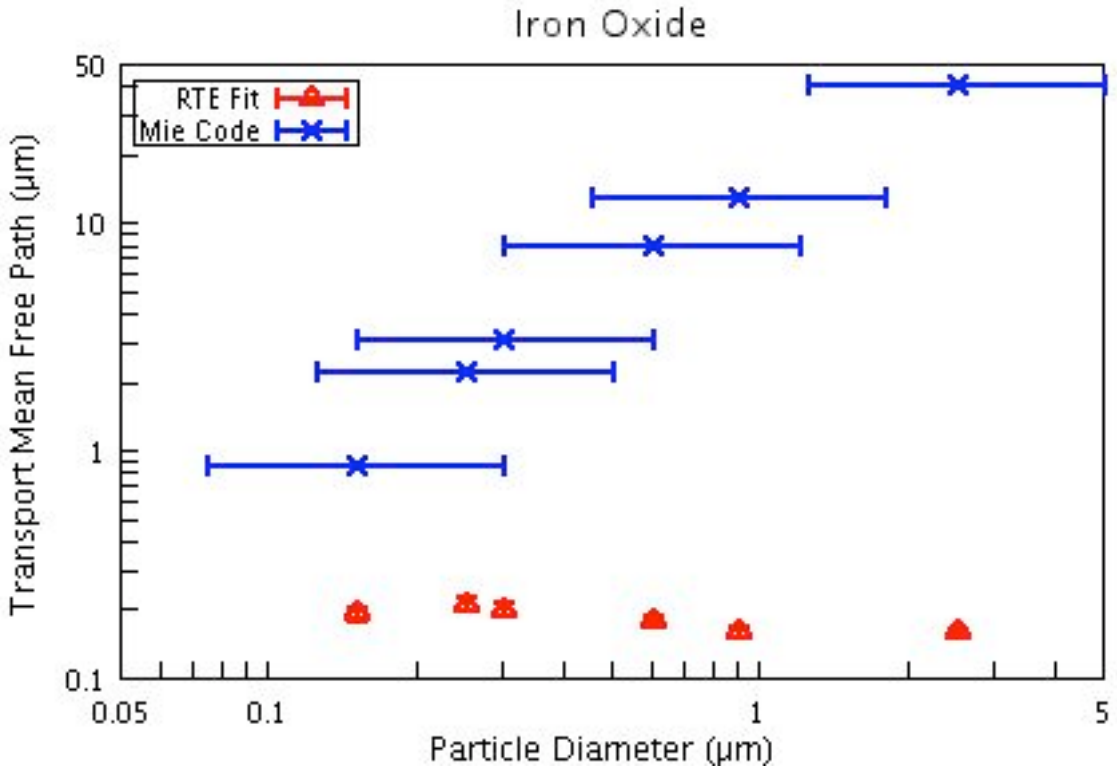

Figure 19l: Transport mean free path results for iron oxide samples. X-error bars on the Mie results show the half-power points of the size distributions used.

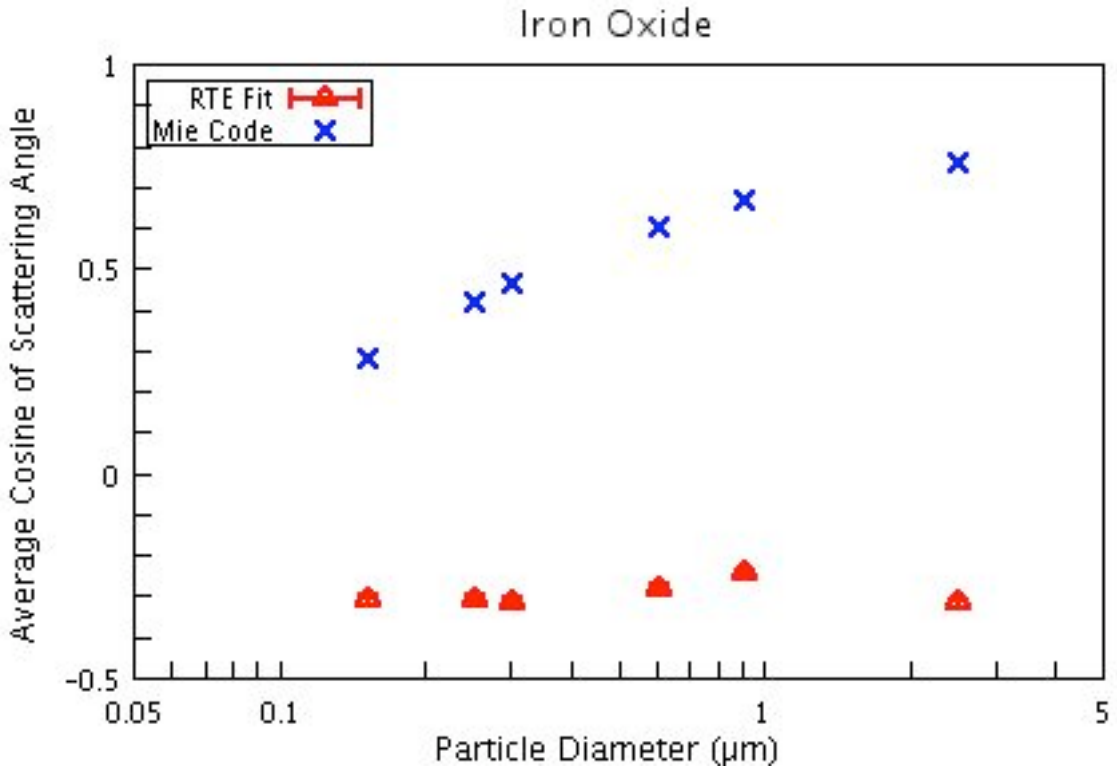

Figure 19m: Average cosine of the scattering angles results for iron oxide samples. The x-axis is plotted on a log scale, the y-axis on a linear scale.

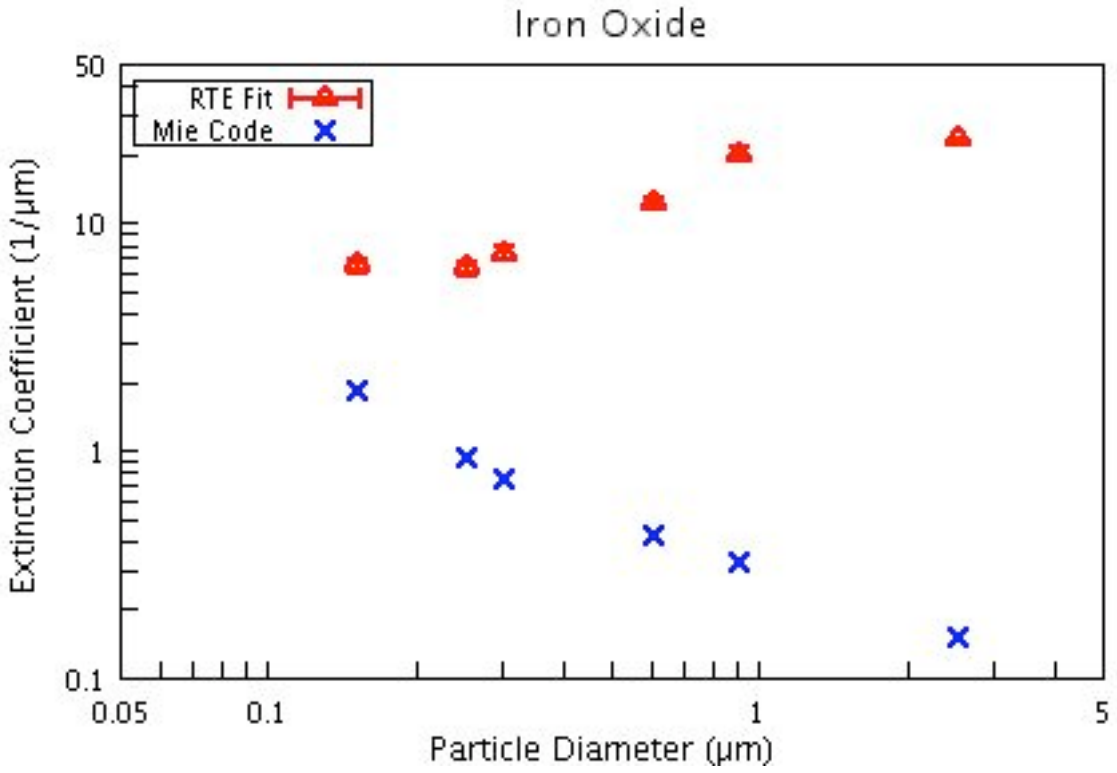

Figure 19n: Extinction coefficient results for iron oxide samples.

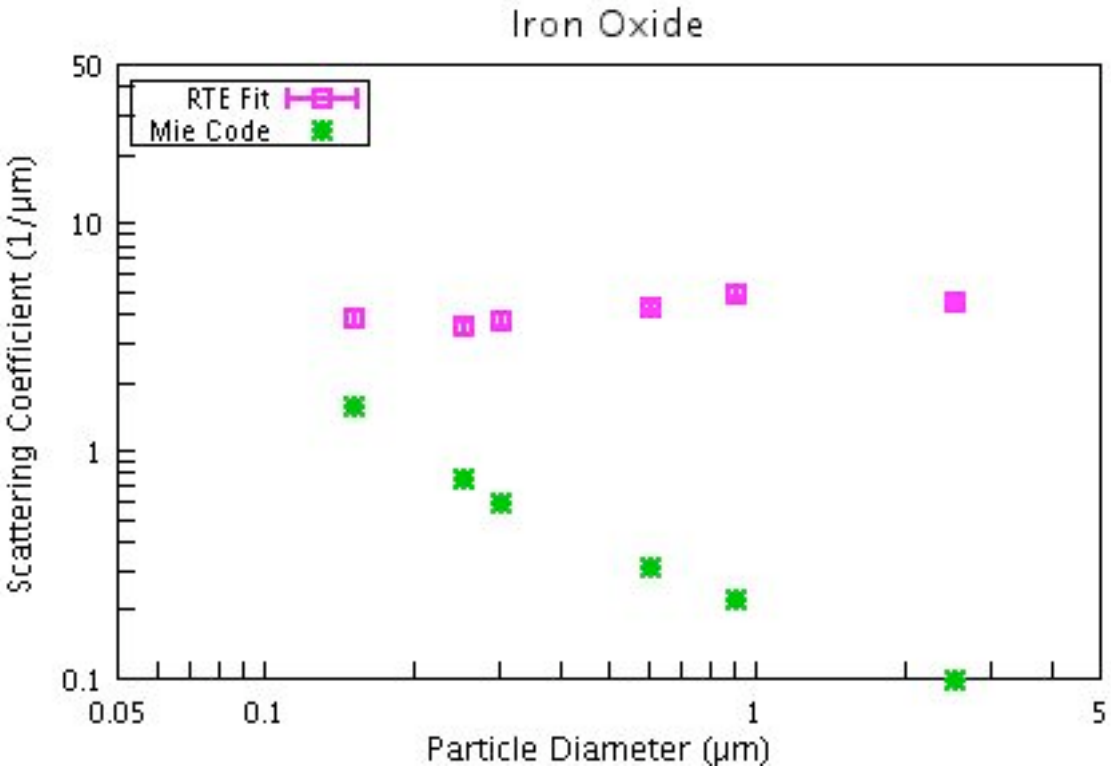

Figure 19o: Scattering coefficient results for iron oxide samples.

due to independent errors in the variables used to determine V (Δx and Δy). The formula is easily modified for additional variables (or reduced to a single variable) by adding/removing an appropriate term.

Errors for fit parameters taken directly from model fits (by modifying the parameter until an unacceptable fit was obtained) can be a bit misleading. While large errors may indicate a noisy set of data, they may also indicate that the parameter in question is not well constrained, and can vary a great deal before a noticeable change in the fit occurs. Alternatively, small errors may suggest a very well constrained fit, they may reflect a mediocre fit that quickly becomes unacceptable, or they may reflect a parameter that was very close to physical impossibility (especially when examining the parameters of the single scattering function). Regardless, the errors calculated from the parameter fits as well as those determined by propagation are all relatively small: the plots shown in Figure 19 all have y-axis error bars for the fit parameters, and many are indistinguishable from the points used to mark the data values.

Errors for the particle size were not true errors, considering the difficulty of determining the exact accuracy of the results. Instead, the error bars on particle size determinations represent the size distribution that used in the Mie code. The actual point itself lies on the peak of the size distribution, and the error bars extend to the half-power points. The half power points for all of the estimated size distributions occur at the same relative size to the peak (1/2 the peak for the lower half power point, 2 times the peak for the upper half power point): the distributions are similar above the half-power points, and differ only below them.

Discussion

Figures

Graphs of both model fit determined scattering parameters and calculated Mie theory predictions for those parameters appear in Figure 19. All plots, except for those involving <cos□>, are log-log: <cos□> plots are log along the x-axis only, so that negative values can be plotted along the y axis The x-error bars indicate the peak and half-power points of the estimated size distributions: these are the same for all parameters, but the error bars are omitted on most of the figures to avoid clutter. Y-error bars on model fit parameters are the result of error analysis discussed earlier.

Measured Scattering Parameters

The phase curves of each of these samples has provided a new insight into the scattering of light by particulate samples. The analysis of these curves has not provided the answers to the questions originally asked; instead, the results have provided a set of new questions and perhaps answers to some others that were not considered originally. The radiative transfer based model fits shown here represent very good fits to the laboratory datasets, and the error bars for each parameter suggest that while the fits are not unique, the parameters are relatively well-constrained. Clearly, the model used here (Hapke, 2002) is a good empirical representation of scattering from these samples, even for particles smaller than the wavelength. However, the relationship of the fit parameters to the physical properties of the sample remains to be determined.

An interesting note from the analysis of these curves is the inability to directly compare the long arm and short arm data. While test runs from the short arm goniometer at an incidence

angle of 0° can be combined with long arm data (same incidence) with no issue, this is not the case when the incidence angle is varied. Model fits to i=60° short arm data do not often produce scattering parameters that fit the long arm data of the same sample taken at i=0°; considering that the model fits should remove any effect of geometry on the sample, this is a puzzling result that suggests there may be limitations to the accuracy of the fits obtained, or to the scattering model used here when the incidence angle is not 0°. Possibly this is the result of surface roughness, which is not taken into account in either the model or the theoretical calculations. The effect of the unevenness of the surface is small when the incidence angle is small, but gets larger as the angle does. While this effect is not quantified in this study, the difference between the two instruments when measuring at different incidence angles is likely due to surface roughness. The difference between the long arm and short arm results is also one of the reasons that the long arm phase curve data was not fit with the full model equation (a simplified version was used), but the more important reason was the effect of the kinked fiberoptics on the curve itself. As discussed earlier, this (now-resolved) kink rendered the larger phase angles of this dataset (3° - 5°) unusable for model fits.

A remarkable result from the short arm phase curves is the extreme width of the coherent backscatter opposition surge for the iron oxide samples. While the aluminum oxides and calcium carbonates demonstrate a CBOE that is only a few degrees wide, the circular polarization ratios for the iron oxide short arm datasets suggest that the CBOE extends out to at least 40° phase. The model fits to this data suggest that the CBOE actually has an effect on the phase curve out to almost 80°. Converting the CBOE width terms for the iron oxides per equation (28) gives values of the HWHM ranging from 0.17 to 0.23 radians, or 9.75° - 13.2°. At first glance, these values may seem rather small, considering both the circular polarization data

and the model fits. This apparent discrepancy exists because the shape of the CBOE is not triangular, but has a long tail that extends to large phase angles. A more serious difficulty in interpreting the large width is that the relationship between the HWHM and the transport mean free path (L) given in equation (27), derived by van Albada et al. (1987) and used in the model of Hapke (2002), is probably not valid when the transport mean free path is less than the wavelength (van Albada et al., 1987; Akkermans et al., 1988). This is clearly the case for the iron oxides. The extinction and scattering coefficients derived from L for the iron oxide samples probably are similarly not valid. However, those scattering parameters that are not dependent on the transport mean free path (determined from the RTE model fits: w, p(g), and h_c) remain valid.

The plots of single scattering albedo versus particle size show some dependence on particle size; both the iron oxides and calcium carbonate data show decreasing albedos with increasing particle size. While this change is extremely small in the latter dataset, the error bars of the points do not overlap, suggesting that this is likely a real trend and not an artifact of noise. This trend was expected for the iron oxides; simple inspection of the samples shows a color change from a bright orange-red to a dull dark maroon as the particle size increases. Any other trend would have suggested an unreliable result. The aluminum oxides, however, are different; the five samples smaller than 2.1 μm have roughly similar albedos, while those larger than 2.1 μm have albedos that increase with increasing particle size. The 2.1 μm sample is anomalous with an albedo somewhat smaller than the other sizes. This lower albedo occurs where particle morphology observed in SEM images changes; hence, it is likely that the particle morphology is having some effect on the reflectivity of the sample.

The average cosine of the scattering angle (<cos□>) and the transport mean free path (L) both show very little dependence on particle size. Through the entire suite of samples, there are

only two that have slightly positive values of <cos□>; the aluminum oxides sized 0.05 and 7.1 μm. These are, therefore, the only two samples that show any evidence of being slightly forward scattering. The remaining samples are all slightly backscattering.

The lack of an appreciable size-dependence in the values of any of the parameters, especially the transport mean free path (L), observed here and in earlier studies (Nelson *et al.*, 2000; Hale *et al.* 2002, Nelson *et al.* 2002a and 200b) was so surprising that considerable care was taken to insure that this was not an instrumental effect. In order to do this, samples that are not expected to exhibit any opposition surge were measured using the long arm goniometer. Results for the rippled surface of a piece of welding glass and a sample of 2.5 μm glass microspheres are shown in Figure 20. The welding glass should exhibit only specular reflection, and hence should not have a coherent backscatter opposition surge. The glass spheres have smooth surfaces, and are very close together, making the transport mean free path very long. Any coherent backscatter surge from this material should be very narrow, and not visible even with the long arm goniometer. If an opposition surge were present in either the phase curve or the circular polarization ratios, this would indicate that this is an instrument effect and not a real phenomenon. The results clearly show, however, that this is <u>not</u> an instrumental effect; no coherent backscatter opposition surge is visible in these samples. The constant upward slope with decreasing phase angle observed in the glass microspheres is a result of the spheres' glories; there is no upturn visible in the circular polarization data, showing that there is no CBOE visible in the range of phase angles measured.

The extinction and scattering coefficients (E and S) for the aluminum oxides and calcium carbonates also show little dependence on particle size. This is not unexpected, considering the values of E and S depend on the parameters discussed above, which show no size dependence

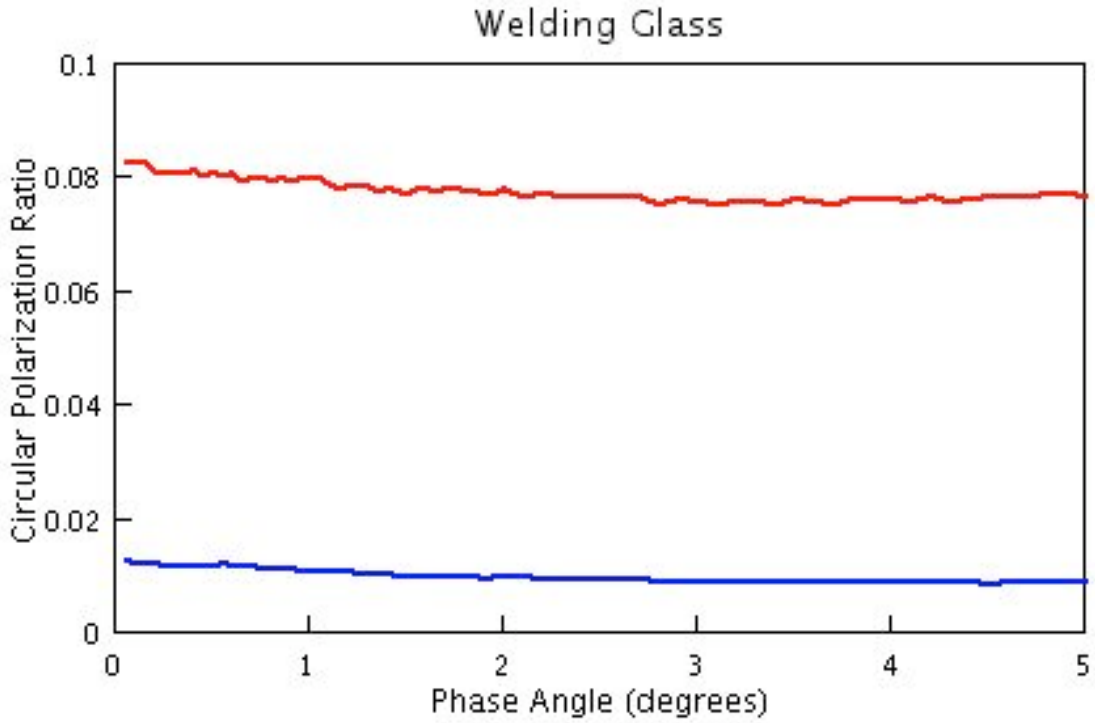

Figure 20a: Phase curve and circular polarization ratios for welding glass and 2.5 μm glass microspheres taken on the long arm goniometer. The welding glass data have been smoothed, the glass microsphere data have not. The welding glass data shown above includes circular polarization ratios for both senses of circularly polarized light.

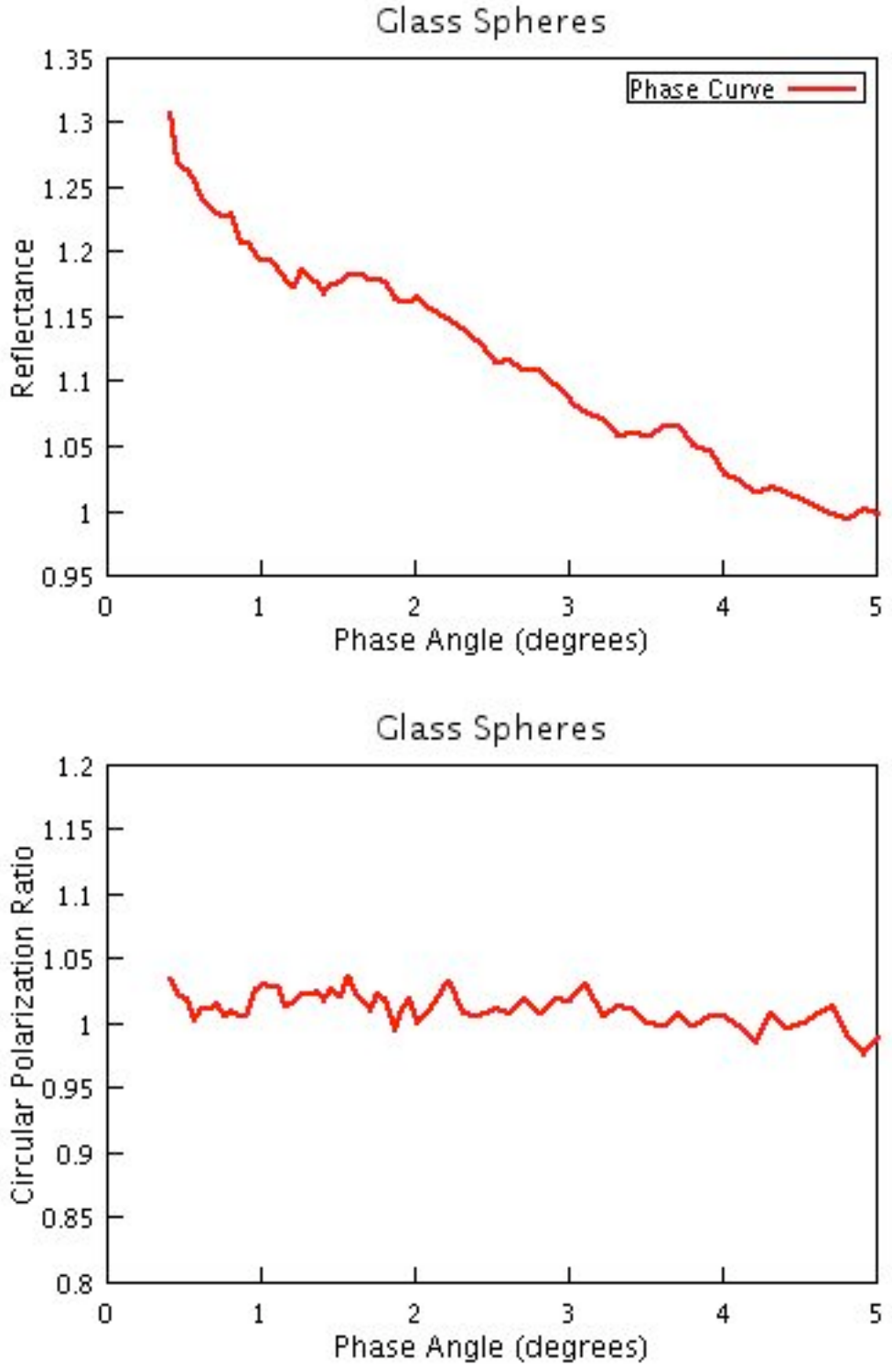

Figure 20b: Phase curve and circular polarization ratio data for 2.5 μm glass microspheres

either. The changes observed in the albedo of the aluminum oxides, however, does not appear in E or S; the value of these terms is relatively unchanged with changing particle size, except for a slight increase at the 7.1 μm particle size (which, coincidentally, is one of the two samples that exhibited forward scattering). The calcium carbonate values of E and S are also relatively similar, with a decrease only at the largest particle size.

Regardless of the scattering parameter discussed, there is no significant change in the behavior of the parameter as the particle size approaches the wavelength. Trends observed in the larger particle sizes continue to the smaller sizes with no abrupt change or deviation at the particle sizes nearest the size of the wavelength.

Predictions of Fundamental Particle Scattering Models

The predicted values of w show a slight decrease with increasing particle size, which is especially apparent in the calcium carbonates and the iron oxides. Conversely, the predicted values of the average cosine of the scattering angles <cos□> increase with increasing particle size for particles larger than the wavelength; particles smaller than the wavelength have lower values of <cos□>. All of the predicted values of <cos□> are positive, indicating the theory predicts that these samples should all be strongly forward scattering. Part of this is due to the inclusion of diffraction in the fundamental particle scattering theory, which does not exist for particles in contact (Hapke, 1999). However, even if diffraction were removed, <cos□> would remain positive.

For sizes greater than the wavelength, the extinction and scattering efficiencies (Q_E and Q_S) do not depend strongly on the particle size, so extinction and scattering coefficients (E and S)are inversely proportional to the size. For sizes less than the wavelength, Q_S and Q_E decrease strongly as the size decreases. Hence, predicted values of the transport mean free path show a

pronounced concave up trend for the high albedo samples corresponding to a concave down trend in the values of E and S. The corresponding highest/lowest points occur at a value near the wavelength of light. Because the iron oxide has a large imaginary refractive index, this trend does not appear in these samples, where the predicted values of the transport mean free path L increase slightly with increasing particle size while the values of E and S decrease.

Comparison of Model Fits and Theoretical Predictions

The datasets of laboratory measured phase curves for three sets of powders of known composition and particle size were compared with predictions of models that assume the particles are the fundamental scattering units. These phase curves include the small phase angles, where the effects of both the coherent backscatter and shadow hiding opposition surges are apparent, and larger phase angles, which are necessary for accurate derivation of scattering parameters. A number of interesting discrepancies between the experimental results and theoretical predictions were observed.

All of the opposition surges measured here, including both high and low albedo samples, are concave upward. The phase curve appears to continue to increase beyond the smallest angles measured, rather than rolling over and producing a rounded-off curve. Laboratory measurements of suspensions of well-separated latex microspheres and theoretical predictions have suggested that only non-absorbing materials should have such peaked phase curves while absorbing media should exhibit truncated, rounded opposition surges (Etemad *et al.*, 1987; van der Mark *et al.*, 1988; Wolf *et al.* 1988). The observed sharp peaks require that a large number of the multiply-scattering photons have entrance and exit points that are separated by several mean free paths, which is quite likely in a natural surface that exhibits a large amount of surface roughness on the scale of a mean free path.

Neither the values nor the trends observed in parameters derived from model fits and those predicted by fundamental particle scattering theory agree, as shown in Figure 19. While in some cases the parameters may have similar values for a single particle size, more often the values are significantly different from each other. Observed decreases in single scattering albedo model fits with increasing size are of a much larger magnitude than are predicted by Mie theory.

The signs of the predicted and observed average cosines of the scattering angles (<cos□>) are nearly all opposite, and the absolute magnitudes of the predicted values are 2-3 times larger than that of the model fits. The values of <cos□> show the samples are nearly all weakly to moderately backscattering. This is completely contrary to theoretical predictions based on the fundamental particle scattering assumption applied to spheres that regolith particles should be strongly forward scattering (Mishchenko, 1994).

The variations of the transport mean free path (L), the extinction coefficient (E), and the scattering coefficient (S) with particle size are in complete contrast to the theoretical predictions based on the assumption of fundamental particle scattering. Clearly, fundamental particle scattering theory fails to accurately predict the scattering parameters observed in laboratory samples. These powders are not good examples of fundamental particle scatterers, even when the particle size is much larger than the wavelength. The dependence of L on particle size is particularly surprising. Intuitively, one expects that L should be of the order of the particle size; this is predicted by fundamental particle scattering models based on Mie theory (Mishchenko, 1992b; Mishchenko and Dlugach, 1993; Mishchenko, 1993a), and is supported by measurements on suspensions of well separated latex spheres (Kuga and Ishimaru, 1984; van Albada and Lagendijk, 1985 and 1987; Wolf *et al.,* 1988). Our results show that this is not the case for complex particles in contact. However, they are clearly in agreement with previously published

results (i.e. Nelson *et al.*, 2000; Hale *et al.*, 2002; Nelson *et al.*, 2002a) suggesting that the width of the CBOE — and therefore the value of the transport mean free path — has little dependence on particle size. This is true regardless of particle albedo as well, whether the measured CBOE width is for the darker iron oxides and the brighter aluminum oxides presented here, or the extremely dark boron carbides reported in Nelson (2002).

The small values of the transport mean free path (L) explain why predictions of fundamental scattering models that large regolith particles should be strongly forward scattering (c.f. Mishchenko, 1994) are not correct because the particles are not the scattering units. A result of this conclusion is that the commonly used relationship (equation (4)) between the extinction coefficient (E), the scattering coefficient (S), and L and the extinction and scattering efficiencies given earlier is not valid in the case of closely-packed media. On the other hand, scattering models based on this assumption have had success in quantitatively predicting absorption coefficients from bidirectional reflectance measurements (Hapke and Wells, 1986). At present it is not clear what should be used in place of these relations to calculate E, S (i.e. equation (4)), and the single scattering function p(g).

An interesting result is the way that the observed scattering and extinction coefficients (E and S) change to accommodate changes in the single scattering albedo w. It is commonly assumed in fundamental large particle scattering theories that the value of E remains approximately constant, while the values of S and the absorption coefficient (K) vary to cause the value of the single scattering albedo (w) to change. The model results here, however, suggest that S remains constant, and that the variations in w are related to variations in E. Given that S and E are related by the absorption coefficient K ($E = S + K$), if S remains constant, E changes with K. Observed decreases in single scattering albedo with increasing particle size are due to

increased absorption with increasing particle size. This is consistent with the results of spectral analysis of powders of different sizes that show a decrease in the depth of absorption bands with decreases in particle size (i.e. Conel, 1969; Salisbury *et al.*, 1987; Moersch and Christensen, 1995; Mustard and Hays, 1997; Cooper and Mustard, 1999).

The results described above clearly indicate that there is a discrepancy between theories based on fundamental particle scattering and reflectances measured in the laboratory. The most striking result is the lack of a strong dependence of the measured scattering parameters (except for the single scattering albedo w) on particle size. This observation suggests that our understanding of the basic interaction of a light beam with the surface of a complex medium, like a particulate sample, is not well understood. It appears, at least from the results measured here, that the light is interacting with scattering units that are on the order of a few wavelengths in size. For particles that are smaller than the wavelength, the individual particles do not scatter independently, but instead interact coherently and appear as wavelength-sized clumps to the incoming light. For particles that are similar in size to the wavelength, the particles themselves may act as scattering units. This is consistent with results presented here, where the best agreement between the theoretical predictions and laboratory measurements often occurs at particle sizes near the wavelength. For particles much larger than the wavelength, wavelength scale surface facets, cracks, and protrusions act as scattering units rather than the entire particle itself. This interpretation can explain why the single scattering function p(g) is backscattering and not forward scattering: the forward scattering prediction is based on calculations for smooth-surfaced isolated spheres, not rough-surfaced irregular particles in contact.

Media of complex particles such as the powders studied here (or the regolith of a solar system body) do not behave as collections of smooth spheres that scatter independently of each

other. Instead, we suggest that the waves propagating through these media are most strongly influenced by wavelength-scale inhomogeneities, which act as the scattering units expected by radiative transfer theory. This conclusion is supported by the ability of RTE-based models to produce good empirical fits to reflectances measured from particulate samples, where an fundamental sphere scattering model such as Mie theory does not accurately reproduce the measured scattering parameters. These wavelength sized scattering units may be surface facets or protrusions, subsurface cracks, the particle itself, or an agglomerate of smaller particles. Regardless, this monotony in the size of the scattering unit suggests that the transport mean free path will be the same for powders of different particle sizes, and that the value will be proportional to the wavelength. This conclusion predicts (although this prediction was not studied here) that the HWHM should not vary with wavelength if the transport mean free path L is proportional to wavelength. This hypothesis is consistent with measurements made here and elsewhere that the HWHM of the coherent backscatter opposition surge varies only weakly with particle size (i.e. Nelson *et al*., 2000; Hale *et al*., 2002; Nelson *et al*., 2002a), and wavelength (Nelson *et al*., 2002b, Hapke *et al*. 1998).

Conclusions

This project was originally intended to examine experimentally the changes in particle scattering as the size of the particle approached the wavelength of the scattered light. The results showed little change in modeled scattering parameters as the particle size decreased, aside from an expected increase in albedo due to decreased absorption. Specifically, the questions that were intended to be addressed were the following: (1) How well do radiative transfer based scattering models describe the scattering of light by media with particle sizes equal to or smaller than the wavelength? (2) Can models and relationships based on the fundamental particle scattering assumption be reliably applied to data from planetary regoliths and regolith analogs? (3) If the fundamental particle scattering assumption is not valid, then what is the physical meaning of parameters determined from radiative transfer based models? (4) Can physical properties be determined from similar laboratory measurements and photometric remote sensing data?

The answers to the first and second questions are addressed in the model fits and parameter comparisons. The radiative transfer based model of Hapke (2002) provided a good empirical fit to all the data acquired in this study, regardless of the particle size. Clearly, this model is useful for describing and parameterizing data from media of large particles, and media made up of particles equivalent to, or smaller than the wavelength. Second, the results from the model fits do not agree with the theoretical predictions of a fundamental particle scattering theory. These results suggest that this assumption, and models and relationships based on it, are inadequate to model planetary regoliths. The third and fourth questions remain unaddressed here. These questions raise important issues, since the end result of this photometric modeling should be to determine certain physical properties of a planetary surface remotely. Future work

in this area should provide more insights, by including additional materials and expanding the work to additional wavelengths and geometries.

The important result of this study is the disagreement between results of the assumption of fundamental particle scattering and the modeled parameters. While exact agreement is not expected because the SEM analysis shows that our particles are not the spheres assumed by theory, it is clear that the theoretical predictions of the Mie code calculations poorly represent the scattering parameters derived from fits of a radiative-transfer based model to the laboratory results. The magnitudes of the observed changes in albedo are not predicted; the particles are expected to be strongly forward scattering when in fact they are symmetric or backscattering. Predicted changes in the scattering and extinction coefficients, as well as the transport mean free path with particle size are not observed. The predicted quantities tend to have curved character changes at particle sizes near the wavelength, but the observed values are nearly constant in value for these three parameters regardless of particle size. When the albedo decreases due to increased particle size, the scattering coefficient S remains constant while the extinction coefficient E and the absorption coefficient K increase, rather than E remaining constant while S decreases, as predicted by theory.

Interpretation of the measured laboratory results suggests that particulate media may behave as scattering units on the order of the wavelength in size, regardless of the actual particle size. These units may represent surface irregularities, particle clumps, or individual particles. The hypothesis given here is that this results in a transport mean free path that is nearly invariant with particle size, and is proportional to the wavelength. This would suggest that the half-width at half-maximum of the coherent backscatter opposition surge should only vary weakly with either particle size or wavelength.

It is clear from the comparison described here that the results of fundamental particle scattering theory cannot be applied to materials consisting of closely packed scatterers. While those theories are valid for situations such as aerosols or clouds in planetary atmospheres, their results and assumptions should be applied only with great caution to the study of planetary surfaces covered by regoliths.

Appendices

Appendix A

Representative SEM images from each composition used. Aluminum oxide and iron oxide images were taken at the University of Pittsburgh courtesy of the Materials Science department, and each image contains a notation of the magnification as well as a scale bar. Calcium carbonate images were acquired during automated particle size runs at R.J. Lee Group (Murraysville, PA). The calcium carbonate images do not contain scale bars: the figure caption instead lists the measured average diameter of the particle in each image.

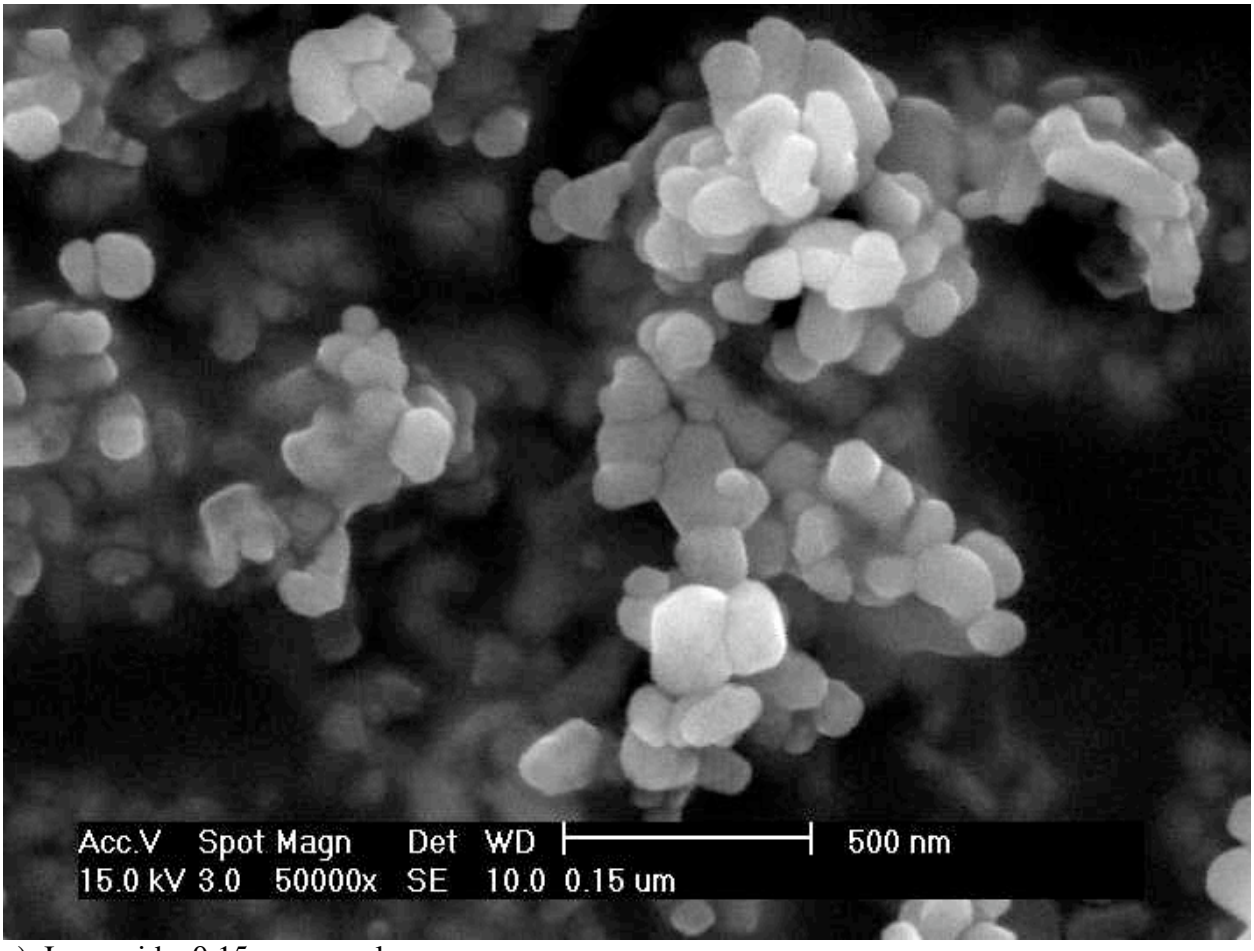

a) Iron oxide, 0.15 μm sample

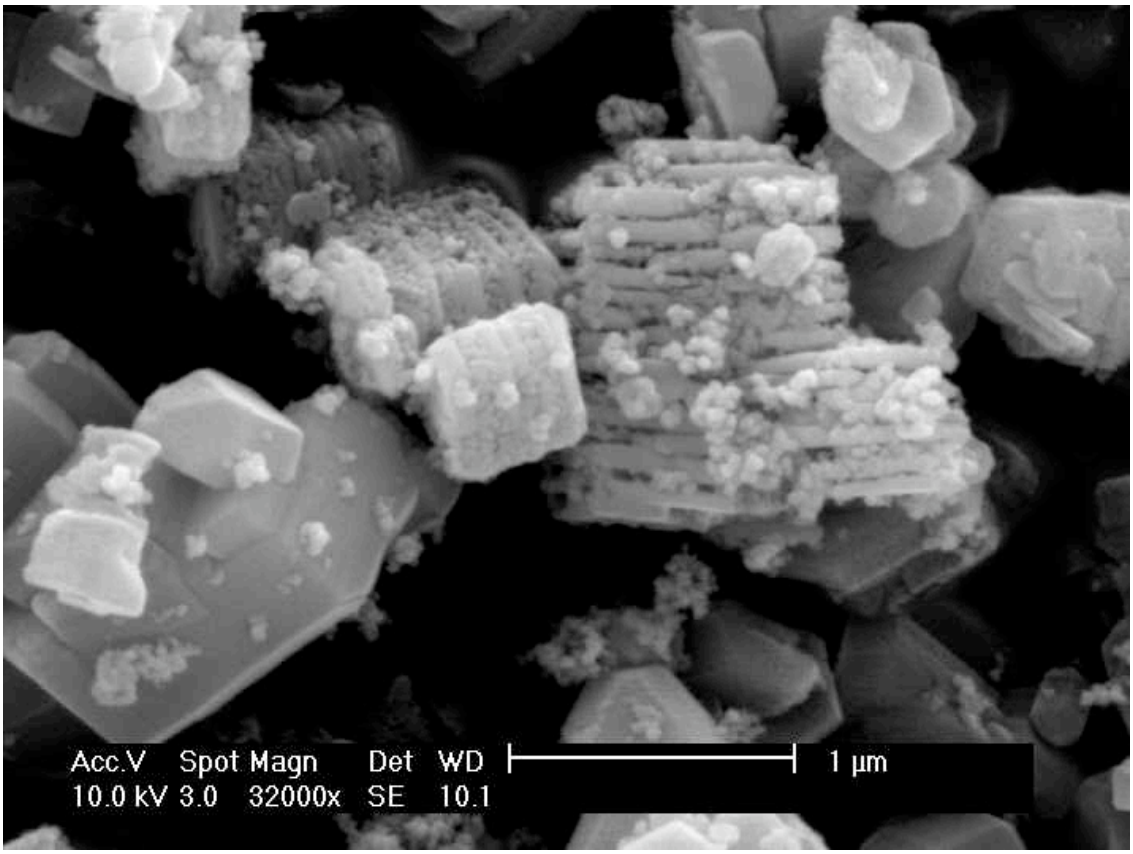

b) Aluminum oxide, 0.3 μm sample

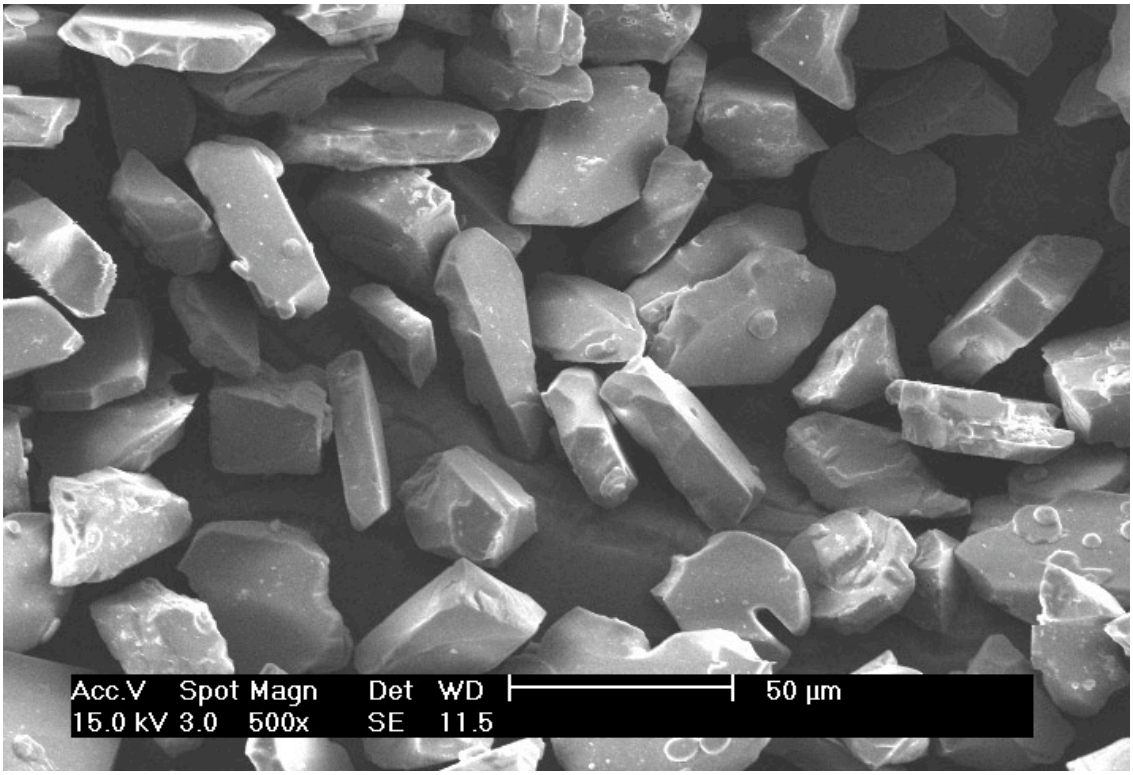

c) Aluminum oxide, 30.009 μm sample

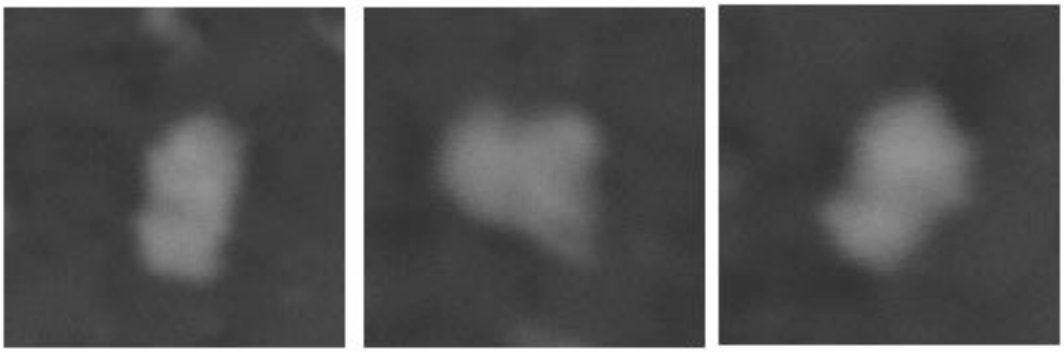

d) Calcium carbonate, 0.06 μm sample (2.043 μm, 1.84 μm, and 1.574 μm average diameter)

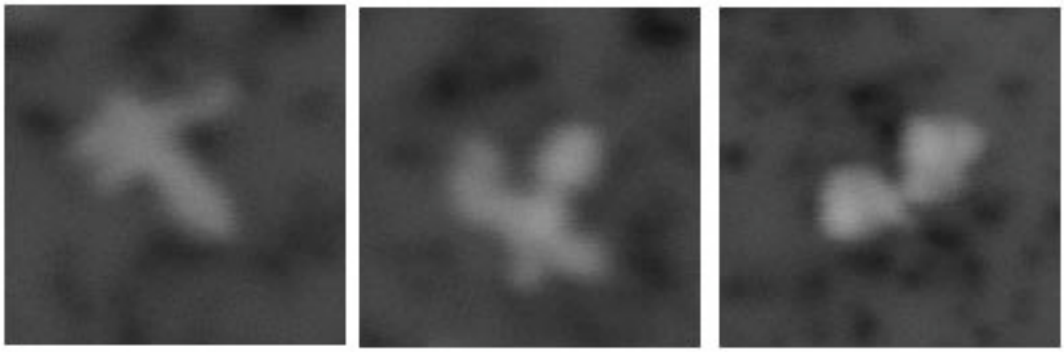

e) Calcium carbonate, 0.8 μm sample (1.26 μm, 1.47 μm, 1.471 μm average diameter)

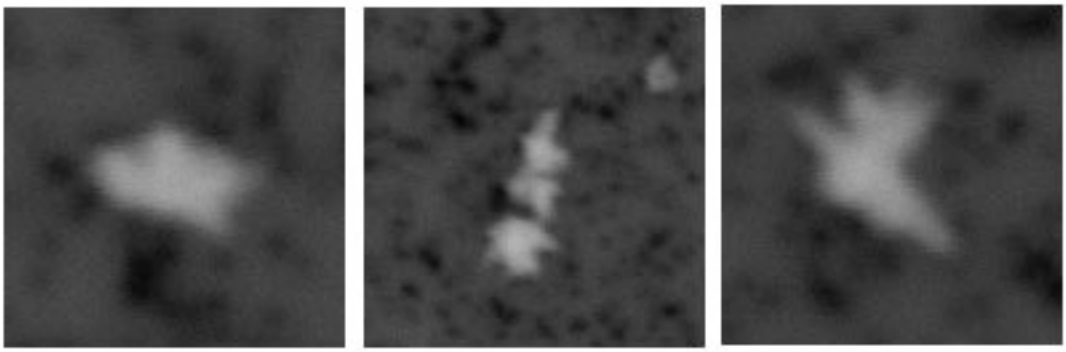

f) Calcium carbonate, 1.1 μm sample (1.308 μm, 1.785 μm, 1.674 μm average diameter)

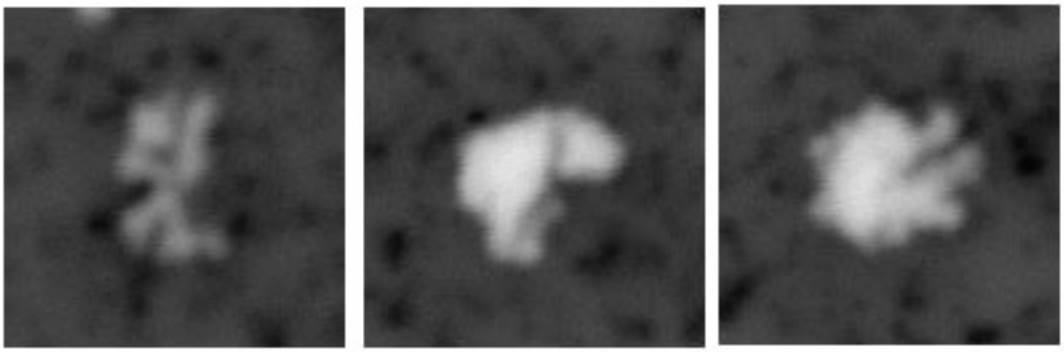

g) Calcium carbonate, 3.0 μm sample (1.665 μm, 2.559 μm, 2.67 μm average diameter)

Appendix B

Expansion of p(g) formulations into Legendre polynomials, and calculation of terms of the multiple scattering term M.

2nd Order Legendre Polynomial (iron oxide fits)

$$p(g) = 1 + b1\cos g + (b2/2)(3\cos^2 g - 1)$$
$$P(\mu) = 1 - (b1/2)\cos e$$
$$P(\mu_0) = 1 - (b1/2)\cos i$$
$$\mathcal{P} = 1 - (b1/4)$$

3rd Order Legendre Polynomial (calcium carbonate fits)

$$p(g) = 1 + b1\cos g + (b2/2)(3\cos^2 g - 1) + (b3/2)(5\cos^3 g - 3\cos g)$$
$$P(\mu) = 1 - (b1/2)\cos e + (b3/2)(5\cos^3 e - 3\cos e)$$
$$P(\mu_0) = 1 - (b1/2)\cos i + (b3/2)(5\cos^3 i - 3\cos i)$$
$$\mathcal{P} = 1 - (b1/4) + (b3/64)$$

Asymmetric Double Henyey-Greenstein Function (aluminum oxide fits)

$$p(g) = \frac{1-c}{2}\left[\frac{1-\xi_1^2}{(1+2\xi_1\cos g+\xi_1^2)^{3/2}}\right] + \frac{1+c}{2}\left[\frac{1-\xi_2^2}{(1-2\xi_2\cos g+\xi_2^2)^{3/2}}\right]$$

$$p(g) = \frac{1+c}{2}\left[1+\sum_{n=1}(2n+1)(-\xi_1)^n P_n(\cos g)\right] + \frac{1-c}{2}\left[1+\sum_{n=1}(2n+1)(\xi_2)^n P_n(\cos g)\right]$$

$$= 1 + \sum_{n=1}\frac{(2n+1)}{2}\left[(1+c)(-\xi_1)^n + (1-c)(\xi_2)^n\right]P_n(\cos g)$$

$$b_n = \frac{(2n+1)}{2}\left[(1-c)(\xi_2)^n - (1+c)(-\xi_1)^n\right]$$

$$P(\mu_0) = 1 + (3/4)\left((1-c)\xi_2 - (1+c)\xi_1\right)(\cos i) - (7/32)\left((1-c)\xi_2^3 - (1+c)\xi_1^3\right)\left(5\cos^3 i - 3\cos i\right)$$
$$+(11/256)\left((1-c)\xi_2^5 - (1+c)\xi_1^5\right)\left(63\cos^5 i - 70\cos^3 i + 15\cos i\right)$$

$$P(\mu) = 1 + (3/4)\left((1-c)\xi_2 - (1+c)\xi_1\right)(\cos e) - (7/32)\left((1-c)\xi_2^3 - (1+c)\xi_1^3\right)\left(5\cos^3 e - 3\cos e\right)$$
$$+(11/256)\left((1-c)\xi_2^5 - (1+c)\xi_1^5\right)\left(63\cos^5 e - 70\cos^3 e + 15\cos e\right)$$
$$\mathcal{P} = 1 + (3/8)\left((1-c)\xi_2 - (1+c)\xi_1\right) + (7/128)\left((1-c)\xi_2^3 - (1+c)\xi_1^3\right) + (11/512)\left((1-c)\xi_2^5 - (1+c)\xi_1^5\right)$$

Bibliography

Akkermans, E., P.E. Wolf, R. Maynard, and G. Maret. 1988. Theoretical study of the coherent backscattering of light by disordered media. *J. Phys. France* **49**, 77-98.

Ambartsumian, V. 1958. The theory of radiative transfer in planetary atmospheres. In *Theoretical Astrophysics*, ed. V. Ambartsumian. New York, Pergamon Press. p. 550-564.

Beers, Y. 1957. *Introduction to the Theory of Error, 2nd Edition*. Reading, MA, Addison-Wesley Publishing Company, Inc. 66 pp.

Bobrov, 1970. Physical properties of Saturn's rings. In *Surfaces and Interiors of Planets and Satellites*, ed. A. Dollfus. London, Academic Press. p. 376-461.

Bohren, C.F. and D.R. Huffman. 1983. *Absorption and Scattering of Light by Small Particles*. New York, John Wiley & Sons, Inc. 530 pp.

Born, M., and E. Wolf. 1980. *Principles of Optics, 6th Edition*. Cambridge, Cambridge University Press. 952 pp.

Buratti, B.J., W.D. Smythe, R.M. Nelson, and V. Gharakhani. 1988. Spectrogoniometer for measuring planetary surface materials at small phase angles. *Appl. Opt.* **27**, 161-165.

Buratti, B.J., A.L. Lane, J. Gibson, H. Burrows, R.M. Nelson, D. Bliss, W. Smythe, V. Garkanian, and B. Wallis. 1991. Triton's surface properties: A preliminary analysis from ground-based, Voyager photopolarimeters subsystem, and laboratory measurements. *J. Geophys. Res.* **96**, 19197-19202.

Chandrasekhar, S. 1960. *Radiative Transfer*. New York, Dover Publications. 393 pp.

Conel, J.E. 1969. Infrared emissivities of silicates: Experimental results and a cloudy atmosphere model of spectral emission from condensed particulate mediums. *J. Geophys. Res.* **74**, 1614-1634.

Cook, A.F., F.A. Franklin, and F.D. Palluconi. 1973. Saturn's rings – a survey. *Icarus* **18**, 317-337.

Cooper, C.D., and J.F. Mustard. 1999. Effects of very fine particle size on reflectance spectra of smectite and palagonitic soil. *Icarus* **142**, 557-570.

Deer, W.A., R.A. Howie, and J. Zussman. 1992. *An Introduction to the Rock-Forming Minerals, 2nd Edition*. Essex, Longman Scientific & Technical. 696 pp.

Egan, W.G. 1969. Polarimetric and photometric simulation of the Martian surface. *Icarus* **10**, 223-227.

Egan, W.G., and T. Hilgeman. 1976. Retroreflectance measurements of photometric standards and coatings. *Appl. Opt.* **15**, 1845-1849.

Egan, W.G., and T. Hilgeman. 1977. Retroreflectance measurements of photometric standards and coatings. Part 2. *Appl. Opt.* **16**, 2861-2864.

Egan, W.G., J. Veverka, M. Noland, and T. Hilgeman. 1973. Photometric and polarimetric properties of the Bruderheim chondritic meteorite. *Icarus* **19**, 358-371.

Etemad, S., R. Thompson, M.J. Andrejco, S. John, and F.C. MacKintosh. 1987. Weak localization of photons: Termination of coherent random walks by absorption and confined geometry. *Phys. Rev. Lett.* **59**, 1420-1423.

Franklin, F.A. and A.F. Cook. 1965. Optical properties of Saturn's rings. II. Two-color phase curves of the two bright rings. *Astron. J.* **70**, 704-720.

Franklin, F.A., and A.F. Cook. 1974. Photometry of Saturn's satellites: The opposition effect of Iapetus at maximum light and the variability of Titan. *Icarus* **23**, 355-362.

Gehrels, T. 1956. Photometric studies of asteroids. V. The light-curve and phase function of 20 Massalia. *Astrophys. J.* **123**, 331-338.

Gehrels, T., T. Coffeen, and D. Owings. 1964. Wavelength dependence of polarization. III. The lunar surface. *Astron. J.* **69**, 826-852.

Gervais, F. 1991. Aluminum oxide (Al_2O_3). In *Handbook of Optical Constants of Solids II,* ed. E.D. Palik. Boston, MA, Academic Press, Inc. 761-775.

Goetz, W. 2002. *The Optical Properties of Martian Dust.* Ph.D. dissertation, University of Copenhagen.

Gradie, J., J. Veverka, and B. Buratti. 1980. The effects of scattering geometry on the spectrophotometric properties of powdered material. *Proc. Lunar Planet. Sci. Conf. 11th*, 799-815.

Hale, A.S., R.M. Nelson, W.D. Smythe, J.L. Piatek, and B.W. Hapke. 2002. Laboratory studies of the opposition effect: Measurements of well-sorted particles smaller and larger than the incidence wavelength. *Lunar Planet. Sci. Conf.* **XXXIII**, abstract #1383.

Hansen, J.E. and T.D. Travis 1974. Light scattering in planetary atmospheres. *Space Sci. Rev.* **16**, 527-610.

Hapke, B.W. 1963. A theoretical photometric function for the lunar surface. *J. Geophys. Res.* **68**, 4571-4586.

Hapke, B. 1981. Bidirectional reflectance spectroscopy. 1. Theory. *J. Geophys. Res.* **86**, 3039-3054.

Hapke, B. 1984. Bidirectional reflectance spectroscopy. 3. Correction for macroscopic roughness. *Icarus* **59**, 41-59.

Hapke, B. 1986. Bidirectional reflectance spectroscopy. 4. The extinction coefficient and the opposition effect. *Icarus* **67**, 264-280.

Hapke, B. 1990. Coherent backscatter and the radar characteristics of outer planet satellites. *Icarus* **88**, 407-417.

Hapke, B. 1993. *Theory of reflectance and emittance spectroscopy*. New York, Cambridge University Press. 454 pp.

Hapke, B. 1999. Scattering and diffraction of light by particles in planetary regoliths. *J. Quant. Spec. Rad. Trans.* **61**, 565-581.

Hapke, B. 2002. Bidirectional reflectance spectroscopy. 5. The coherent backscatter opposition effect and anisotropic scattering. *Icarus* **157**, 523-534.

Hapke, B. and D. Blewett. 1991. Coherent backscatter model for the unusual radar reflectance of icy satellites. *Nature* **352**, 46-47.

Hapke, B. and H. van Horn. 1963. Photometric studies of complex surfaces, with applications to the Moon. *J. Geophys. Res.* **68**, 4545-4570.

Hapke, B., and E. Wells. 1981. Bidirectional reflectance spectroscopy. 2. Experiments and observations. *J. Geophys. Res.* **86**, 3055-3060.

Hapke, B.W., R.M. Nelson, and W.D. Smythe. 1993. The opposition effect of the Moon: The contribution of coherent backscatter. *Science* **260**, 509-511.

Hapke, B., D. DiMucci, R. Nelson, and W. Smythe. 1996. The cause of the hot spot in vegetation canopies and soils: Shadow-hiding versus coherent backscatter. *Remote Sens. Env.* **58**, 63-68.

Hapke, B., R. Nelson, and W. Smythe. 1998. The opposition effect of the Moon: Coherent backscatter *and* shadow hiding. *Icarus* **133**, 89-97.

Helfenstein, P., J. Veverka, and P.C. Thomas. 1988. Uranus satellites: Hapke parameters from Voyager disk-integrated photometry. *Icarus* **74**, 231-239.

Helfenstein P., N. Currier, B.E. Clark, J. Veverka, M. Bell, R. Sullivan, J. Klemaszewski, R. Greeley, R.T. Pappalardo, J.W. Head III, T. Jones, K. Klaasen, K. Magee, P. Geissler, R. Greenberg, A. McEwen, C. Philips, T. Colvin, M. Davies, T. Denk, G. Neukum, and M.J.S. Belton. 1998. Galileo observations of Europa's opposition effect. *Icarus* **135**, 41-63.

Henyey, L.G. and J.L. Greenstein. 1941. Diffuse radiation in the galaxy. *Astrophs. J.* **93**, 70-83.

Irvine, W.M. 1966. The shadowing effect in diffuse media. *J. Geophys. Res.* **71**, 2931-2937.

Irvine, W.M. and A.P. Lane. 1973. Photometric properties of Saturn's rings. *Icarus* **18**, 171-176.

Ishimaru, A. and Y. Kuga. 1982. Attenuation constant of a coherent field in a dense distribution of particles. *J. Opt. Soc. Am.* **72**, 1317-1320.

Ishimaru, A. and L. Tsang. 1988. Backscattering enhancement of random discrete scatterers of moderate sizes. *J. Opt. Soc. Am. A* **5**, 228-236.

Kawata, Y. and W.M. Irvine. 1974. Models of Saturn's rings which satisfy the optical observations. *Proc. IAU Symp.* **65**, 441-464.

Klaasen, K.P., T.C. Duxbury, and J. Veverka. 1979. Photometry of Phobos and Deimos from Viking Orbiter images. *J. Geophys. Res.* **84**, 8478-8486.

Kuga, Y. and A. Ishimaru. 1984. Retroreflectance from a dense distribution of spherical particles. *J. Opt. Soc. Am. A* **1**, 831-835.

Kuga, Y., L. Tsang, and A. Ishimaru. 1985. Depolarization effects of the enhanced retroreflectance from a dense distribution of spherical particles. *J. Opt. Soc. Am. A* **2**, 616-618.

Lane, A.L., C.W. Hord, R.A. West, L.W. Esposito, K.E. Simmons, R.M. Nelson, B.D. Wallis, B.J. Buratti,, L.J. Horn, A.L. Graps, and W.R. Pryor. 1986. Photometry from Voyager 2: Initial results from the Uranian atmosphere, satellites, and rings. *Science* **233**, 65-70.

Lane, A.L., R.A. West, C.W. Hord, R.M. Nelson, K.E. Simmons, W.R. Pryor, L. W. Esposito, L.J. Horn, B.D. Wallis, B.J. Buratti, T.G. Brophy, P. Yanamandra-Fisher, J.E. Colwell, D.A. Bliss, M.J. Mayo, and W.D. Smythe. 1989. Photometry from Voyager 2: Initial results from the Neptunian atmosphere, satellites, and rings. *Science* **246**, 1450-1454.

Lumme, K., and E. Bowell. 1981. Radiative transfer in the surfaces of atmosphereless bodies. I. Theory. *Astron. J.* **86**, 1694-1704.

Lumme, K., and W.M. Irvine. 1976. Photometry of Saturn's rings. *Astron. J.* **81**, 865-893.

Mallama, A., D. Wang, and R.A. Howard. 2002. Photometry of Mercury from SOHO/LASCO and Earth. *Icarus* **155**, 253-264.

Minnaert, M. 1961. Photometry of the moon. In *Planets and Satellites*, Kuiper, G.P. and B.M. Middlehurst (eds.) 213-245.

Mie, G. 1908. Beiträge zur Optik trüber Medien speziell kolloidaler Metallösungen. *Ann. Phys.* **25**, 377-445.

Mishchenko, M.I. 1991. Light scattering by randomly oriented axially symmetric particles. *J. Opt. Soc. Am. A* **8**, 871-882.

Mishchenko, M.I. 1992a. Polarization characteristics of the coherent backscatter opposition effect. *Earth, Moon, & Planets* **58**, 127-144.

Mishchenko, M.I. 1992b. The angular width of the coherent back-scatter opposition effect: An application to icy outer planet satellites. *Astrophys. Space Sci.* **194**, 327-333.

Mishchenko, M.I. 1993a. On the nature of the polarization opposition effect exhibited by Saturn's rings. *Astrophys. J.* **411**, 351-361.

Mishchenko, M.I. 1993b. Light scattering by size–shape distributions of randomly oriented axially symmetric particles of a size comparable to a wavelength. *Appl. Opt.* **32**, 4652-4666.

Mishchenko, M.I. 1994. Asymmetry parameters of the phase function for densely packed scattering grains. *J. Quant. Spec. Rad. Trans.* **52**, 95-110.

Mishchenko, M.I., and J.M. Dlugach. 1993. Coherent backscatter and the opposition effect for E-type asteroids. *Planet. Space Sci.* **41**, 173-181.

Mishchenko, M.I., and L.D. Travis. 1998. Capabilities and limitations of a current Fortran implementation of the T-matrix method for randomly oriented, rotationally symmetric scatterers. *J. Quant. Spec. Rad. Trans.* **60**, 309-324.

Mishchenko, M. I., J. M. Dlugach, E. G. Yanovitskij, and N. T. Zakharova. 1999a. Bidirectional reflectance of flat, optically thick particulate layers: an efficient radiative transfer solution and applications to snow and soil surfaces, *J. Quant. Spec. Rad. Trans.* **63**, 409-432.

Mishchenko, M. I., I. V. Geogdzhayev, B. Cairns, W. B. Rossow, and A. A. Lacis. 1999b. Aerosol retrievals over the ocean by use of channels 1 and 2 AVHRR data: sensitivity analysis and preliminary results, *Appl. Opt.* **38**, 7325-7341

Moersch, J.E. and P.R. Christensen. 1995. Thermal emission from particulate surfaces: A comparison of scattering models with measured spectra. *J. Geophys. Res.* **100**, 7465-7477.

Muinonen, K., K. Lumme, and J. Peltoniemi. 1990. Scattering of light by crystals: A possible application to planetary dust. *Adv. Space Res.* **10**, 189-192.

Mustard, J.F. and J.E. Hays. 1997. Effects of hyperfine particles on reflectance spectra from 0.3 to 25 μm. *Icarus* **125**, 145-163.

Nelson, R.M. 2002. The opposition effect: A very unusual case. *Solar System Remote Sensing Symposium*. LPI Contrib. #1129. pp. 53.

Nelson, R.M, B.J. Buratti, B.D. Wallis, A.L. Lane, R.A. West, K.E. Simmons, C.W. Hord, and L.W. Esposito. 1987. Voyager 2 photopolarimeter observations of the Uranian satellites. *J. Geophys. Res.* **92**, 14905-14910.

Nelson, R.M., B.W. Hapke, W.D. Smythe, and L.J. Horn. 1998. Phase curves of selected particulate materials: The contribution of coherent backscattering to the opposition surge. *Icarus* **131**, 223-230.

Nelson, R.M., B.W. Hapke, W.D. Smythe, and L.J. Spilker. 2000. The opposition effect in simulated planetary regoliths. Reflectance and circular polarization ratio change at small phase angle. *Icarus* **147**, 545-558.

Nelson, R.M., B.W. Hapke, W.D. Smythe, A.S. Hale, and J.L. Piatek. 2002a. The opposition effect: Laboratory studies compared to theoretical models. *Lunar Planet.Sci. Conf.* **XXXIII**, abstract #1816.

Nelson, R.M., W.D. Smythe, B.W. Hapke, and A.S. Hale. 2002b. Low phase angle laboratory studies of the opposition effect: search for wavelength dependence. *Planet. Space. Sci.* **50**, 849-856.

O'Leary, B.T. 1967. The opposition effect of Mars. *Astrophys. J.* **149**, L147-L149.

O'Leary, B., and F. Briggs. 1970. Optical properties of Apollo 11 moon samples. *J. Geophys. Res.* **75**, 6532-6538.

O'Leary, B., and F. Briggs. 1973. Optical properties of Apollo 12 moon samples. *J. Geophys. Res.* **78**, 792-797.

O'Leary, B.T. and D.G. Rea. 1968. The opposition effect of Mars and its implications. *Icarus* **9**, 405-428.

Oetking, P. 1966. Photometric studies of diffusely reflecting surfaces with applications to the brightness of the moon. *J. Geophys. Res.* **71**, 2505-2513.

Peters, K.J. 1992. Coherent-backscatter effect: A vector formulation accounting for polarization and absorption effects and small or large scatterers. *Phys. Rev. B* **46**, 801-812.

Price, M.J. 1974. Optical scattering properties of Saturn's rings. II. *Icarus* **23**, 388-398.

Querry, M.R., G. Osborne, K. Lies, R. Jordon, and R.M. Coveney Jr. 1978. Complex refractive index of limestone in the visible and infrared. *Appl. Opt.* **17**, 353-356.

Salisbury, J.W., B. Hapke and J.W. Eastes. 1987. Usefulness of weak bands I midinfrared remote sensing of particulate planetary surfaces. *J. Geophys. Res.* **92**, 702-710.

Seeliger, H. 1887. Zur Theorie der Beleuchtung der grossen Planeten insbesondere des Saturn. *Abhandl. Bayer. Akad. Wiss. II, Cl. XVI.* 114 pp.

Seeliger, H. 1893. Theorie der Beleuchtung staubförmiger kosmisher Massen insbesondere des Saturnringes. *Abhandl. Bayer. Akad. Wiss. II, Cl. XVIII.* 72 pp.

Shevchenko, V.G., I.N. Belskaya, Yu. N. Krugly, V.G. Chiomy, and N.M. Gaftonyuk. 2002. Asteroid observations at low phase angles. II. 5 Astraea, 75 Eurydike, 77 Frigga, 105 Artemis, 119 Althaea, 124 Alkeste, and 201 Penelope. *Icarus* **155**, 365-374.

Shkuratov, Y. 1988. Diffractional model of the brightness surge of complex structure surfaces. *Kin., Phys., Cel. Bodies* **4**, 33-39.

Simonelli, D. P. and J. Veverka. 1986. Phase curves of materials on Io: Interpretation in terms of Hapke's function. *Icarus* **68**, 503-521.

Spitzer W. and D. Kleinman. 1961. Infrared lattice bands in quartz. *Phys. Rev.* **121**, 1324-1335.

Stephen, M.J., and G. Cwilich. 1986. Rayleigh scattering and weak localization: Effects of polarization. *Phys. Rev. B* **34**,, 7564-7572.

Taylor, R.C., T. Gehrels, and A.B. Silvester. 1971. Minor planets and related objects. VI. Asteroid (110) Lydia. *Astron. J.* **76**, 141-146.

Thomas, P.C., J. Veverka, P. Helfenstein, R. Hamilton Brown, and T.V. Johnson. 1987. Titania's opposition effect: Analysis of Voyager observations. *J. Geophys. Res.* **92**, 14911-14917.

Thorpe, T.E. 1979. The Mars opposition effect at 20° N latitude and 20° W longitude. *Icarus* **37**, 389-398.

Tsang, L. and A. Ishimaru. 1984. Backscattering enhancement of random discrete scatterers. *J. Opt. Soc. Am. A* **1**, 836-839.

van Albada, M.P. and A. Lagendijk. 1985. Observation of weak localization of light in a random medium. *Phys. Rev. Lett.* **55**, 2692-2695.

van Albada, M.P. and A. Lagendijk. 1987. Vector character of light in weak localization: Spatial anisotropy in coherent backscattering from a random medium. *Phys. Rev. B* **36**, 2353-2356.

van Albada, M.P., M.B. van der Mark, and A. Lagendijk. 1987. Observation of weak localization of light in a finite slab: Anisotropy effects and light-path classification. *Phys. Rev. Lett.* **58**, 361-364.

van de Hulst, H.C. 1957. *Light Scattering by Small Particles.* New York, Dover Publications. 470 pp.

van der Mark, M.B., M.P. van Albada, and A. Lagendijk. 1988. Light scattering in strongly scattering media: Multiple scattering and weak localization. *Phys. Rev. B* **37**, 3575-3592.

Wolf, P.E., and G. Maret. 1985. Weak localization and coherent backscattering of photons in disordered media. *Phys. Rev. Lett.* **55**, 2696-2699.

Wolf, P.E., G. Maret, E. Akkermans, and R. Maynard. Optical coherent backscattering by random media: an experimental study. *J. Phys. France* **49**, 63-75.